


In Situ Geochronology for the Next Decade

Final Report

Submitted in response to
NNH18ZDA001N-PMCS:
Planetary Mission Concept Studies

August 10, 2020



Barbara Cohen

Barbara Cohen
Principal Investigator
NASA Goddard Space Flight Center

Michael Amato

Michael Amato
Planetary and Lunar Business Lead
NASA Goddard Space Flight Center



TABLE OF CONTENTS

1. SCIENTIFIC OBJECTIVES	1
1.1 Science Questions and Objectives	1
1.2 Science Traceability	2
2. PAYLOAD DEFINITION AND SAMPLE ANALYSIS	3
2.1 Instrument Descriptions	4
2.2 Sample Analysis Concept of Operations	6
3. HIGH-LEVEL MISSION CONCEPT	8
3.1 Overview	8
3.2 Technology Maturity and Technology Development Plan	9
3.3 Risks	10
4. LUNAR GEOCHRONOLOGY LANDER MISSION	10
5. VESTA GEOCHRONOLOGY HOPPER MISSION	16
6. MARS GEOCHRONOLOGY LANDER MISSION	20
7. DEVELOPMENT SCHEDULES AND COSTS	22
APPENDICES	
A – ACRONYMS	A-1
B1 – SCIENCE TEAM STUDY REPORT	B1-1
B2 – PAYLOAD	B2-1
B3 – DESIGN TEAM STUDY REPORT	B3-1
B4 – DETAILED COST AND SCHEDULE	B4-1
C – SPECIAL TECHNICAL ANALYSIS – MOBILITY TRADES	C-1
D – REFERENCES	D-1



STUDY AUTHORS

SCIENCE DEFINITION TEAM

Barbara Cohen (PI), GSFC
Kelsey Young (DPI), GSFC
Nicolle Zellner, Albion College
Kris Zacny, Honeybee Robotics
R. Aileen Yingst, PSI
Ryan Watkins, PSI
Sarah Valencia, GSFC
Tim Swindle, U of Arizona
Stuart Robbins, SwRI
Noah Petro, GSFC
Dan Moriarty, GSFC
Stephen Indyk, Honeybee Robotics

Juliane Gross, Rutgers University
Jennifer Grier, PSI
John Grant, Smithsonian
Caleb Fassett, MSFC
Ken Farley, Caltech
Ben Farcy, U of Maryland
Bethany Ehlmann, Caltech
Darby Dyar, PSI
Natalie Curran, GSFC
Carolyn van der Bogert, University Westfalische
Ricardo Arevalo, U of Maryland
Scott Anderson, SwRI

GSFC ENGINEERING TEAM

Mike Adams
Ginger Bronke
Eric Cardif
John Crow
Amani Ginyard
Kyle Hughes
Stephen Indyk
Cameron Jerry
Andrew Jones
Richard Lynch
Stephen Meyer
Ryo Nakamura
Anthony Nicoletti
Dave Palace
Miguel Benayas Penas
Glenn Rakow
Bruno Sarli
Marcia Segura
Thomas Spitzer
David Steinfeld
John Zuby

GSFC MISSION DESIGN LAB TEAM

Maryam Bakhtiari-Nejad
Grant Barrett
Bob Beaman
Emily Beckman
Kaitlyn Blair
Jennifer Bracken
Thomas Carstens
Angel Davis
Paul Earle
Luis Gallo
Camille Holly
Frank Kirchman
Steve Levitski
Blake Lorenz
Mike Machado
Dick McBirney
Khashy Parsay
Sara Riall
Russ Snyder
David Steinfeld
James Sturm
Huaizu You
John Young

LOCKHEED MARTIN (MARS LANDER CONCEPT)

Richard Warwick
Noble Hatten
Mark Johnson
Scott Francis
Madeline O'Neil
Tim Linn



EXECUTIVE SUMMARY

Geochronology, or determination of absolute ages for geologic events, underpins many inquiries into the formation and evolution of planets and our Solar System. The bombardment chronology inferred from lunar samples has played a significant role in the development of models of early Solar System and extrasolar planet dynamics, as well as the timing of volatile, organic, and siderophile element delivery. Absolute ages of ancient and recent magmatic products provide strong constraints on the dynamics of magma oceans and crustal formation, and the longevity and evolution of interior heat engines and distinct mantle/crustal source regions. Absolute dating also relates habitability markers to the timescale of evolution of life on Earth.

The importance of constraining the planetary history via absolute dating has been reaffirmed in multiple community documents, including the last two Planetary Science Decadal Surveys. For example, *Vision and Voyages* advocates efforts to “Determine the chronology of basin-forming impacts and constrain the period of late heavy bombardment in the inner solar system and thus address fundamental questions of inner solar system impact processes and chronology.” For both the Moon and Mars, sample-return missions are being planned where samples can be returned to terrestrial laboratories and examined in depth. But the number of geochronologically-significant terrains across the inner Solar System far exceeds our ability to conduct sample return to all of them. Accordingly, the *Vision and Voyages* document also recommended technology development of *in situ* geochronology experiments that have now advanced; several such instruments will be TRL 6 by the time of the next Decadal Survey.

We formulated a set of medium-class (New Frontiers) mission concepts to three different locations (the Moon, Mars, and Vesta) where sites that record Solar System bombardment, magmatism, and habitability are uniquely preserved and accessible. We developed a notional payload consisting of two instruments capable of measuring radiometric ages, an imaging spectrometer and optical cameras to provide site geologic context and sample characterization, a trace-element analyzer to augment sample contextualization, and a sample acquisition and handling system. A Vesta hopper and single-site lunar and Mars landers to advance Solar System chronology would likely fit into the New Frontiers cost cap in our study. Such missions would also enable a broad suite of geologic investigations such as basic geologic characterization, geomorphologic analysis, establishing ground truth for remote sensing analyses, analyses of major, minor, trace, and volatile elements, atmospheric and other long-lived monitoring, organic molecule analyses, and soil and geotechnical properties.

These investments have made possible New Frontiers-class missions that would carry multiple, complementary instruments to conduct *in situ* dating with the precision needed to meet community-identified science goals. Allowing proposals for missions that improve Solar System chronology by *in situ* dating could take advantage of both recent advances in science and creative implementation solutions emerging from the planetary science community. The study team believes smart proposal teams and organizations would likely be able to fit competing versions of these missions into a New Frontiers-class mission. We urge the Decadal Survey panel to include missions in the New Frontiers list that address compelling problems in geochronology by either sample return or *in situ* dating.



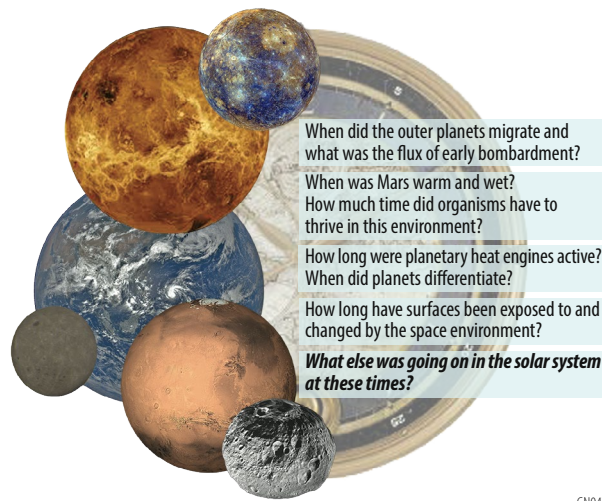
MAIN REPORT

1. SCIENTIFIC OBJECTIVES

1.1 Science Questions and Objectives

Geochronology, or the determination of absolute ages for geologic events, underpins many inquiries into the formation and evolution of planetary bodies and our Solar System (Figure 1). Geochronology can drive major advances in planetary science in the next decade, including calibrating body-specific chronologies and creating a framework for understanding Solar System formation, illuminating the effects of impact bombardment on life, and revealing the evolution of planetary surface environments and interiors. Longstanding geochronology-driven science goals are to:

- Determine the chronology of basin-forming impacts to constrain the time period of heavy bombardment in the inner Solar System and thus address fundamental questions related to inner Solar System impact processes and chronology.
- Reduce the uncertainty for inner Solar System chronology in the “middle ages” (1-3 Ga) to improve models for planetary evolution, including volcanism, volatiles, and habitability.
- Establish the history of habitability across the Solar System. Absolute ages of potentially habitable terrains would help resolve when localized environments within the inner Solar System could have supported biological activity.
- Calibrate body-specific chronologies. Geologic epochs on different planetary bodies have been defined by events that have little apparent relationship to each other. Calibrating body-specific chronologies is critically important for comparing planetary histories, contextualizing Solar System dynamics, and developing an interplanetary perspective on the evolution of planetary surfaces, interiors, and habitable environments.



GN047

Figure 1: Geochronology would create a framework uniting processes across the inner Solar System.

In the last two decades, NASA has invested in developing innovative *in situ* dating techniques that will be TRL 6 by the time of the next Decadal Survey. These instruments are less precise than their terrestrial laboratory counterparts, but sufficient to answer a wide range of questions related to Geochronology Science Goals (Appendix B2). The team developed Objectives through which *in situ* dating would resolve Science Objectives specific to the Moon, Mars, and Vesta, tracing to Lunar Exploration Analysis Group (LEAG), Mars Exploration Program Analysis Group (MEPAG), and Small Bodies Analysis Group (SBAG) goals documents. See Appendix B1 for fuller descriptions of the Science Goals and Objectives.



Moon 1: Establish the chronology of basin-forming impacts by measuring the radiometric age of samples directly sourced from the impact melt sheet of a pre-Imbrian lunar basin. *In situ* dating of an impact-melt sheet of a lunar basin thought to be significantly older than the Imbrium basin would place it either within the canonical cataclysm (3.9 Ga) or as part of a declining bombardment in which most impacts are 4.2 Ga or older.

Moon 2: Establish the age of a very young lunar basalt to correlate crater size-frequency distributions with crystallization ages. *In situ* dating would reduce the uncertainty in absolute model ages derived from crater size-frequency distribution measurements to no more than 20% of the current uncertainty shown between different lunar chronology functions.

Mars 1: Establish the age of a well-exposed Hesperian martian lava terrain to correlate crater size-frequency distributions with crystallization ages. *In situ* dating could radically improve our understanding of Mars's volcanic history, with relevance to geodynamics and interior cooling, assign widely-separated igneous provinces absolute ages, and examine the compositional progression of igneous sources with time. This would also provide a direct test of the quality of the adaptation of the lunar cratering chronology to Mars.

Mars 2: Establish the epoch of martian habitability by measuring the radiometric age of Noachian clay-bearing stratigraphies. *In situ* dating to constrain the timing of Noachian unit formation would provide an important anchor for crater spatial densities of terrains hosting geologic evidence from Mars' most habitable period. This has concomitant implications for reconciling the timing of the development of life on Earth (~3.5 Ga oldest fossils) and hypothesized spikes in early impact bombardment (~3.9 Ga).

Vesta: Establish the radiometric ages of vestan samples with well-established provenance. *In situ* dating would constrain Vesta's geologic timescale by dating key stratigraphic craters and contiguous geologic terrains. Given the large disparity in ages derived by different logical assumptions, this level of precision would not only reveal the ages of key basins but would set firm constraints on the impactor flux estimates used throughout the Main Asteroid Belt.

1.2 Science Traceability

The Science Traceability Matrix (STM) (**Table 1**) establishes measurement and mission requirements needed to address the Geochronology science objectives and traceability to the lander payload. The overarching requirement in all cases is to measure the age of the desired lithology. To accomplish this, several measurements and associated observations need to be made, including a) using radiometric chronology to directly measure the age of samples derived from the target lithology with precision better than or equal to +200 Myr (95% confidence, or 2σ); b) contextualizing the desired lithology using petrology, mineralogy, and/or elemental chemistry; and c) relating the measured lithology age to crater counting of the lithology's terrain.

For this study, measurement requirements for all Geochronology mission goals and objectives would be met by carrying a single notional payload comprising representative instruments. All instruments, except the Inductively Coupled Plasma Mass Spectrometer (ICPMS), are planned to be TRL 6 in 2023 (the start of the next Planetary Decadal), so no additional development costs nor technology maturation would be required before mission Phase B (see **Sections 2, 3**, and **Appendix B2** for payload element technical details and TRL assessment).

Of the mission measurement requirements, determining the radiometric age is the most demanding. *In situ* geochronology has only been performed as an opportunistic measurement on the Curiosity mission (*e.g.*, Farley *et al.*, 2014; Martin *et al.*, 2019; Cohen *et al.*, 2020). Application of multiple chronometers would provide technologic redundancy as well as increasing confidence in the interpretation of the geologic events experienced by the sample, though disagreement would not negate the inherent value of each measurement. The team therefore baselined two independently-developed *in situ* dating instruments, CDEX and KArLE. These instruments are on track to meet or exceed the precision requirements in the NASA Technology Roadmap, which specify $\pm 5\%$ for rocks 4.5 billion years old (Ga) (approximately ± 200 Myr, 2σ), and a desired precision of $\pm 1\%$ for 4.5 Ga rocks (or about



Table 1: Science Traceability Matrix.

Science Objectives	Measurement Goals	Measurement Requirements	Payload Element*	Functional Requirements
Moon 1 and 2: Measure the radiometric ages of a pre-Imbrian lunar basin and a very young lunar basalt. OR	Measure the age of the desired lithology with precision ± 200 Myr	Use Rb-Sr radiometric chronology to directly measure the age of samples derived from the target lithology	CDEX	Collect, triage, and analyze ten 0.5-2 cm samples of each target lithology Remotely sense the lander workspace to provide sample context at the landing site to create spatially contiguous maps Conduct sample analysis at two different sites
		Use K-Ar radiometric chronology to directly measure the age of samples derived from the target lithology	KArLE	
Mars 1 and 2: Establish the ages of a well-exposed Hesperian martian lava and Noachian clay-bearing stratigraphies. OR	Contextualize the desired lithology using petrology, mineralogy, and/or elemental chemistry	Measure major- and trace-element geochemistry of the samples to establish parentage and evolution of lithologies	ICPMS, CDEX, KArLE	
		Identify mineralogy by mapping abundances of olivine, pyroxene, oxides, plagioclase, and aqueous alteration minerals, including phyllosilicates, sulfates, carbonates, and other hydrated salts	UCIS	
Vesta: Establish the radiometric ages of vestan samples with well-established provenance.	Relate the measured lithology age to crater counting of the lithology's terrain	Image samples at the microscale to determine grain size, petrology	Microimager	
		Determine the composition of the surface unit to place the lithologies into a regional and global context	Panoramic Imager, UCIS	
*Chemistry and Dating Experiment (CDEX), Potassium-Argon Laser Experiment (KArLE), Inductively Coupled Plasma Mass Spectrometry (ICPMS), Ultra-Compact Imaging Spectrometer (UCIS)				

± 50 Myr, 2σ). The uncertainty in a geochronology measurement is influenced not only by technological capabilities of the instrument but also by the complexity (*e.g.*, mineralogy, alteration history, etc.) of the planetary material and geologic setting being investigated. Thus, sample selection, location, and geological context are just as important as the analytical methodologies that enable radiometric dating. The team included remote imaging, spectroscopy, and trace-element compositional measurements in the baseline payload so the landing site and selected samples are well-understood prior to dating.

Functionally, a mission to accomplish these science objectives must be a landed mission with access to surface samples. The mission must be capable of collecting, triaging, and analyzing ten 0.5-2 cm samples of each target lithology (derivation of number of samples is described in **Appendix B1**). The mission must also be capable of remotely sensing the lander workspace and the landing site to provide sample context and create spatially contiguous maps of the landing site for orbital context. Because the notional payload would include complex and potentially expensive instruments, the team chose to maximize mission investment by asking the team to design a mission that could conduct *in situ* analyses at two different sites, thereby accomplishing multiple science goals. To drive the engineering constraints for these studies, the team considered pairs of candidate landing sites for each body. Although these are notional landing sites based on the identified science questions, the team made every effort to ensure these sites were representative of the range of sites the science community might desire for a mission with geochronology capabilities. **Appendix B** provides additional information about candidate landing sites. Mobility proved to be the most difficult functional requirement to meet, as described in **Appendix C**, and this requirement was not met in all mission architectures.

2. PAYLOAD DEFINITION AND SAMPLE ANALYSIS

The notional payload would provide a complementary and robust approach to resolving the science goals using technologies that would be ready for a New Frontiers 6 Announcement of Opportunity. A common payload would be implemented for all destinations, with minor changes to adapt to the



Martian environment. The selected hardware is meant to be representative of a payload that could meet the science requirements and be accommodated on a New Frontiers-class mission, rather than endorsing an instrument or specific payload configuration. The payload mass, power, and data needs are summarized in **Table 2**. Mass and power contingency (30%) were added to account for the early nature of this payload concept. More information about the payload elements, their heritage, and performance is provided in **Appendix B2**.

Table 2: Summary of payload mass, power, and communication needs.

	Mass		Average Power		Data Generation CBE (Mbit) ²	
	CBE (kg)	MEV (kg) ¹	CBE (W)	MEV (W) ¹	Lunar & Mars	Vesta
CDEX						
CDEX instrument	55	71.5	140	182	22400	
Grinding station	5.7	7.41	20	26	N/A	
Postgrind Imager	0.6	0.78	7	9.1	1500	
Sample Manipulation Arm	10	13	20	26	1600	
<i>Vacuum chamber & pump (Mars only)</i>	<i>5.13</i>	<i>6.67</i>	<i>12</i>	<i>15.6</i>	N/A	
KArLE						
KArLE Instrument ³	22.9	29.77	100	130	21220	
<i>Vacuum pump (Mars only)</i>	<i>0.13</i>	<i>0.169</i>	<i>12</i>	<i>15.6</i>	N/A	
ICPMS ³	9.5	12.4	102	132.6	38	
UCIS (Including DPU)	5	6.5	30	39	11268	22046
Panoramic Imagers (total for 2)	1.16	1.508	14.8	19.2	1454	2529
Microimager	1.1	1.43	7.5	9.75	180	240
Imaging DEA ⁴	1.1	1.43	0	0	N/A	
Sample acquisition and triage						
PlanetVac	16	20.8	32	41.6	30	40
Triage station	2.5	3.25	6	7.8	N/A	
Electronics box	2.3	2.99	22.8	29.6		
Totals	132.8/ 138.1	172.7/ 179.5			59690	71613
¹ MEV=CBE+30% margin						
² Total for full described mission. Data values for imagers, CDEX, and UCIS are post-compression						
³ KArLE and ICPMS would share laser ablation and mass spectrometer subsystems; see Appendix B2						
⁴ Would serve Postgrind Imager, Panoramic Imagers, and Microimager						

2.1 Instrument Descriptions

The Chemistry and Dating EXperiment (CDEX) (**Figure 2**) (Anderson *et al.*, 2015a; Anderson *et al.*, 2015b) uses LA-MS to obtain elemental abundance and LARIMS to obtain isobar-free rubidium-strontium (Rb-Sr) dates. Samples presented to the CDEX inlet are laser-ablated at hundreds of locations on a flat surface in a two-dimensional grid. The ablated ions can be sent directly to a time-of-flight mass spectrometer to measure chemistry or can be selectively ionized to obtain Rb-Sr ages.

The Potassium-Argon Laser Experiment (KArLE) is a LIBS-MS investigation (*e.g.*, Cohen *et al.*, 2014; Cohen and Cho, 2018) to measure K-Ar ages (**Figure 3**). KArLE uses laser ablation to interrogate about a dozen spots on a solid sample. An integrated carousel accepts rocks and positions them for imaging and laser ablation. After ablation, KArLE uses Laser-Induced Breakdown Spectroscopy (LIBS) to determine K, admits the gas

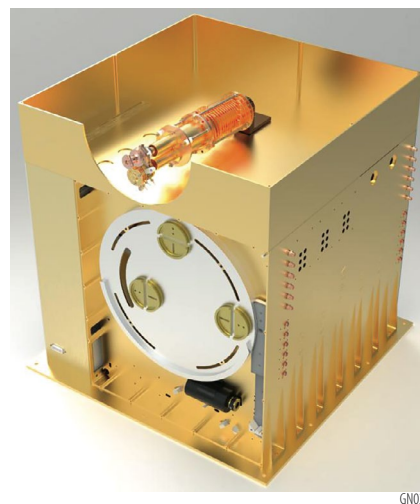


Figure 2: Rendering of the CDEX instrument (Southwest Research Institute).



released by ablation to a quadrupole mass spectrometry (QMS) to measure Ar, and relates the two measurements using a laser scanning microscope.

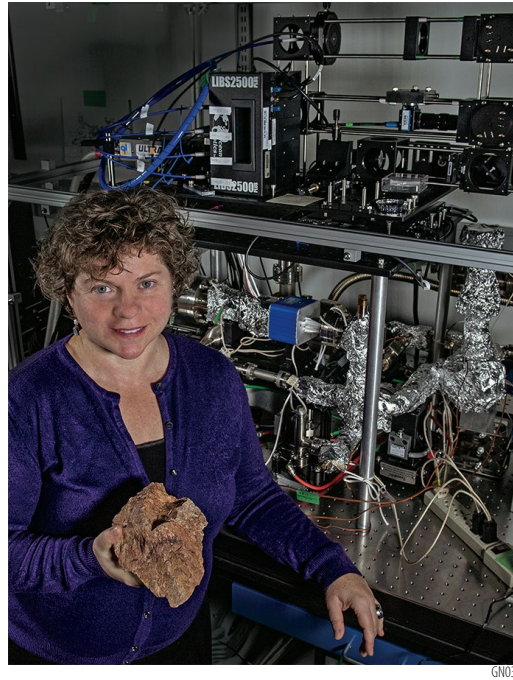


Figure 3: KARLE instrument is already in the laboratory breadboard stage, as pictured at GSFC.

Both geochronology instruments detect a range of major and minor elements that would assist in associating samples with specific lithologies, but complementary trace element analysis (ppmw levels and below) using ICPMS would enable discrimination of genetic relationships between different planetary materials. The ICPMS (Arevalo Jr. *et al.*, 2019) uses laser ablation to release particles, ionizes them using a plasma source for ionization, and measures them using a mass spectrometer. The ICPMS would use an identical laser ablation system and a similar enough mass spectrometer to KARLE that, for this study, the team decided to efficiently package the two instruments to eliminate duplication of these components.

Remote sensing would be used to characterize the diversity of lithologies present at the landing site, differentiate samples for further measurement, and facilitate reconstruction of the local and regional geology of the site. A suite of cameras would be required to acquire color images at hand-lens and mm- to cm-scale within the environs of the lander, as well as panoramic views of the landing site. The team chose suite of imagers from Malin Space Science Systems' commercial product line (Maki *et al.*, 2012; Maki *et al.*, 2003; Maki *et al.*, 2018), though suitable imagers have flown on a variety of planetary missions in diverse environments. The Panoramic Cameras have an 80-degree wide field of view (FOV) and draw heritage from TAGCAMS on OSIRIS-REx (**Figure 4**). The Microimager and Postgrind Imager are based on the Mars Hand Lens Imager (MAHLI) instrument (**Figure 4**).

Infrared (IR) spectroscopy detects electronic and vibrational absorptions related to mineralogy in reflected light. Shortwave visible infrared imaging spectroscopy (SWIR; 0.6-3.6 μm) is appropriate for this mission concept study because Mars dust obscures the rock in visible and near-infrared (VNIR) wavelengths, and VNIR signatures on the Moon are modified by space weathering. The team chose JPL's Ultra Compact Imaging Spectrometer (UCIS), an Offner spectrometer using e-beam gratings and HgCdTe detectors drawing direct heritage from the Moon Mineralogy Mapper M3 instrument (**Figure 5**). UCIS collects reflectance spectra from 600 - 3600 nm, enabled by cryogenically cooling via a small Peltier cooler.

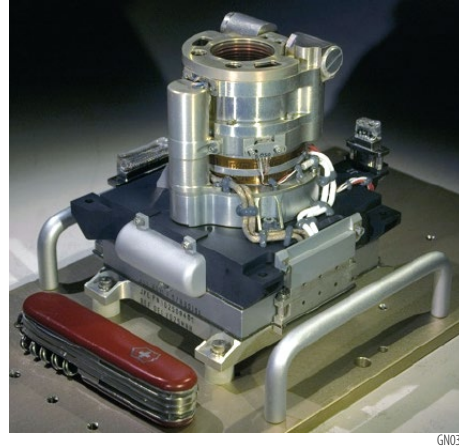


Figure 4: Examples of MSSS cameras (left, OSIRIS-REx TAGCAMS and right, MSL MAHLI).

At present, geochronology measurements are not standoff or remote techniques; all share a common need for sample acquisition, manipulation, and analysis. The team chose Honeybee Robotics' PlanetVac (Zacny *et al.*, 2014a) (**Figure 6**), a pneumatic system, to loft and sort regolith into fines and rocks of appropriate size for analysis (0.5-2 cm diameter), though several other systems (*e.g.*, drills, scoop/sieves, etc.) could be considered with appropriate modifications to the concept of operations. In this study, we included two PlanetVac cones on separate lander footpads to enable sampling redundancy in the event the material under one cone is unsuitable for sampling, as well as flexibility to sample at two different positions under the lander. Valving controls the release of the compressed gas at the nozzles and the compressed gas tanks are sized for multiple sampling events plus ample margin.

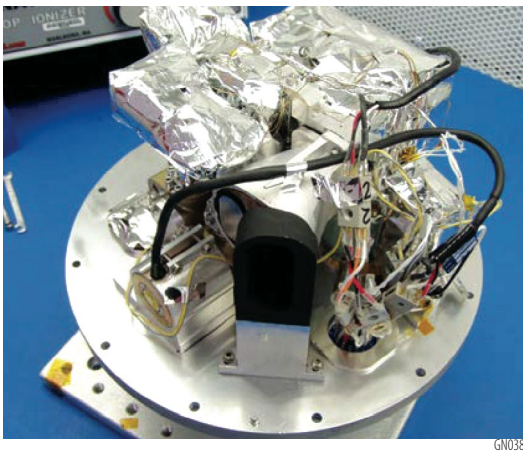


Figure 5: JPL's UCIS instrument has direct heritage from the M3 lunar instrument.



Figure 6: The Honeybee Robotics PlanetVac foot unit.

2.2 Sample Analysis Concept of Operations

The number of samples that would need to be collected and analyzed is a function of a) how many aliquots of the lithology of interest are needed to ensure statistical confidence in assigning an age; b) how much of the lithology of interest makes up the regolith at the landing site; and c) how many rocks of correct size (0.5 – 2 cm in diameter) exist in the regolith. For this study, we adopted a requirement to analyze ten samples of each lithology of interest to achieve robust counting statistics. The team selected candidate landing sites where current understanding of remote sensing and geologic setting make it probable that the majority of the samples retrieved would represent the lithology of interest, but adopted a further factor of three to account for potential mixing, requiring 30 samples to be collected and triaged per lithology of interest. Finally, the team derived the abundance of appropriately-sized



rocks using data from landing sites on the Moon and Mars and from the Kapoeta meteorite. This factor drives the number of samples that need to be collected and examined in triage. The estimated excavation volume on all bodies would be a few liters or less, a volume easily accommodated by PlanetVac. **Appendix B1** provides additional detail about sampling statistics and landing sites.

The team developed a reference sample analysis process through which the samples would be acquired, analyzed, prioritized, and sequentially introduced to each instrument (**Figure 7**). The reference sequence would be repeated for each sample until the required number of samples were completed at each site. The sequence may be paused at multiple points for additional data analysis, troubleshooting, or to manage payload power. Additional process information is provided in **Appendix B2** and sequence adaptation for each destination is described in **Sections 4** (Lunar), **5** (Vesta), and **6** (Mars). The instruments would be arranged in an arc around the Sample Manipulation Arm (SMA) (**Figure 8**). PlanetVac would pneumatically gather surface samples, transfer, and sieve them to the 0.5-2 cm diameter required for analysis. The sieved samples would be gravity-fed into the triage station for identification and prioritization using data from the spectrometer and Microimager. After ground-in-the-loop analysis of the initial triage data, prioritized samples would be selected for further analysis. The SMA would move samples from the triage station to the other instruments, including grinding the sample to a 10-micron polish for CDEX, imaging the ground surface, presenting the sample to the CDEX aperture, and finally dropping it into the KArLE carousel. Each sample cycle, excluding triage analysis, generates approximately 3 Gbits of data (MEV).

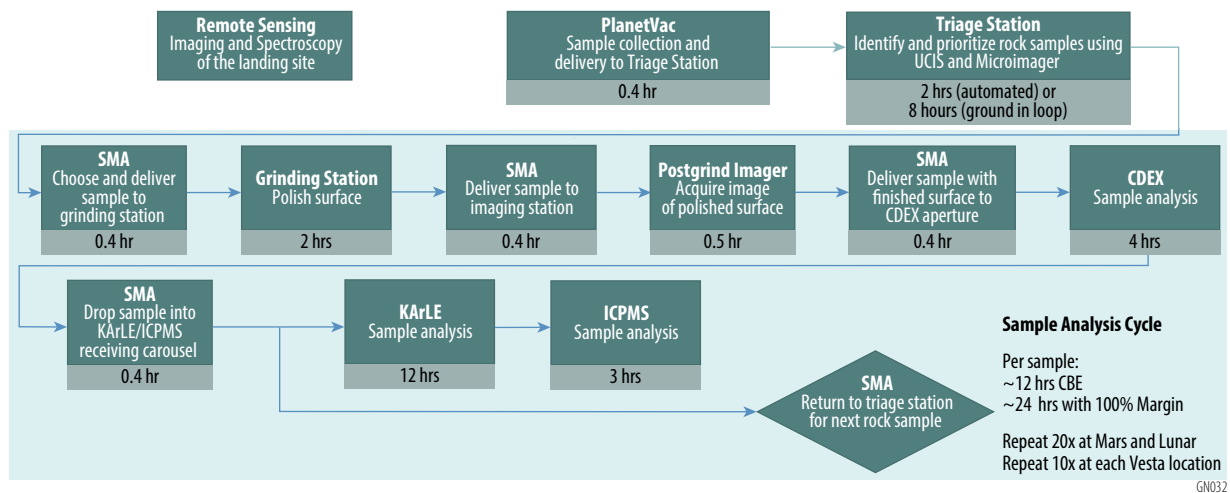


Figure 7: Nominal sample analysis sequence common to all mission concepts. All times given are CBE plus 100% margin.

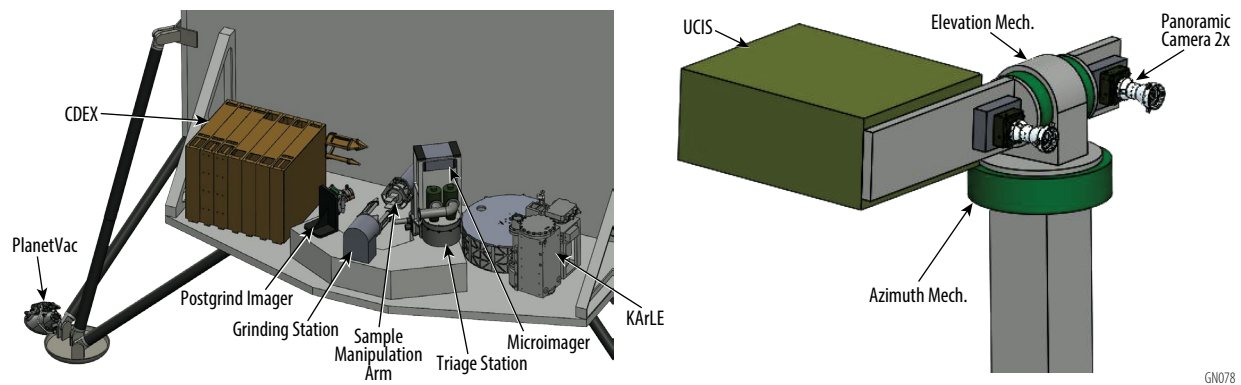


Figure 8: Notional geochronology payload layout for the lunar and Vesta missions.



In parallel with sample science, the Panoramic Imagers and UCIS obtain 360-degree coverage of the landing area from lander to horizon. They would be mast mounted on a rotation/tilt mechanism. Because of lighting constraints, the collection cadence of the context images would be specific to each destination, described in **Sections 4** (Lunar), **5** (Vesta), and **6** (Mars). A total of 20 samples would be analyzed in all concepts, so the data generated by the Geochronology instruments would be essentially the same for all destinations. On Vesta, where there would be two science sites, two context imaging datasets and would be acquired and there would be additional triage processes planned. Data summaries for the Lunar, Vesta, and Mars concepts are shown in **Table 2**.

3. HIGH-LEVEL MISSION CONCEPT

3.1 Overview

All Geochronology mission studies were conducted at Concept Maturity Level (CML) 4. They present an implementation concept at the subsystem level, as well as science traceability, key technologies, heritage, risks and mitigations. In addition, the team developed cost models. Some CML 5 aspects were also accomplished, including requirements traceability and notional schedules to the subsystem level. The studies assumed that each mission would be a Class B, PI-led mission, consistent with a New Frontiers Announcements of Opportunity.

Geochronology mission requirements are summarized in **Table 3** and detailed mission design is discussed in **Appendix B3**. All versions of the Geochronology mission in this study would use a single lander, with the capability to hop to a second site implemented for the Vesta design. The need for *in situ* analysis necessitated a lander design and the goal to stay within the anticipated New Frontiers 6 cost cap precluded investigating multiple scientifically-interesting destinations on the Moon and Mars (see **Appendix C** for technical analysis of mobility). A lunar hopper proved unfeasible due to the large propellant mass that would be required, so the study went forward with a lander that would not meet the requirement to sample from two sites. The Mars lander likewise would not meet the requirement for two sites, because adding mobility would have driven the mission outside the New Frontiers cost cap.

Table 3: Geochronology mission requirements.

Mission Functional Requirement	Mission Design Requirements	Lander Requirements	Ground System Requirements	Operations Requirements
Collect, triage, and analyze ten 0.5-2 cm samples of each target lithology	Lunar transfer of trajectory ≤ 5 days Vesta transfer trajectory ≤ 5 years Mars transfer trajectory ≤ 3 years	≥ 1 m/s separation velocity from Launch Vehicle Provide ΔV of 1,864 m/s for landing Land with a velocity of ≤ 0.5 m/s vertical and ≤ 0.1 m/s horizontal at 5 m above the surface Land Safely with clearance between surface and lower deck of at least 0.5m	34m DSN Antenna Receive Lander engineering & science data telemetry Encrypt commands Decrypt downlink Provide commanding	Implement required DDOR Manage time correlations Maneuvers Support DSN passes
Remotely sense the lander workspace to provide sample context at the landing site to create spatially contiguous maps	Falcon 9 Heavy recovery (Moon) or expendable (Vesta and Mars) with 5m fairing	Data Storage 100 Gbits Return data with less than 20 day latency Deliver 180 kg of science instruments to surface	Record/archive science data Provide critical event telecom coverage: Launch Sep, S/A	Monitor Lander state of health Implement contingency procedures
Conduct sample analysis at two different sites	Mission surface lifetime sufficient to conduct all operations Reliability Category 2, Class B	LVDS data interface with instruments Provide 200 W electrical power to the science instruments (Lunar, Vesta). Provide 700 W-hr/Sol electrical power to the science instruments (Mars). 0.1 ms timing accuracy with 10^{-6} S stability relative to ground station	Deployment, Instrument Deployments DDOR Science Data Center, Science Operations Center, Mission Operations Center	Implement science sequences Manage lander operations Perform ops sim testing



Figure 9 illustrates an example organizational structure for implementing a Geochronology New Frontiers mission. As with all New Frontiers missions, the PI would have ultimate responsibility and authority to execute the mission. It would be highly recommended that the lead Project Management organization also be responsible for elements within the organization that are of the same color boxes as the PM box color. It would also be highly recommended that the lead organization for the lander also own responsibility for mission operations. Instrument providers and science team members would be Co-I's from various organizations.

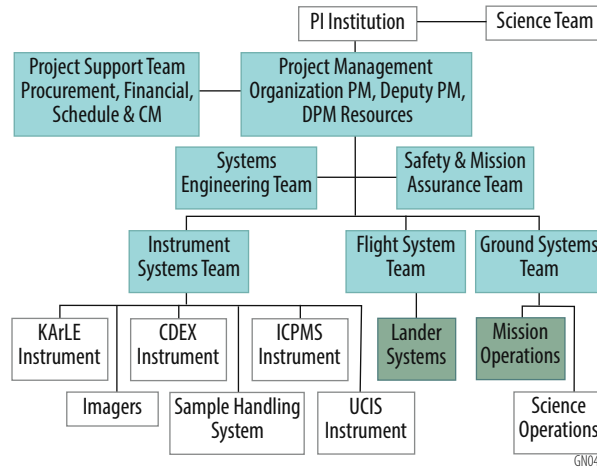


Figure 9: Notional Geochronology mission organization showing key roles and responsibilities.

Planetary Protection: The lunar lander is assumed to be category I-L as per NID 8715.128 “Planetary Protection Categorization for Robotic and Crewed Missions to the Earth's Moon” so the requirements are minimal, consisting primarily of proper documentation. The Vesta concept is expected to be Category III as per NPR 8020.12D “Planetary Protection for Extraterrestrial Missions” due to the Mars flyby so an analysis demonstrating the probability of impacting Mars is less than 1×10^{-2} for a period of 50 years must be generated. Category III missions impose clean room and possibly microbial reduction efforts. The Mars concept is Category IV and as such will be subject to the more strict clean room and contamination control requirements prescribed in the NID and NASA-HDBK-6022 NASA Standard Procedures for the Microbial Examination for Space Hardware. Cost estimates for the Mars Lander and Systems I&T are based on a Lockheed Martin proprietary parametric cost model, which incorporates costs related to PP activities. Assessing full instrument compatibility with Planetary Protection requirements is future work however with 50% added reserves provide confidence that Geochronology payload costs estimates encompass some level of PP related activities. Request for formal Planetary Protection categorization should be made during Pre-Phase A mission formulation.

3.2 Technology Maturity and Technology Development Plan

CDEX, KArLE, and UCIS, currently under development in NASA instrument maturation programs, are expected to achieve TRL 6 (system/sub-system model or prototype demonstration in an operational environment, **Table 4**) by 2023, the start date of the next decadal survey. They will therefore be ready for infusion into a mission with no additional technology investment in Pre-Phase A or Phase A. However, these instruments would require mission-level investment to build a flight version that meets the requirements of the specific mission, including any unique environment and payload integration needs. ICPMS is currently being developed in the PIDDP program to achieve TRL 4 (low fidelity system/component breadboard to demonstrate basic functionality and performance predictions) by 2023. Further maturation to TRL 6 would be necessary (for example, via MatISSE or DALI) prior to a flight mission AO release; if this follow on investment were not made, then any potential mission would need to make an investment to mature the instrument or descope it with a moderate loss to



science. All imagers in this study are TRL 9 and available for any mission in the next decade. Sample manipulation components will be at TRL 6 or higher maturity, developed for flight for all considered destinations. Instrument maturity details are provided in **Appendix B2**.

Table 4: Payload technology readiness levels and heritage.

Payload Element	Provider	Flight heritage	Status	TRL in 2023			Maturation path (NASA investments) ¹	Additional needs (Mission investments)
				Moon	Mars	Vesta		
CDEX	SwRI	--	Performance demonstrated in functional breadboard	6	6	6	PIDDP (2013), MatISSE (2017), Proposed to Mars 2020 and Discovery 2015	Destination-specific environment and integration
KaRLE	GSFC	GSFC mass spectrometers including SAM, LADEE, MOMA-MS, LIBS from ChemCam, carousel from SAM	Performance demonstrated in functional breadboard	6	6	6	PIDDP (2014), DALI (2018), proposed to Mars 2020	Destination-specific environment and integration
ICPMS	University of Maryland	GSFC mass spectrometers including SAM, LADEE, MOMA-MS	Proof of concept demonstrated	4	4	4	PICASSO (2018), SBIR/STTR; additional MatISSE or DALI to achieve TRL 6	Destination-specific environment and integration
UCIS	JPL	Moon Mineralogy Mapper, others	Performance demonstrated in functional breadboard	6	6	6	MatISSE (2012) for Mars and Vesta, DALI (2018) for Moon	Destination-specific environment and integration
Panoramic and Microimager	MSSS	MAHLI, WATSON, ECAMS (MSL and OSIRIS-REx)	Flown in relevant environments	9	9	9	CLPS (2022)	None
PlanetVac and other hardware	Honeybee Robotics	--	Performance demonstrated in functional breadboard	9	6	9	MMX, CLPS	Destination-specific environment and integration

¹Planetary Instrument Concepts for the Advancement of Solar System Observations (PICASSO); Maturation of Instruments for Solar System Exploration (MatISSE); Development and Advancement of Lunar Instrumentation (DALI); Small Business Innovation Research (SBIR) / Small Business Technology Transfer (STTR); Commercial Lunar Payload Services (CLPS); Martian Moons Explorer (MMX)

All lander hardware has flight heritage and current TRL of 6 or greater. Algorithm and flight software development is needed that would integrate TRN and HA as a complete system. TRN will be demonstrated on Mars 2020 prior to Geochronology PDR. Development of these components is being actively pursued by NASA within a variety of lander programs including Safe and Precise Landing – Integrated Capabilities Evolution (SPICE) program which will be largely completed before a Geochronology mission would be proposed. Lunar and Vesta lander hardware details are provided in **Appendix B3**.

3.3 Risks

Geochronology top risks and their mitigation activities are shown and ranked in **Figure 10** and **Table 5**. Risk Management definitions in GSFC GPR 7120.4D were used to rank the likelihood and consequence of the risks. Risks 1 and 3 are unique to the Vesta mission, while the other 4 risks would be germane to any Geochronology mission studied.

4. LUNAR GEOCHRONOLOGY LANDER MISSION

Lander Design

The lunar Geochronology flight system consists of a lander that meets the mission requirements in **Table 3**. **Appendix B3** provides additional details about the lander systems.

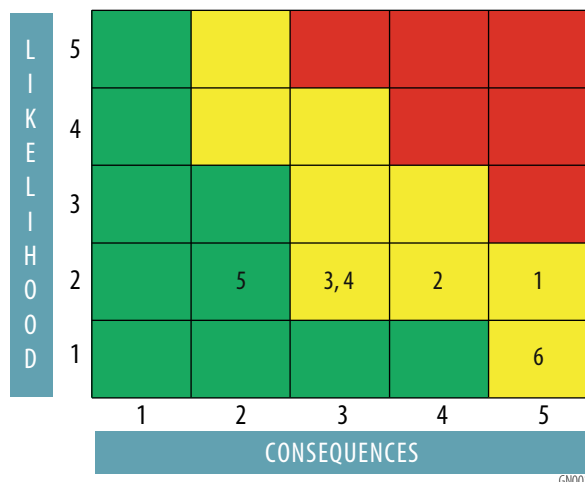


Figure 10: Geochronology Risk Matrix.

Table 5: Geochronology mission top risks, impacts, and potential mitigation strategies.

Risk ID Type	Risk	L	C	Potential Mitigation
1 Technical	Given that the best-resolution images of Vesta from the Dawn mission’s low-altitude mapping orbit (LAMO) are 70 meters per pixel, too coarse to identify hazards at the lander scale, there is a possibility that the mission’s mapping survey would fail to find a suitable landing location, resulting in the need to rework landing algorithms at cost and schedule (analogous to OSIRIS-REx)	2	5	<ol style="list-style-type: none"> 1) Lessons learned from OSIRIS-REx, Mars 2020, InSight and other landed missions would be incorporated into the guidance and navigation concept. 2) Additional research and development of landing guidance and navigation algorithms should be conducted, prior to AO release or mission would have to carry those costs. 3) A planned mission should extend sufficient resources into Phase E to allow for survey algorithm updates and testing as new information about Vesta’s surface would become available.
2 Technical	Given the use of terrain-relative navigation in landing, there is a possibility that additional research and development would be required during the implementation phase resulting in impacts to cost and schedule.	2	4	<ol style="list-style-type: none"> 1) Lessons learned from OSIRIS-REx, Mars 2020, InSight and other landed missions would be incorporated into the guidance and navigation concept. 2) Additional research and development of landing and hopping guidance and navigation should be conducted prior to AO release or mission would have to carry those costs.
3 Technical	Given that taking off from the surface of a planetary body and landing again is a complex operation, there is a possibility that additional research and development would be identified during the implementation phase, resulting in impacts to cost and schedule.	2	3	<ol style="list-style-type: none"> 1) Lessons learned from OSIRIS-REx, Mars 2020, InSight and other landed missions would be incorporated into the guidance and navigation concept. 2) Additional research and development of landing and hopping guidance and navigation should be conducted prior to AO release or mission would have to carry those costs.
4 Programmatic	Given that the surface operations includes many sequential elements, there is a possibility that additional research and development would be longer than planned, resulting in an increase mission lifetime.	2	3	<ol style="list-style-type: none"> 1) A proposed mission should rigorously define the surface operations timeline and ensure it would include sufficient margin. 2) Lessons learned from complex, real-time missions such as Curiosity and Perseverance should be implemented to provide appropriate training for the science and operations teams to handle payload operations and science interpretation (nominal and off-nominal).
5 Programmatic and Cost	Given that this study assumes NASA will have invested resources into maturing mission-enabling payload and lander technologies to TRL 6 prior of the New Frontiers 6 AO, there is a possibility that investments would not have been made, resulting in cost to mature instrument within the proposed New Frontiers mission budgets.	2	2	NASA SMD should make necessary investments in instrument maturation described in the study report prior to AO release or mission would have to carry those costs.
6 Technical	Given that the mission would require a sample acquisition and distribution system, there is a possibility that a failure would occur in the chain, resulting in a loss of some or all geochronology science.	1	5	<ol style="list-style-type: none"> 1) A proposed mission would implement redundancy in the sample acquisition and distribution system, including PlanetVac hardware and mechanism control electronics. 2) A proposed mission would implement a robust qualification and testing program at the systems and component level.



The lander (4.6 meters tall, 3.9 meters long, 3.3 m wide) would easily fit within the Falcon 9 5 meter fairing, as shown in **Figure 11**. A lunar Geochronology mission would have a launch window of three days every two weeks. The lander would use 4 main engines with a thrust of 4 kN each and 12 ACS thrusters (two sets of six pairs, one set for primary and one for redundancy). The lander would use three solar arrays (totaling 12 m² total area) to provide a daylight peak power of 928 W BOL, 785 W EOL at lunar noon. An 1,176 AH battery (packaged as four separate batteries) would support night loads. Communications and science operations would be restricted to lunar daylight, although the receiver would be left on during the lunar night. The thermal design would use louvers to keep the lander cool during the lunar daylight and warm during the lunar night. The instruments would be accommodated on the lander as shown in **Figure 8**. To reduce the distance the samples must travel, CDEX, KARLE, and the sample handling system would be located in an on one side of the lander, as close as possible to the lunar surface (**Figure 11**).

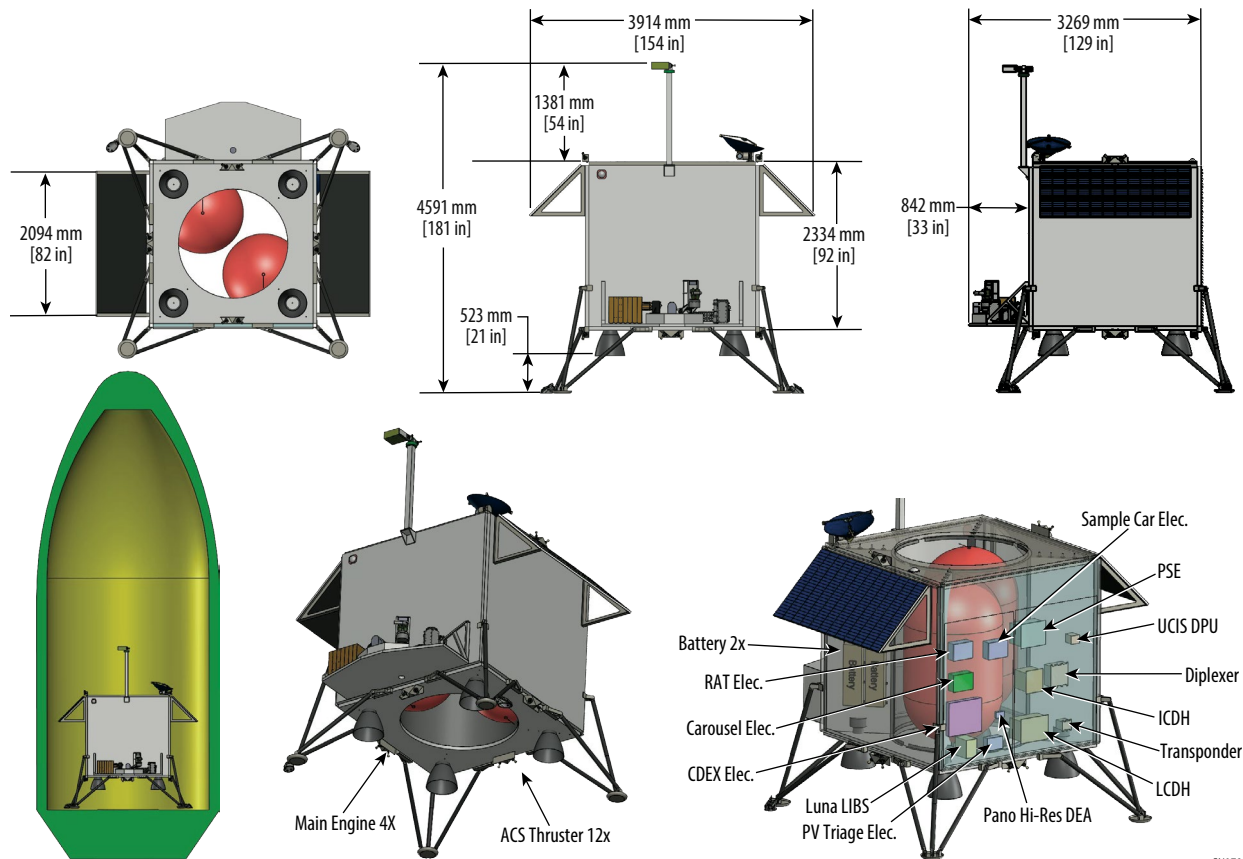


Figure 11: The lunar geochronology lander would use heritage hardware and structural designs that are well within the state of the art to deliver outstanding science from the surface of the Moon. More views of the lunar lander are also shown.

Table 6 summarizes the mass and power characteristics of the Geochronology lunar lander. **Table 7** summarizes the flight system characteristics.

Flight and Surface Operations

Table 8 summarizes the lunar mission design for launching on a Falcon 9 Heavy Recovery. The lunar mission would have a 3-day launch window every 2 weeks. The Falcon 9 Heavy would place the lander into a lunar transfer trajectory. The lander would perform Lunar Orbit Insertion (LOI) into a 250 km-altitude circular polar lunar orbit to overfly the selected site at local midmorning (nominally 9 am local time). The lander would deorbit and brake to lower the lander to 100 m above the landing site



Table 6: The lunar lander bus mass and power demonstrate adequate margin in meeting mission requirements.

	Mass			Average Power (Day)			Average Power (Night)		
	CBE (kg)	% Cont.	MEV (kg)	CBE (W)	% Cont.	MEV (W)	CBE (W)	% Cont.	MEV (W)
Structures & Mechanisms	691	26	817	0	0	0	0	0	0
Thermal Control	34	10	37	0	0	0	0	0	0
Propulsion (dry mass)	342	10	376	0	0	0	0	0	0
Attitude Control (Cruise and Descent only)	2	10	30	104	10	114	0	0	0
Command & Data Handling	23	10	25	52	10	57	16	30	20
Telecommunications	27	10	29	57	10	63	17	10	19
Power	394	10	433	5	10	5	1	10	1
Total Lander Bus	1,538	14	1,749	218	10	240	34	21	40

Table 7: Lunar lander characteristics.

Flight System Element Parameters	Value/ Summary
General	
Design life, months	12
Structure	
Structures material	Aluminum, Composite, Titanium
Number of articulated structures	2
Number of deployed structures	2
Aeroshell diameter, m	N/A
Thermal Control	
Type of thermal control used	Louvers/Radiators, Heat Pipes
Propulsion	
Estimated Delta-V budget, m/s	2,681 m/s
Propulsion type(s) and associated propellant(s)/oxidizer(s)	Regulated Bipropellant, MMH, NTO
Number of thrusters and tanks	4 Main Engines 12 ACS Engines 1 MMH Tanks 2 NTO Tanks 2 Pressurant Tanks
Specific impulse of each propulsion mode, seconds	293
Attitude Control	
Control method	3-axis
Control reference	Inertial
Attitude control capability, arcseconds	50
Attitude knowledge limit, arcseconds	6
Agility requirements	Landing, Terrain Relative Navigation
Articulation/#-axes	High Gain Antenna - 2 axis
Sensor and actuator information	0.35 deg sun sensors, 50 arcsec star scanners, 0.005 deg/hr MIMU, LiDAR, Laser Altimeter, Camera
Command & Data Handling	
Flight element housekeeping data rate, kbps	2,000
Data storage capacity, Mbits	50,000
Maximum storage record rate, kbps	1,000
Maximum storage playback rate, kbps	100,000
Power	
Type of array structure	Body-mounted
Array size, meters ²	12
Solar cell type	TJGaAs
Expected power generation at Beginning of Life (BOL) and End of Life (EOL), Watts	928W BOL, 785W EOL
On-orbit average power consumption, Watts	N/A
Lunar day Power Consumption, Watts	266.0
Lunar night Power Consumption, Watts	41.6
Battery type (NiCd, NiH, Li-ion)	Li-ion
Battery storage capacity, amp-hours	1,176



with a velocity magnitude of 8.2 m/s, then vertically descend to land with a terminal velocity of ≤ 0.5 m/s vertical and ≤ 0.1 m/s horizontal at 5 m above the surface. The lander would use Terrain Relative Navigation (TRN) and possibly hazard avoidance approaches to select landing sites and avoid pre-defined hazardous areas. The entire landing operation, from start of DOI to touchdown, would take a little over one hour (Figure 12).

Table 8: Lunar mission design summary.

Parameter	Value
Orbit parameters	250 km circular polar
Mission lifetime	12 months
Maximum eclipse period	14.5 days
Launch site	Cape Canaveral, FL
Total lander mass with contingency (includes instruments)	1,921.3 kg
Propellant mass without contingency	2,983.5 kg
Propellant contingency	10%
Propellant mass with contingency	3,315.0 kg
Launch adapter mass with contingency	97.4 kg
Total launch mass	5,334 kg
Launch vehicle	Falcon 9 Heavy Recovery
Launch vehicle lift capability	7,049 kg
Launch vehicle mass margin	1,715.3 kg
Launch vehicle mass margin (%)	32.2%

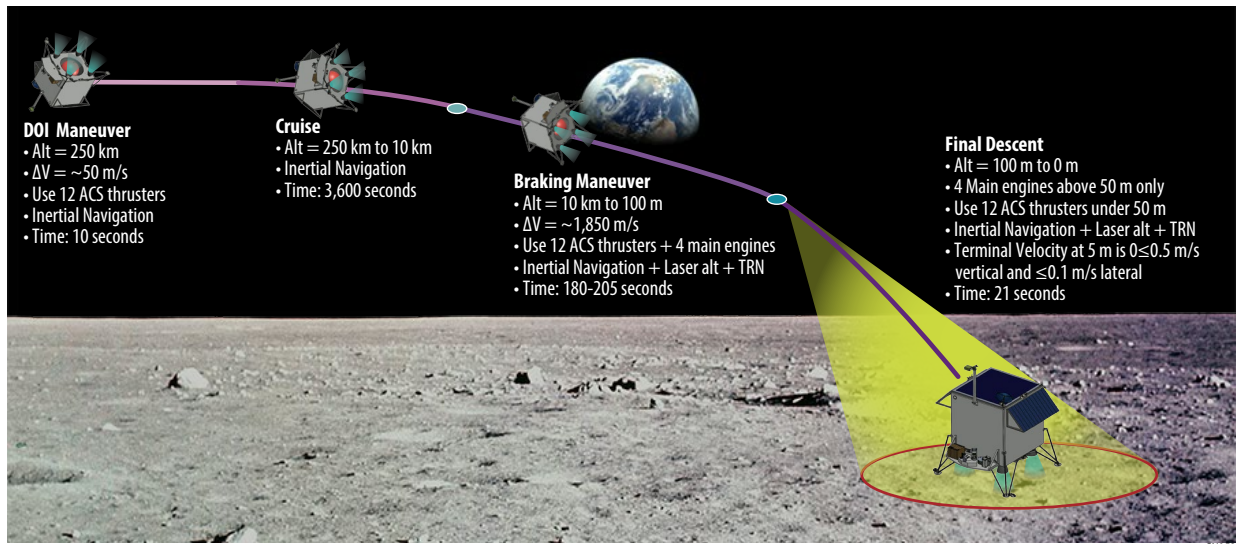


Figure 12: Lunar descent and landing summary.

After landing, a five-day lander checkout would be performed, followed by instrument commissioning and initial data collection. The estimated daylight remaining at the landing site after landing is 261 hours (10.8 days), which would provide margin should any anomalies occur after landing and prior to lunar night. Normal surface operations would occur during the daylight portion of the lunar day (14.5 Earth days), when the lander would perform sample analysis and site imaging while recharging the lander batteries and communicating with Earth. Then it would enter a low-power state for the lunar night.

The available power would permit each sample analysis cycle to directly follow the reference flow described in Section 2. Communication bandwidth would allow for the full sample science data to be downlinked in the DSN pass immediately following data acquisition. Surface operations would permit



two samples to be analyzed per lunar day, with time allotted for wakeup/checkout and shutdown. A full set of context imaging would be collected on terrestrial day 4 (mid-day lighting), with flexibility to enable imaging under other lighting conditions. Nominal science/surface operations would continue for approximately 300 Earth days, and a full year is budgeted to include margin. The lunar surface data and power profile is shown in **Figure 13**.

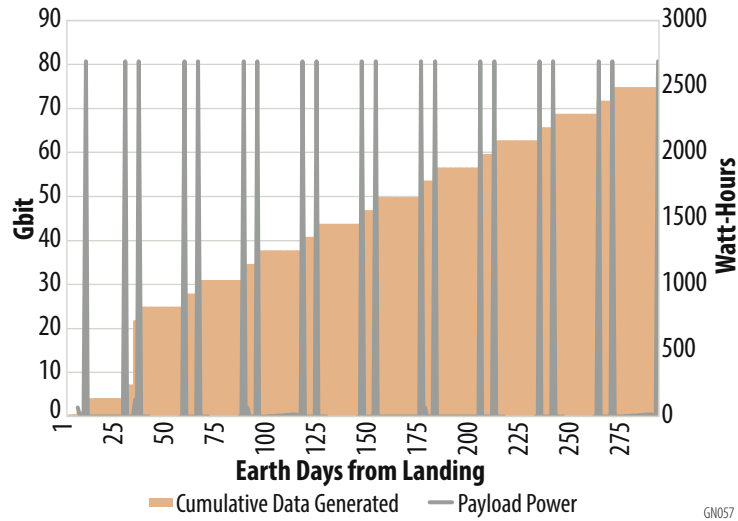


Figure 13: Lunar surface science operations data and power profile. Spikes in payload power represent sample analysis.

The Deep Space Network (DSN) would be used as the primary means for all communications during the flight operations, checkout, commissioning, and surface operations phases. The lander would use Direct-to-Earth (DTE) communication links to forward commands to and receive science and housekeeping data from the lunar surface (**Figure 14**). Throughout landing and checkout, the lander would use continuous DSN coverage; during science operations, the lander would have an approximately 1-hour contact with DSN each Earth day (**Table 9**). Link budgets show 10 Mbps for the lander-to-DSN link, with 5.7 dB of margin.

Table 9: Summary of lunar mission operations and ground data systems.

	Mission Phase 1 Flight ops	Mission Phase 2 Post-landing Checkout	Mission Phase 3 Surface ops
Mission phase duration, weeks	1	2	49
Downlink frequency band, GHz	8.4	8.4	8.4
Downlink Information			
Number of contacts per day	1	1	1 during lunar day 0 during lunar night
Telemetry data rate, kbps	≥10,000	10,000	10,000
Transmitting antenna type and gain, DBi	HGA 30.27	HGA 30.27	HGA 30.27
Transmitter peak power, Watts	17	17	17
Downlink receiving antenna gain, DBi	66.92	66.92	66.92
Total daily data volume, Mb/day	0.064	1,454	3000*
Uplink Information			
Number of uplinks per day	1	1	1 during lunar day 0 during lunar night
Uplink frequency band, GHz	7.2	7.2	7.2
Telecommand data rate, kbps	32	32	32
Receiving antenna type and gain, DBi	LGA -2.0	LGA -2.0	LGA -2.0
*Worst case, full sample cycle			

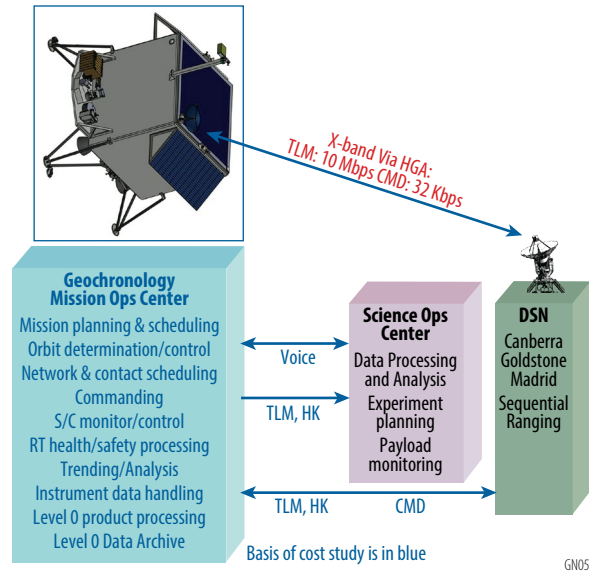


Figure 14: Ground systems architecture for the lunar geochronology lander.

Figure 14 highlights the different functions that would be served by the Mission Operations Center (MOC) and Science Operations Center (SOC). The illustrated MOC & SOC architecture has been used in many successful NASA space missions and would meet the requirements for data volume, DSN contact frequency, and all flight and science operations identified for the studied lunar, Vesta, and Mars missions. Further details of MOC and SOC designs, optimization of functions, Phase E Data products, etc. were not explored in this study and would need to be further specified in future Geochronology mission proposals.

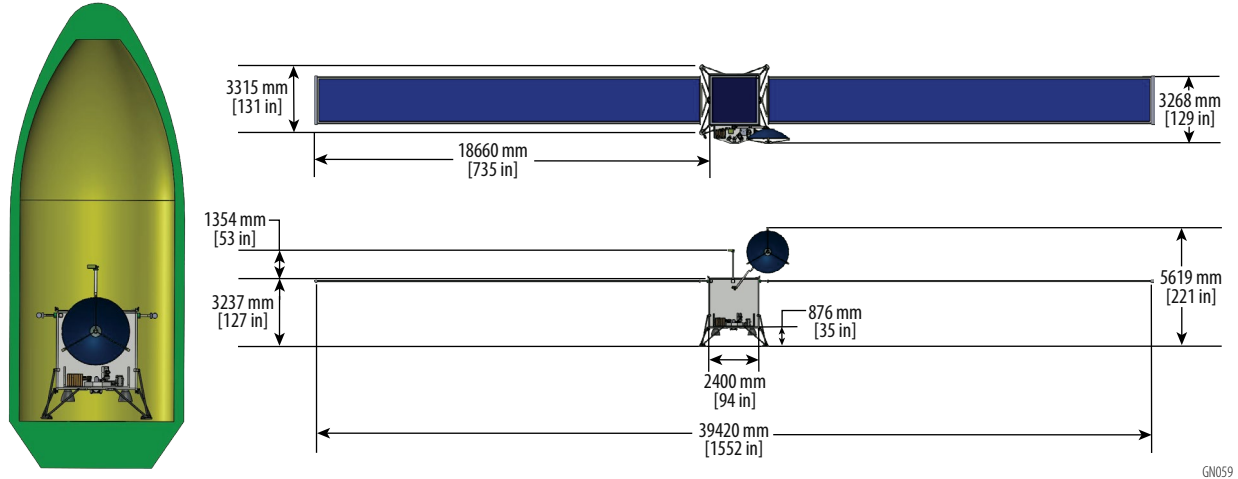
5. VESTA GEOCHRONOLOGY HOPPER MISSION

Hopper Design

The flight system design for a Vesta Geochronology hopper mission (**Figure 15**) is largely based on the lunar Geochronology lander design. **Table 10** summarizes the Vesta hopper mass and power. **Table 11** summarizes the flight system characteristics. The launch vehicle, ACS, avionics, and propulsion subsystems would be identical to the lunar lander concept. The power, communications, structures, and thermal subsystems would be modified for Vesta. The instrument accommodations on the Vesta hopper would be nearly identical to the lunar concept, but the surface operations would be different. **Appendix B3** provides additional spacecraft subsystem details. The lunar mission would use a Falcon 9 Heavy reusable while the Vesta and Mars missions would require the use of the Falcon 9 Heavy expendable.

Vesta, located further from the sun (2.57 AU) than the Moon, receives a lower solar flux of 217 W/m² and rotates more rapidly (5.342 hours). The Geochronology power system configuration would primarily be driven by the low solar flux at Vesta. TJGaAs solar cells with bare cell efficiency of 29.5% and normal solar array losses would generate 36W/m² BOL and 32 W/m² EOL. We baselined two furled flexible solar arrays, each providing 16 m² each of active cell area. The arrays would be oriented at the first landing site (15°N latitude) with wings deployed north and south and rotated to track the sun for the Vesta day, providing 1114W BOL / 990W EOL continuous power for science and avionics.

After science operations at the first landing site were completed, the solar arrays would be furled and the spacecraft would hop to a second site. At the second site (72°S latitude) the arrays would be rolled out to an area of 38m² each and oriented east and west and rotated to offset the angle of latitude.



GN059

Figure 15: Views of the Vesta Geochronology hopper.

Table 10: Vesta hopper mass and power summary.

	Mass			Average Power		
	CBE (kg)	% Cont.	MEV (kg)	CBE (W)	% Cont.	MEV (W)
Structures & Mechanisms	731.4	19	817.2	0	0	0
Thermal Control	34.1	10	37.5	0	0	0
Propulsion (dry mass)	341.8	10	376.0	0	0	0
Attitude Control (Cruise and Descent only)	27.2	10	29.9	27.2	10	29.9
Command & Data Handling	23.1	10	25.4	52.0	10	57.2
Telecommunications	34.3	10	37.7	57.0	10	62.7
Power	155.0	16	180.5	5.0	10	5.5
Total Lander Bus	1,346.9	16	1,548.2	141.2	10	155.3

At the second site (72°S latitude) the arrays would be oriented east and west and rotated to offset the angle of latitude. In this configuration, the arrays would provide a peak power of 2,736W BOL / 2,432W EOL at orbit noon. An additional fixed body mounted solar panel area of up to 4 m² would be included to power avionics for the flight to Vesta. A 37AH, high energy density Li-ion battery would support avionics loads during the Vesta night. The flexible solar array envisioned for use on the Vesta Geochronology mission demonstrated deployment and furling on the International Space Station in 2016 and is TRL 6.

Flight and Surface Operations

The Vesta mission would have a 14-day launch window. The Vesta mission operations would be similar to the lunar mission, with the Falcon 9 Heavy placing the lander into a long cruise and the lander then performing the Vesta orbit insertion and landing, with the addition of a hop phase and a second surface operations phase. Flight operations would include launch, 49-month cruise, and insertion into a 250 km-altitude circular polar Vesta orbit (**Table 12**). Upon arrival at Vesta, the lander would remain in orbit until a terrain map has been developed for the landing site, estimated to be 6 months based on current knowledge of Vesta from the Dawn mission. The period between orbit insertion and landing includes survey and rehearsal phases, similar to the OSIRIS-REx mission (Leonard *et al.*, 2016). The selected landing sites on Vesta are Rheasilvia Central Peak (-71.95 deg, 86.30 deg) and (15 deg, 180 deg), respectively. Landing operations would be similar to the lunar case, including the descent and braking phases and use of TRN.



Table 11: Vesta hopper flight system characteristics.

Flight System Element Parameters	Value/Summary, Units
Design life, months	61
Structure	
Structures material	Aluminum, Composite, Titanium
Number of articulated structures	4
Number of deployed structures	4
Aeroshell diameter, m	N/A
Thermal control	
Type of thermal control used	Louvers/Radiators, Heat Pipes
Propulsion	
Estimated delta-V budget, m/s	3,432 m/s
Propulsion type(s) and associated propellant(s)/oxidizer(s)	Regulated Bipropellant, MMH, NTO
Number of thrusters and tanks	4 Main Engines 12 ACS Engines 1 MMH Tanks 2 NTO Tanks 2 Pressurant Tanks
Specific impulse of each propulsion mode, seconds	293
Attitude Control	
Control method	3-axis
Control reference	Inertial
Attitude control capability, degrees	50
Attitude knowledge limit, degrees	6
Agility requirements	Landing, Terrain Relative Navigation
Articulation/#-axes	2-axis High Gain Antenna 1-axis Solar array gimbals
Sensor and actuator information	0.35 deg sun sensors, 50 arcsec star scanners, 0.005 deg/hr MIMU, LiDAR, Laser Altimeter, Camera
Command & Data Handling	
Flight Element housekeeping data rate, kbps	2,000
Data storage capacity, Mbits	50,000
Maximum storage record rate, kbps	1,000
Maximum storage playback rate, kbps	100,000
Power	
Type of array structure	2 Roll out solar tracking; 1 body fixed
Array size, m ²	76 for worst case 2nd landing site
Solar cell type	TJGaAs
Expected power generation at Beginning of Life (BOL) and End of Life (EOL), W	2432 W / 2736 W for worst case 2nd landing site
On-orbit average power consumption, Watts	379.9
Battery type	Li-ion
Battery storage capacity, amp-hours	37

Table 12: Vesta hopper mission design characteristics.

Parameter	Value
Orbit parameters	250 km circular polar
Mission lifetime	61 mo
Maximum eclipse period	2.5 hr
Launch site	Cape Canaveral, FL
Total lander mass with contingency (includes instruments)	1,720.9 kg
Propellant mass without contingency	4,487.9 kg
Propellant contingency	10 %
Propellant mass with contingency	4,986.5 kg
Launch adapter mass with contingency	97.4 kg
Total launch mass	6,804.9 kg
Launch vehicle	Falcon 9 Heavy Expendable
Launch vehicle lift Capability	10,391 kg
Launch vehicle mass margin	3,586.1 kg
Launch vehicle mass margin (%)	52.7 %



After landing on the surface of Vesta, a five-day lander checkout would be performed, followed by instrument commissioning and initial data collection. Available power would allow the sample analysis sequence (**Section 2**) to occur uninterrupted over its nominal ~24 hour duration, or ~5 Vesta days. Science operations therefore would not be paused during the Vesta night. At a downlink rate 24 Mb/sec and assuming 1 DSN pass/Earth day at 50% efficiency, it would take 4 hours of contact to download the daily average data volume of 346 Mbits. Context imaging would be spread out to maintain consistent lighting and in this concept, assumed to occur within the first 20 Earth days of operations. Surface science would conclude 130 Earth days from landing and data downlink would be complete on Day 142 (**Figure 16**). Surface science operations would be essentially identical at both Vesta sites. A full Earth year is budgeted for the mission to provide margin.

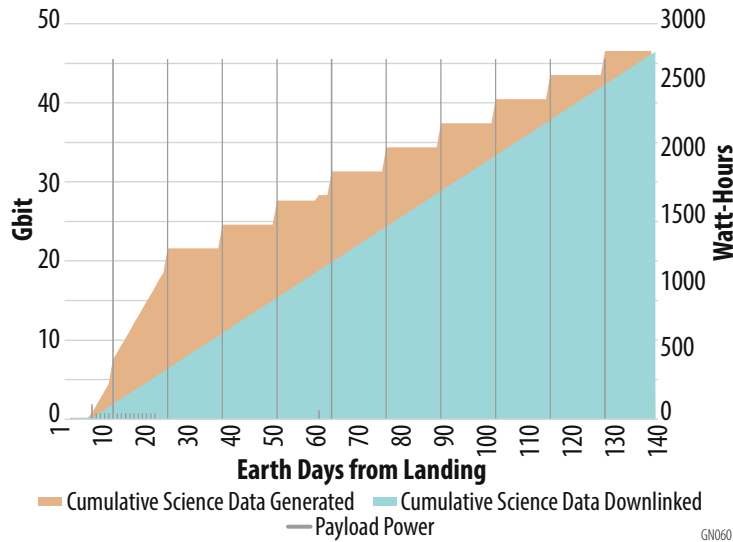


Figure 16: Vesta surface science operations data and power profile (per site).

After the science goals are achieved at Rheasilvia Central Peak, the lander would retract the solar arrays and hop to the Marcia crater site. The hop between Rheasilvia Central Peak and Marcia would have a duration of ~38 minutes. During the landing, checkout, and hop phases, the lander would use continuous DSN coverage. During surface operations, the lander would have a 6-hour contact with DSN each Earth day during the sunlit portion of the Vestan day. Communications are summarized in **Table 13**.

Table 13: Vesta mission operations and ground data systems summary.

	Mission Phase 1 Flight operations	Mission Phase 2 Post-landing checkout	Mission Phase 3 Surface operations
Number of contacts per Earth day	1	1	1
Duration of mission phase, weeks	2,548	2	41
Downlink Information			
Downlink frequency band, GHz	28.4	28.4	28.4
Telemetry data rate, kbps	>50	50	50
Transmitting antenna type and gain, DBi	HGA 53.93	HGA 53.93	HGA 53.93
Transmitter peak power, Watts	100	100	100
Downlink receiving antenna gain, DBi	78.54	78.54	78.54
Total daily data volume, Mb/day	32	2,529	346
Uplink Information			
Number of uplinks per day	1	1	1
Uplink frequency band, GHz	7.2	7.2	7.2
Telecommand data rate, kbps	16	16	16
Receiving antenna type and gain, DBi	HGA	HGA	HGA

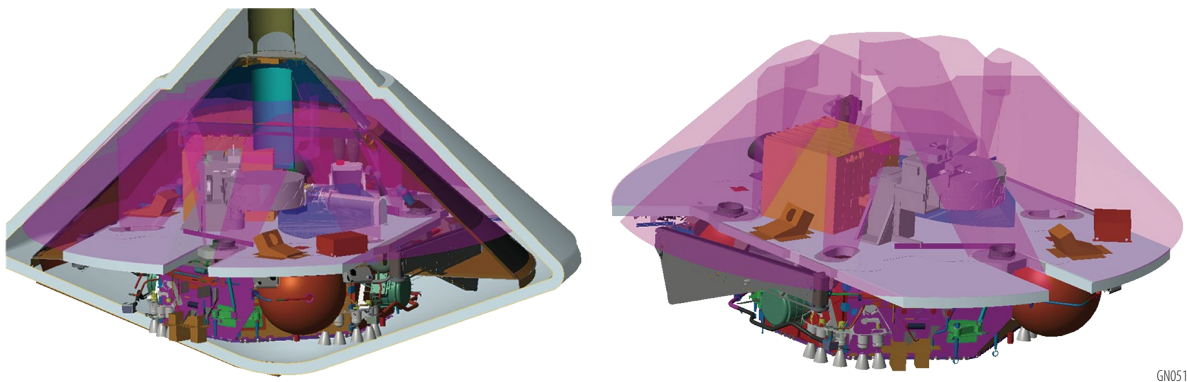


6. MARS GEOCHRONOLOGY LANDER MISSION

Lander Design

The study team worked to implement the full Geochronology payload and operations for Mars version of the mission. Lockheed Martin helped this investigation, leveraging previous cost capped mission lander designs. The lander would be a lander and EDL system based on the successful InSight and Phoenix missions, scaled to land 180 kg of payload and operate for ≥ 180 sols. Specific modifications would include extending the deck and bipods to accommodate the instruments, increasing the aeroshell diameter, adding three MR-104s and a 4-inch stretch (\sim XSS-11 tank) to the descent manifold, and using a Viking-sized parachute to accommodate the larger mass. The mission design considered all Mars launch opportunities between 2025 and 2035 and selected the 2030 window for its ability to target a landing close to $L_s=0$ to maximize operations time before the onset of dust storm season. The Mars Geochronology mission would launch between July 12, 2030 and August 1, 2030 to land on October 30, 2032 at $L_s=73$.

Figure 17 shows the Mars Geochronology lander stowed in the heat shield. To accommodate the increased mass of the Geochronology payload relative to Phoenix or InSight, the deck and aeroshell would be scaled up. Scaling up the aeroshell and launch mass would cause all primary structures to increase in mass (and would increase the size of the aeroshell). Additional details about the Mars Geochronology lander are provided in **Appendix B3**.



GN051

Figure 17: Views of the Mars geochronology lander stowed in the heat shield.

Flight and Mission Operations

Mars entry, descent, and landing would be similar to the systems used for Phoenix and InSight (**Figure 18**). The desired latitude and longitude would be targeted at an altitude of 15 km above the surface of Mars, at which point a parachute would further arrest the spacecraft's momentum. Terrain-relative navigation (TRN) was not considered in this study because the landing site precision did not require it; however, this capability will have been demonstrated on Mars for the Perseverance lander and could be considered in future mission formulation activities.

The lander design would provide ~ 700 W-hr/sol for payload operations, which would pace payload use during Mars surface operations (**Figure 19**). The Geochronology sequence would have the advantage of being able to pause and restart at nearly any point, so the process used to analyze a single sample would be distributed over approximately 4 sols. For the first several samples, full data would be downlinked and examined before retrieving the next sample from the Triage station to ensure the instruments were working properly, sample analysis understood, and results interpretable in the context of the Science Goals. Later in the mission, a data summary or subset might be considered for downlink and review, which could increase the pace of operations, and some efficiency in sample analysis is built into the surface operations shown in **Figure 19**. Context imaging would be divided over ~ 16 sols to ensure consistent lighting conditions, though there would be flexibility in this pacing. The full



PMCS: Geochronology for the Next Decade

20-sample science operations would be complete at Sol 340, at a communication rate of 200 Mbit/Sol, and all data downlinked by Sol 390; 450 sols are budgeted for margin.

Because of the aging Mars orbiter fleet and competition for orbital assets at equatorial latitudes, it is unknown how much communications relay capacity may be available for this mission. A conservative estimate of Mars relay user's guide thresholds might be 50 Mbits/sol, though flight experience is much better and shows considerable margin against this value. Our 200 Mbit/Sol estimate has been consistently demonstrated on Mars Insight (See **Appendix B3, Table B3-29**). At a downlink rate of 50 Mbits/sol, it would take ~1500 sols to complete all science data downlink.

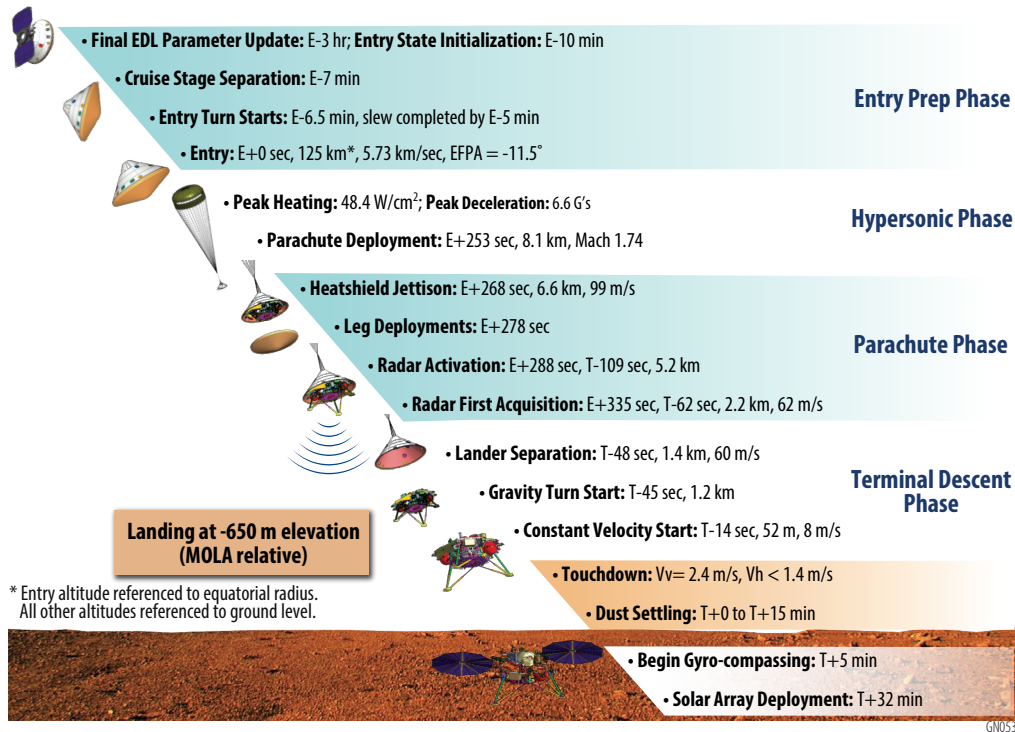


Figure 18: The Mars Geochronology lander entry, descent, and landing sequence would be modeled on previous successful Mars landings.

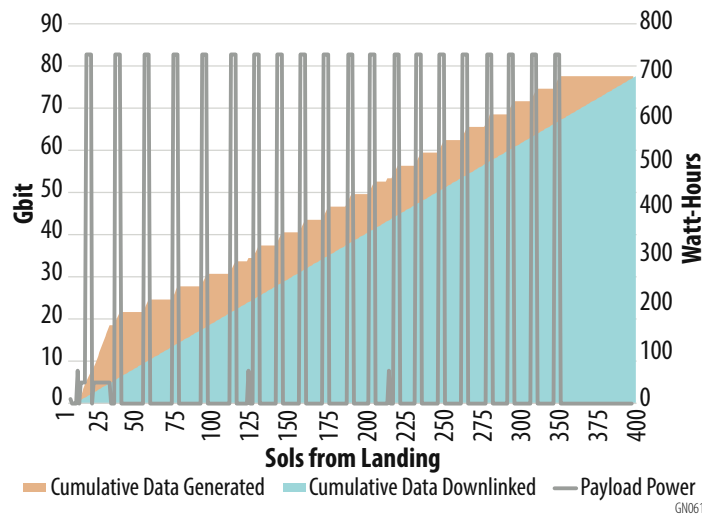


Figure 19: Mars surface science operations data and power profile.



7. DEVELOPMENT SCHEDULES AND COSTS

Mission Development Schedules

The team generated an example or template Geochronology mission schedule leveraging the study work and New Frontiers mission data sets in CADRe. This template schedule is consistent with the average mission Phase B-D durations of prior New Frontiers missions and typical average locations for standard mission-level milestone reviews. Development timeframes for the instruments and spacecraft will be highly influenced by the template schedule. This template schedule assumes all mission enabling subsystem technologies would have been matured to TRL 6 prior to Phase A. The Phase B-D durations, milestone reviews and general schedule flow of the Geochronology template schedule would be compatible with all Geochronology missions studied. The mission schedules would vary slightly in their launch readiness dates and constraints and Phase E elements and durations. A high-level summary schedule and mission phase durations for all Geochronology missions studied is provided in **Schedule Foldout 1**. Additional details about the schedule and assumptions are provided in **Appendix B4**.

Mission Life-Cycle Costs

Table 14 shows the total Geochronology Phase A-E mission costs by major WBS element. All cost estimates, including 50% reserves, are considered preliminary and are commensurate with concept maturity level of the missions studied. All costs estimates assume all component and subsystems technology would have matured to TRL 6 prior to Phase B start. Phase A costs reflect previous New Frontiers Mission Step 2 Concept Study Report (CSR) costs and are the same for all Geochronology mission cost estimates. Phase A costs would be directed to reducing the risks outlined in specific mission proposals, further maturing mission payload and lander element designs, developing the CSR, and performing a Geochronology mission Site Visit. The costs of all mission concepts are within family of a New Frontiers mission classification. The team used parametric cost modeling to estimate costs for instruments and landing systems; both are reported at the 50% confidence level. Wrap factors were used for the other WBS elements and 50% unallocated margin was added to the total. Detailed costing methodology and cost breakdowns for WBS 5 and 6 and Phase E are provided in **Appendix B4**.

Table 14: Geochronology mission cost summary.

WBS Element		Costs \$M FY 2025		
		Lunar	Vesta	Mars
1	Project Management	\$44	\$46	\$38
2	Mission Systems Engineering	\$26	\$27	\$23
3	Safety and Mission Assurance	\$23	\$24	\$20
4	Science	\$19	\$20	\$17
5	Payload	\$232	\$232	\$237
6	Lander Systems	\$325	\$348	\$249
7	Mission Operations	\$18	\$18	\$18
9	Ground Systems	\$40	\$41	\$35
10	Systems I&T	\$33	\$34	\$29
Phase A		\$5	\$5	\$5
Subtotal		\$765	\$795	\$670
50% Phase A-D Reserves		\$382	\$398	\$335
Phase A-D Mission Total		\$1,147	\$1,193	\$1,006
Phase E		\$64	\$201	\$114
25% Phase E Reserves		\$16	\$50	\$29
Phase A-E Mission Total		\$1,228	\$1,445	\$1,149

Summary and Recommendations

Table 15 summarizes all the studied architectural options and how well they would meet the Geochronology science goals and mission drivers. The Vesta architecture option would meet full sample science objectives at multiple sites within a New Frontiers cost cap. For the Moon and Mars, under the study assumptions, cost and payload mass would preclude significant mobility, whether by hopper or rover. New Frontiers-class single-site landers at the Moon and Mars could carry full payloads for ~1 year of operations. Sites may exist where multiple objectives could be met by analyzing more samples.

From these studies, the team concluded that feasible New Frontiers-class missions would exist that could carry a capable instrument payload to conduct *in situ* dating with the precision to answer community-identified Geochronology science goals. Recent NASA investments in *in situ* dating instruments have resulted in payload options that will be ready to infuse into these or other missions



in the next decade. Missions that fit within the New Frontiers-class and include dating by multiple corroborating methods and extensive characterization to increase confidence in results are possible. Additionally, new remote sensing, geologic mapping, and site evaluation efforts have expanded the locations where safe landing sites can access lithologies of interest.

Table 15: A summary of architecture options in this study and assessment against Science Goals and Objectives shows there are multiple compelling mission options in the New Frontiers family. The color code shows how well each architecture option meets the original study goals of measuring radiometric ages on multiples samples using two different methods, conducting measurements at two sites on each body, and meeting a New Frontiers cost cap (green = substantively met; yellow = partially met; orange = did not meet).

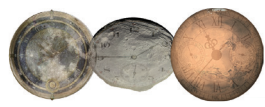
Target	Science Goal	Sample Science	Multiple Sites	Cost Class
Moon	Determine the chronology of basin-forming impacts	Full	Single lander	New Frontiers
	Constrain uncertainty in lunar chronology from 1-3 Ga	Full	Single lander	New Frontiers
	Both	Reduced	Hopper 100s of km	Flagship
Mars	Validate crater-counting ages on Mars	Full	Single lander	New Frontiers
	Bound the epoch of habitability	Full	Single lander	New Frontiers
	Both	Reduced	Rover 10s of km	Flagship
Vesta	Establish vestan chronology	Full	Hopper 100s of km	New Frontiers

Although mobility options were too expensive to fit into the New Frontiers cost cap in this study, the team believes compelling cases can be made for targeted single-site landers on the Moon and Mars to address the individual science objectives in **Section 1.2**. Such missions would also enable a broad suite of geologic investigations, such as basic geologic characterization; geomorphologic analysis; establishing ground truth for remote sensing analyses; analyses of major, minor, trace, and volatile elements; atmospheric and other long-lived environmental monitoring; organic molecule analyses; and soil and geotechnical properties.

It is conceivable the current NASA CLPS program will survive and grow into the next decade. If so, the larger landers could mature into options that could host part or even all of the Geochronology payload. The growth areas needed include total payload mass capability, broader landing site capability, higher reliability, lower risk, and the addition of packages that provide power and thermal solutions (such as the extended operations package part of the LEMS project) for the lunar night. Continuing the CLPS program into the next decade would increase the likelihood that lower-cost communications relays would become available. If the goals and promises of the CLPS program also result in lower payload delivery cost, multiple lunar Geochronology sites could be investigated on the Moon, at lower cost.

Additional technology maturation investments beneficial to this class of mission may include improving the sensitivity of geochronology instruments to enhance age measurement precision, developing end-to-end sample acquisition and handling to feed samples to multiple instruments (*e.g.*, Curiosity, Europa Lander), and expanding flight system technologies to enable spacecraft operations that increase science return (*e.g.*, high-performance computing chips and boards capable of processing terrain navigation and hazard avoidance algorithms, more efficient batteries, thermal technologies that enable night survival, communications throughput, etc.).

In situ geochronology is a feasible way to address community-identified science goals at the Moon, Mars, and Vesta. The Geochronology team advocates for the Decadal Survey panel to include opportunities in the New Frontiers missions list for answering these compelling science questions, with the implementation flexibility to meet them by sample return or *in situ* dating.



Lunar Summary Mission Schedule

Mission Phases & Calendars	FY 2026		FY 2027		FY 2028		FY 2029		FY 2030		FY 2031		Phase	Duration mo.
	CY 2026		CY 2027		CY 2028		CY 2029		CY 2030		CY 31			
	Post Site Visit	Phase B 19 mo.		Phase C 19 mo.		Phase D 13 mo.		Phase E 12 mo.		Ph F				
NASA Reviews & Major Mission Reviews	Site Visit	ATP	SRR/MDR	M-PDR	KDP-C	M-CDR	SIR	KDP-D	PER	PSR	KDP-E	KDP-F	Phase A	9
WBS 5 Payload Development		Payload Req. Review		Payload PDR's		Payload CDR's		Payload SIR/PER		Payload PSR			Phase B	19
Instrument Development		Mission & Payload Elements Requirements Definition		Payload Element PDR Season		Payload Element CDR Season		Instruments Fabrication, Assembly Integration and Test (A&IT)		Funded Schedule Reservem (FSR) 2.5 mo.			Phase C	19
KaRLE		Lander ATP		Lander PDR		Lander CDR		Lander/Environmental		Launch			Phase D	13
CDEX		System Definition		Preliminary Design		Final Design		Lander Fabricate & Test		Lander I&T			Phase E Surface Ops	12
ICPMS		Critical Path											Phase F	1
UCIS		Critical Path											ATP-MSRR	6
Imagers		Critical Path											ATP-MPDR	18
Sample Handling Systems		Critical Path											MPDR-MCDR	11
WBS 6 Lander Systems		Critical Path											MPDR-Payload I&T	20
WBS 10 System I&T		Critical Path											Payload I&T w FSR	5.5
		Critical Path											Systems I&T & Environ Test w FSR	9.25
		Critical Path											Total FSR	4.2
		Critical Path											Total Phase B-D	51

Vesta Summary Mission Schedule

Mission Phases & Calendars	FY 2027		FY 2028		FY 2029		FY 2030		FY 2031		FY 2031-35		FY 35		FY 36		Phase	Months
	CY 2027		CY 2028		CY 2029		CY 2030		CY 31	3/31-3/35		CY 35		CY 36				
	Post Site Visit	Phase B 19 mo.		Phase C 19 mo.		Phase D 13 mo.		Ph E Cruise		Ph E Orbit Survey		Phase E Surface Operations		Ph F				
NASA Reviews & Major Mission Reviews	Site Visit	ATP	SRR/MDR	M-PDR	KDP-C	M-CDR	SIR	KDP-D	PER	PSR	KDP-E	Arrive Vesta	Land Vesta	KDP-F	Phase A	9	ATP-MSRR	6
WBS 5 Payload Development		Payload Req. Review		Payload PDR's		Payload CDR's		Payload SIR/PER		Payload PSR					Phase B	15	ATP-MPDR	18
Instrument Development		Mission & Payload Elements Requirements Definition		Payload Element PDR Season		Payload Element CDR Season		Instruments Fabrication, Assembly Integration and Test (A&IT)		Funded Schedule Reservem (FSR) 2.5 mo.					Phase C	23	MPDR-MCDR	11
KaRLE		Lander ATP		Lander PDR		Lander CDR		Lander/Environmental		Launch					Phase D	18	MPDR-Payload I&T	20
CDEX		System Definition		Preliminary Design		Final Design		Lander Fabricate & Test		Lander I&T					Phase E Cruise	49.25	Payload I&T w FSR	5.5
ICPMS		Critical Path													Phase E Orbit Survey	6	Systems I&T & Environ Test w FSR	9.25
UCIS		Critical Path													Phase E Surface Ops	12	Total FSR	9.25
Imagers		Critical Path													Phase F	1	Total Phase B-D	51
Sample Handling Systems		Critical Path																
WBS 6 Lander Systems		Critical Path																
WBS 10 System I&T		Critical Path																

Mars Summary Mission Schedule

Mission Phases & Calendars	FY 2026		FY 2027		FY 2028		FY 2029		FY 2030		FY 2030-2032		FY 2033		FY 2034		Phase	Months
	CY 2026		CY 2027		CY 2028		CY 2029		CY 2030		7/30 - 9/32		CY 2032		CY 2033			
	Post Site Visit	Phase B 19 mo.		Phase C 19 mo.		Phase D 14 mo.		Ph E Cruise		Phase E Operations 464 Earth Days		Ph F						
NASA Reviews & Major Mission Reviews	Site Visit	ATP	SRR/MDR	M-PDR	KDP-C	M-CDR	SIR	KDP-D	PER	PSR	KDP-E	Land Mars	KDP-F	Phase A	9	ATP-MSRR	6	
WBS 5 Payload Development		Payload Req. Review		Payload PDR's		Payload CDR's		Payload SIR/PER		Payload PSR					Phase B	19	ATP-MPDR	18
Instrument Development		Mission & Payload Elements Requirements Definition		Payload Element PDR Season		Payload Element CDR Season		Instruments Fabrication, Assembly Integration and Test (A&IT)		Funded Schedule Reservem (FSR) 2.5 mo.					Phase C	19	MPDR-MCDR	11
KaRLE		EDL ATP		EDL PDR		EDL CDR		EDL Fabricate & Test		EDL I&T					Phase D	14	MPDR-Payload I&T	20
CDEX		System Definition		Preliminary Design		Final Design		EDL Fabricate & Test		EDL I&T					Phase E Cruise Ops	27.5	Systems I&T & Environ Test w FSR	9.25
ICPMS		Critical Path													Phase E Surface Ops	15.25	Total FSR	4.2
UCIS		Critical Path													Phase F	1	Total Phase B-D	51
Imagers		Critical Path																
Sample Handling Systems		Critical Path																
WBS 6 Entry Decent Landing (EDL) Systems		Critical Path																
WBS 10 System I&T		Critical Path																



Appendix A – Acronyms

ACS.....	Attitude Control System
ADC	Analog-to-Digital Converter
AH.....	Amp Hour
AO	Announcement of Opportunity
AOS	Acquisition of Signal
ARM	Advanced RISC Machines
ATC.....	Analog Telemetry Card
ATP.....	Authority To Proceed
BCM	Battery Charge Module
BM	Braking Maneuver
BOL	Beginning of Life
CAD	Computer Aided Design
CADRe	Cost Analysis Data Requirement
CBE.....	Current Best Estimate
C_d	Coefficient of Drag
CDEX	Chemistry and Dating Experiment
CDF.....	Cumulative Distribution Function
CDR	Critical Design Review
CCSDS.....	Consultative Committee for Space Data Systems
C&DH	Command and Data Handling
CEMA.....	Cost Estimating, Modeling & Analysis
CLPS	Commercial Lunar Payload Services
CM.....	Configuration Management
CoM.....	Center of Mass
CMD	Command
CML.....	Concept Maturity Level
Co-I	Co-Investigator
COTS.....	Commercial Off The Shelf
CSR.....	Concept Study Report
DALI	Development and Advancement of Lunar Instrumentation
dB	Decibel
DDOR.....	Delta Differential One-Way Ranging
DEA	Digital Electronics Assembly
ΔV	Delta Velocity
DOI.....	De-Orbit Insertion
DPDT	Double Pull Double Throw



DPU.....	Data Processing Unit
DSN.....	Deep Space Network
DTE.....	Direct to Earth
DTN.....	Delay-tolerant networking
EDL.....	Entry, Descent, and Landing
EOL.....	End of Life
FDIR.....	Fault detection, isolation, and recovery
FEC.....	Forward Error Correction
FETS.....	Field Effect Transistors
FSW.....	Flight Software
FTE.....	Full Time Equivalent
Gbits.....	Giga bits
Gbps.....	Giga bits per second
GSM.....	Generic Switch Module
GMSL.....	Gaussian Minimum Shift Keying
GN&C.....	Guidance Navigation and Control
GPR.....	Goddard Procedural Requirements
GSFC.....	Goddard Space Flight Center
HA.....	Hazard Avoidance
HGA.....	High Gain Antenna
HK.....	Housekeeping
HgCdTe.....	Mercury Cadmium Telluride
HPS.....	High Performance Spacecraft Computing
ICPMS.....	Inductively Coupled Plasma Mass Spectrometry
IR.....	Infrared
IMU.....	Inertial Measurement Unit
IOAG.....	Interagency Operations Advisory Group
I&T.....	Integration and Testing
JAXA.....	Japan Aerospace Exploration Agency
JPL.....	Jet Propulsion Laboratory
K-Ar.....	Potassium-Argon
KArLE.....	Potassium-Argon Laser Experiment
Kbps.....	Kilobits per second
KE.....	Kinetic Energy
kg.....	Kilogram
kN.....	Kilo Newtons
LADEE.....	Lunar Atmosphere and Dust Environment Explorer



LAMO	Low Altitude Mapping Orbit
LA-MS	Laser Ablation-Mass Spectrometry
LARIMS	Laser Ablation – Resonance Ionization Mass Spectrometry
LIDAR	Light Detection and Ranging
LDPC	Low-Density Parity-Check
LEAG	Lunar Exploration Analysis Group
LEMS	Lunar Environment Monitoring Station
Li	Lithium
LIBS	Laser-Induced Breakdown Spectroscopy
LOI	Lunar Orbit Insertion
LRD	Launch Readiness Date
LVDS	Low Voltage Differential Signaling
LVPS	Low Voltage Power Supply
m	Meter
M3	Moon Mineralogy Mapper
MAHLI	Mars Hand Lens Imager
MatISSE	Maturation of Instruments for Solar System Exploration
Mbps	Mega bits per second
MCC	Motor Controller Card
MDL	Mission Design Lab
MIC	Multi-Interface Cards
MPU	Mechanism and Propulsion Unit
MEL	Master Equipment List
MEPAG	Mars Exploration Program Analysis Group
MET	Mission Elapsed Timer
MEV	Maximum Expected Value
mm	Millimeter
MMX	Martian Moons Explorer
MOC	Mission Operations Center
MOCET	Mission Operations Cost Estimating Tool
MOLA	Mars Orbiting Laser Altimeter
MOMA-MS	Mars Organic Molecule Analyzer – Mass Spectrometer
MS	Mass Spectrometer
MRC	Mechanism Release Card
m/s	Meters per second
MSL	Mars Science Laboratory
MSPS	Million Symbols Per Second



MSSS	Malin Space Science Systems
NASA	National Aeronautics and Space Administration
NF	New Frontiers
NICM	NASA Instrument Cost Model
NGRTG	Next-Generation Radioisotope Thermoelectric Generator
OSIRIS-REx	Origins, Spectral Interpretation, Resource Identification, Security, Regolith Explorer
PanCam	Panoramic Camera (on the Mars Exploration Rovers)
PDC	Propulsion Drive Card
PDR	Preliminary Design Review
PI	Principal Investigator
PICASSO	Planetary Instrument Concepts for the Advancement of Solar System Observations
PIDDP	Planetary Instrument Definition and Development Program
PM	Project Management
ppmw	Parts per Million by Weight
PSE	Power System Electronics
PSP	Parker Solar Probe
QMS	Quadrupole Mass Spectrometer
Rb-Sr	Rubidium-Strontium
REE	Rare Earth Element
RF	Radio Frequency
ROM	Rough Order of Magnitude
SA	Solar Array
SAM	Sample Analysis at Mars
SARM	Solar Array Regulation Module
SBAG	Small Bodies Assessment Group
SBC	Single Board Computer
S/C	Spacecraft
SBIR	Small Business Innovation Research
SEER-H	System Evaluation & Estimation of Resources - Hardware
SEU	Single Event Upset
SMA	Sample Manipulation Arm
SMD	Science Mission Directorate
SOC	Science Operations Center
SPLICE	Safe and Precise Landing - Integrated Capabilities Evolution
SQPSK	Staggered quadrature phase-shift keying
SRR	System Requirements Review
SSR	Solid-State Recorder



STM.....	Science Traceability Matrix
STMD	Space Technology Mission Directorate
STTR.....	Small Business Technology Transfer
S/W	Software
SPENVIS	Space Environmental Effects and Education System
SWIR	Shortwave Infrared
SWRI	Southwest Research Institute
TAGCAMS	Touch-and-Go Camera System
TJGaAs.....	Triple Junction Gallium Arsenide
TLM.....	Telemetry
TMCO.....	Technical, Cost, Management & Other
TMR.....	Triple Modular Redundant
TOF	Time of Flight
TRL.....	Technology Readiness Level
TRN	Terrain Relative Navigation
UART	Universal Asynchronous Receiver/Transmitter
UCIS	Ultra Compact Imaging Spectrometer
ULA	United Launch Alliance
USN	Universal Space Network
V	Volts
VNIR.....	Visible and Near-Infrared
W	Watt
WATSON	Wide Angle Topographic Sensor for Operations and eNginering camera
WBS	Work Breakdown Structure



Appendix B1 – Science Team Study Report

1.1 Science Background

Geochronology, or the determination of absolute ages for geologic events, underpins many inquiries into the formation and evolution of planetary bodies and our Solar System. The bombardment chronology inferred from lunar samples has played a significant role in the development of models of early Solar System and extrasolar planet dynamics, as well as the timing of volatile, organic, and siderophile element delivery. Improvements and expansion of known absolute ages would yield new insight for many scientific questions. For example, absolute ages of ancient and recent magmatic products provide strong constraints on the dynamics of magma oceans and crustal formation, and the longevity and evolution of interior heat engines and distinct mantle/crustal source regions. Absolute dating also relates habitability markers to the timescale of evolution of life on Earth. In addition, terrestrial laboratory radiometric and cosmic ray exposure dating of lunar samples paired with crater size-frequency distributions of the geologic units associated with the samples has enabled the calibration of lunar cratering chronology functions. These functions allow the determination of model ages for unsampled geological units across the Moon and have been adapted for application on other terrestrial planetary bodies for which no samples of known provenance currently exist. Major advances in planetary science can thus be driven by geochronology in the next decade, calibrating body-specific chronologies and creating a framework for understanding Solar System formation, the effects of impact bombardment on life, and the evolution of planetary surface environments and interiors.

Absolute ages for formative events in the timelines of multiple worlds were a desire in both the 2003 and 2013 Planetary Science Decadal Surveys. However, given the limitations of then-existing technologies, only sample return was considered a viable method for geochronology and was therefore used as a driver for recommending and implementing sample return missions such as OSIRIS-REx and Mars Sample Return (MSR). Visions and Voyages (2013) also recommended a New Frontiers-class mission to return samples from the Moon's South Pole-Aitken Basin to address the bombardment history of the inner Solar System. Such a mission was proposed multiple times by several groups (*e.g.*, Duke, 2003; Jolliff *et al.*, 2012; Jolliff *et al.*, 2017), and selected twice for Phase A study, but no mission concepts have yet been selected for implementation. Though there are many factors in play when making mission selections, sample return within the New Frontiers program seems to be accomplishable from small bodies (*e.g.*, OSIRIS-REx). There may be additional costs and technical risks in realizing a robotic sample return mission to bodies with significant gravitational wells or those requiring supplemental mission elements (such as a communications satellite to enable lunar farside communication). Further challenging the sample return model, the number of chronologically significant geologic terrains across the inner Solar System far exceeds our financial capacity and projected technological ability to collect, cache, and return samples from all of them, much less do the same across the outer Solar System.

The recommended mission lists in both prior Decadal Surveys reflect the reality that for those decades sample return was regarded as the only way to provide reliable and interpretable geochronological constraints on planetary bodies. However, as a community, we routinely use *in situ* geochemical (*e.g.*, APXS, ChemCam) and isotopic techniques (*e.g.*, mass spectrometers). While these may yield less sensitive or precise measurements than terrestrial laboratories, they are still sufficient to resolve major science questions associated with planetary environments throughout the Solar System where sample return is prohibitive due to financial, technical, and/or other challenges. In the last two decades, NASA has also invested significantly in the development of innovative *in situ* dating techniques. Instrument maturation programs (*i.e.*, Planetary Instrument Concepts for the Advancement of Solar System Observations (PICASSO), Maturation of Instruments for Solar System Exploration (MatISSE), and Development and Advancement of Lunar Instrumentation (DALI)) will have brought the technology readiness levels (TRL) of instruments that can access complementary radiogenic isotopic systems (K-Ar and Rb-Sr) to TRL 6 by the time of the next Decadal Survey. Sample collection and handling systems have also matured, while informed/autonomous operational scenarios have evolved. Thus, the time is right to consider how the precision achievable with *in situ* geochronology (taken here to be ± 200 million years, or Myr) can advance important science goals for the next Decadal Survey. This



report presents dedicated Geochronology mission concepts incorporating these technologies to address science objectives for the Moon, Mars, and small bodies such as Vesta. The aim of this study is to investigate whether an *in situ* dating mission would be a viable alternative (or addition) to sample return missions in the upcoming Decadal Survey to accomplish longstanding geochronology goals within a New Frontiers envelope.

1.2 Science Goals and Objectives

Characterizing the timing and relationships between geological processes across the Solar System is a major goal of planetary science. Our existing understanding of inner Solar System chronology is rooted in defining geologic epochs on each body, and then assigning absolute ages to those epochs by scaling the lunar production and chronology functions to different planetary conditions (Hartmann and Neukum, 2001; Hiesinger *et al.*, 2016a; Neukum *et al.*, 2001; Schmedemann *et al.*, 2014; Strom and Neukum, 1988). Unfortunately, the lunar cratering record itself is unconstrained prior to the apparent bombardment of 3.9 Gyr ago (basin-forming epoch), and suffers from a roughly billion-year uncertainty between 1 and 3 Ga (“middle ages”) (*e.g.*, Bottke and Norman, 2017; Chapman *et al.*, 2007; Fassett and Minton, 2013; Hartmann *et al.*, 2000; Robbins, 2014; Ryder *et al.*, 2000; Stöffler *et al.*, 2006; Zellner, 2017). Geologic epochs on different planetary bodies have been defined by events that have little apparent relation to each other (**Figure B1-1**). Therefore, refining the lunar crater chronology curve and calibrating body-specific chronologies is critically important for comparing planetary histories, contextualizing Solar System dynamics, and developing an interplanetary perspective on the evolution of planetary surfaces, interiors, and habitable environments. We chose three specific Science Goals to investigate in this study:

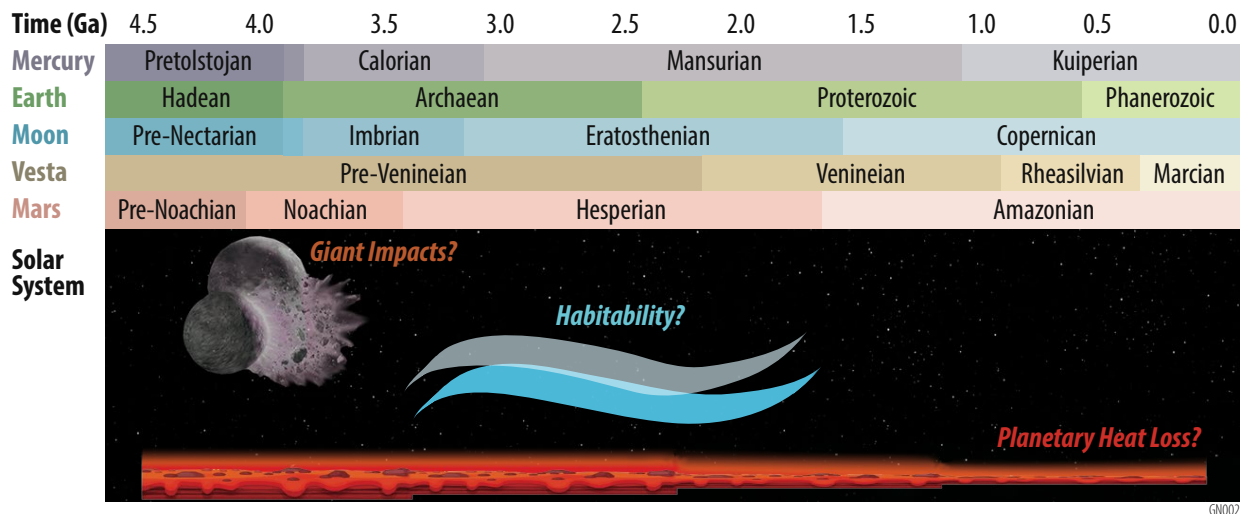


Figure B1-1: The current geologic age boundaries on the inner planets have little relationship to each other, making it challenging to interpret geologic evolution within a solar system context. Uncertainty in the relationship between each geologic era could be resolved using *in situ* dating.

- **Determine the chronology of basin-forming impacts** to constrain the time period of heavy bombardment in the inner Solar System, and thus address fundamental questions related to inner Solar System impact processes and chronology. Ascertaining the early flux of impactors on all planetary bodies across the inner and outer Solar System is necessary to understand the Solar System’s dynamical evolution and processes occurring on nascent planetary bodies.
- **Reduce the uncertainty for inner Solar System chronology** in the “middle ages” (1-3 Ga) to improve models for planetary evolution, including volcanism, volatiles, and habitability. Lunar cratering chronologies are not well-calibrated in the period between 1 and 3 Ga, because there are no



returned samples of known provenance with these ages. This deficit propagates into uncertainties in the chronology systems for the Moon and other bodies, resulting in large uncertainties in the history and duration of volcanic activity.

- **Establish the history of habitability across the Solar System.** Absolute ages of potentially habitable terrains would help resolve when localized environments within the inner Solar System could have supported biological activity.

From these overarching objectives, multiple targeted science objectives can be formulated that would lead to progress on these goals, potentially addressable by a range of missions, including sample return or *in situ* investigations. In this study, we specifically focus on *in situ* methodologies, so we first adopt a quantitative measurement requirement. The 2015 NASA Technology Roadmap calls out *in situ* dating as an important investment (National Aeronautics and Space Administration, 2015), suggesting a minimum precision better than $\pm 5\%$ for rocks 4.5 billion years old (Ga) (approximately ± 200 Myr, 2σ), and a desired precision of $\pm 1\%$ for 4.5 Ga rocks (or about ± 50 Myr, 2σ). For this study, we took the minimum precision requirement to develop specific cases where this level of uncertainty would resolve Science Objectives specific to the Moon, Mars, and Vesta, tracing to LEAG, MEPAG, and SBAG goals documents (Table B1-1), described more fully below.

Table B1-1: Summary of Science Goals and Objectives for the Moon, Mars, and Vesta.

Body	Science Goal	Science Objective	Traceability ¹
Moon	Chronology of basin-forming impacts	Moon 1: Establish the chronology of basin-forming impacts by measuring the radiometric age of samples directly sourced from the impact melt sheet of a pre-Imbrian lunar basin	Test the cataclysm hypothesis by determining the spacing in time of the creation of lunar basins
	Reduce the 1-3 Ga uncertainty	Moon 2: Establish the age of a “middle-aged” lunar basalt to correlate crater size-frequency distributions with crystallization age	Determine the age of the youngest and oldest mare basalts and Establish a precise absolute chronology
Mars	Reduce the 1-3 Ga uncertainty	Mars 1: Establish the age of an extensive and well-exposed Hesperian martian lava terrain and extend the lunar geochronologic framework to Mars	Determine the petrogenesis of martian igneous rocks in time and space
	Habitability across the Solar System	Mars 2: Establish the epoch of martian habitability by measuring the radiometric age of Noachian clay-bearing units	Determine the evolutionary timeline of Mars
Vesta	Calibrating body-specific chronologies	Vesta: Establish the radiometric ages of Vestan samples with well-established provenance	Determine the timing of events in the early Solar System and Use the distribution of compositions and ages of small bodies in the Solar System to make testable predictions about observable parameters in forming planetary systems

¹ Scientific Context for the Exploration of the Moon, LEAG Advancing Science of the Moon Special Action Team, MEPAG Goals Document, iMOST, Small Bodies Analysis Group Science Goals document (Beaty et al., 2019; Lunar Exploration Analysis Group, 2017; MEPAG, 2020; National Research Council, 2007; SBAG, 2016)

Moon 1: Establish the chronology of basin-forming impacts by measuring the radiometric age of samples directly sourced from the impact melt sheet of a pre-Imbrian lunar basin.

The leading model for lunar impact history, which is still under debate (*e.g.*, reviews by Bottke and Norman, 2017; Hartmann, 2019), includes a pronounced increase in large impact events around 3.9 Ga (Ryder, 1990; Tera *et al.*, 1974). The factors that led to this “terminal lunar cataclysm” would likely have also led to large impacts throughout the inner Solar System as a “late heavy bombardment,” influencing the habitability potential of Earth and other bodies. Though recent work on lunar samples has identified the possibility that lunar sample collections may be biased by repeated (albeit unintentional) sampling of Imbrium basin ejecta at the various Apollo landing sites (Haskin *et al.*, 1998; Norman *et al.*, 2010; Schaeffer and Schaeffer, 1977), constraints also come from impact ages of meteorites derived from asteroid parent bodies (Bogard, 2011; Jourdan, 2012; Swindle *et al.*, 2014). H-chondrites show



a prominent group of ^{40}Ar - ^{39}Ar ages between ~ 3.5 and 4.0 Ga, and eucrites and howardites derived from Vesta cluster at ~ 3.5 and 3.8 – 4.0 Ga (Bogard, 2011; Cohen, 2013; Kennedy *et al.*, 2013). The impact-melt clasts in howardites likely formed by high-velocity collisions (Cohen, 2013; Marchi *et al.*, 2013). Few rocks older than 3.9 Ga exist on the Earth, so samples from the basin-forming epoch are scarce, but this bombardment would have occurred on an early Earth with an atmosphere, oceans, and continents, and may have influenced the course of biologic evolution (Maher and Stevenson, 1988; Mojzsis and Harrison, 2000). Large impacts may have had a similar influence on potential biologic evolution on other planets (*e.g.*, Mars or even Venus), early in their history.

Dynamical models that support an early bombardment of the Moon assume lunar bombardment is strongly linked to the broader processes describing the endgame of planet formation (*e.g.*, Morbidelli *et al.*, 2018). A successful model must not only explain what is found on the Moon, but also constrain early bombardment on Mercury, Earth, Mars, the asteroids, and potentially bodies in the outer Solar System as well. These models, which extend from the gas-dust dynamics of forming disks to giant planet migration, may now be invoked to understand our Solar System as well as systems of exoplanets around other stars. As we seek to better link what we know about these other systems, we are left with a fundamental question: Is our Solar System typical or anomalous? One of the best ways to address this question is to determine what processes occurred and their timing and duration in the early Solar System, and then compare these findings to what is observed in planetary systems that are currently forming around other stars. A key test of these dynamical models is whether the terrestrial planets and asteroid belt experienced a relative “lull” in impacts between formation and later bombardment.

Geologic observations of surface morphologies and geophysical data of the Moon have revealed more than 50 distinct basins and possibly more candidate basins whose surface expressions have presumably been obscured by subsequent impact resurfacing (Featherstone *et al.*, 2013; Frey, 2011; Neumann *et al.*, 2015; Spudis, 1993; Wilhelms, 1987). Cross-cutting relationships of ejecta and crater densities allow reconstruction of a relative time-sequence of the basins that have a clear surface expression (Fassett *et al.*, 2012; Wilhelms, 1987). Despite increasingly precise measurements of the isotopic ages of lunar samples and progressively detailed geological studies of the lunar surface using high-resolution imaging, absolute ages of almost all lunar basins are either unknown or poorly constrained. In large part, this reflects our inability to link individual lunar samples with specific basins or craters with a high degree of confidence, even when carefully collected by astronauts. Stöffler and Ryder (2001) provide a comprehensive summary of the radiometric dates of lunar samples available at that time and their interpretation of the ages of key nearside basins such as Imbrium, Serenitatis, Crisium, and Nectaris; however, more recent work has called into question the geologic interpretation of samples from Serenitatis, Crisium, and Nectaris, pulling the pin on the only constraints on a lunar cataclysm (*e.g.* Norman, 2009; Norman *et al.*, 2010; Spudis *et al.*, 2011).

There is general agreement in the community that Imbrium formed at 3.9 Ga, though the exact age depends on the geologic sample, radiometric dating system, and interpretation – ranging from 3.86 ± 0.09 Ga to 3.91 ± 0.09 Ga to 3.934 ± 0.03 Ga (Deutsch and Stöffler, 1987; Merle *et al.*, 2014; Norman *et al.*, 2010; Stöffler and Ryder, 2001). These differences are too small to resolve with *in situ* dating; instead, we seek a basin age that could be distinguished from 3.9 Ga to serve as a second pin in lunar basin stratigraphy. The key to a cataclysm is the duration of bombardment; even in a case where results might be in between the two extremes (for example, 4.0 ± 0.2 Ga), we can use that interval to infer a moderately strong form of the cataclysm. In addition to measurement precision, careful site selection and sample characterization are keys to remote identification of impact-melt samples derived from a pre-Imbrian basin and distinguishing them from KREEP-rich Imbrium samples. Furthermore, once we identify the impact melt-derived material *in situ*, characterize its elemental composition and mineralogy (for geological context), and determine its age, we may be able to find the same materials in the returned sample collection and/or lunar meteorite inventory. Such samples could then be used to measure a more precise age on the same lithology in a terrestrial laboratory, leveraging *in situ* geochronology to acquire returned-sample-quality data.

In situ dating precision of ± 200 Myr with 95% confidence (2σ) may be sufficient to date the impact-melt sheet of lunar basins thought to be significantly older than the Imbrium basin, which would place



them either within the canonical cataclysm (3.9 Ga) or as part of a declining bombardment in which most impacts are 4.2 Ga or older.

Moon 2: Establish the age of a very young lunar basalt to correlate crater size-frequency distributions with crystallization ages

Calibration of the post-basin epoch lunar chronology is based on Apollo and Luna samples from lunar mare basalt flows and younger benchmark craters where samples yield radiometric formation and exposure ages, including Copernicus, Tycho, North Ray, Cone, Autolycus and Aristillus craters (Stöffler and Ryder, 2001). Higher-resolution imaging of the Moon made available by the Lunar Reconnaissance Orbiter, Kaguya, and Chang'E-1 has been used to update the crater size-frequency distribution (CSFD) ages of key lunar geological units for the calibration of the cratering chronology and to check and improve existing crater statistics (Haruyama *et al.*, 2009; Hiesinger *et al.*, 2003; Hiesinger *et al.*, 2016b; Hiesinger *et al.*, 2012; Robbins, 2014; Wang *et al.*, 2015; Williams *et al.*, 2014b). Detailed CSFD measurements have also been made for the selection of young basalt units that could be favorable landing sites for sample return or *in situ* measurements (Hiesinger *et al.*, 2003; Stadermann *et al.*, 2018; Qian *et al.*, 2018). However, different authors' chronologies yield a large range of possible absolute model ages for units with cumulative crater frequencies that place them in the middle part of the chronology function (*e.g.*, van der Bogert and Hiesinger, 2020). For example, crater density results differ by a factor of 2-3 for the area surrounding North Ray crater; factoring in other landing sites, a revised chronology would predict that a lunar surface previously dated at 3 Ga may have an updated model crater age as young as 1.9 Ga (Robbins, 2014).

Under the "classic," sample-based lunar chronology, mare volcanism is thought to have reached its maximum volumetric output between 3.8 and 3.2 Ga (Shearer and Papike, 1999). New crater-density relationships imply peak volcanism may have extended for an additional 1.1 billion years (through 2.5 Ga) (Braden *et al.*, 2014; Hiesinger *et al.*, 2000; Qiao *et al.*, 2017), a finding that would dramatically revise our understanding of the thermal evolution of the lunar mantle, abundance and distribution of radioactive heat-producing elements (*e.g.*, K, U, Th), and release of indigenous lunar volatiles (Needham and Kring, 2017). One or more *in situ* age measurements of lunar basalts significantly younger than 3.2 Ga would greatly improve the calibration of lunar cratering chronologies within this time frame. Not only would this refine our understanding of the duration of lunar mare basalt volcanism, but the improved lunar calibration would propagate forward to improved chronologies for other planetary bodies.

In situ dating precision of ± 200 Myr with 95% confidence (2σ) would be sufficient to reduce the uncertainty in absolute model ages derived from crater size-frequency distribution measurements to no more than 20% of the current uncertainty shown between different lunar chronology functions.

Mars 1: Establish the age of a well-exposed Hesperian martian lava terrain to correlate crater size-frequency distributions with crystallization ages

Ages for ancient and recent magmatic products provide strong constraints on the dynamics of magma oceans and crustal formation, the longevity and evolution of interior heat engines and mantle/crustal source regions. On Mars, the "middle ages" are geologically rich, including the cessation of abundant volcanism and the formation of hydrated minerals (Ehlmann *et al.*, 2016a). Revision of the middle Mars chronology might imply that these processes could have lasted for a billion additional years, revising models for martian thermal evolution and allowing a longer era of abundant volatiles and potential habitability. Given the current uncertainties in the absolute age of volcanic surfaces of middle and especially younger martian age, there is a large uncertainty in the history and duration of interior processes on Mars. While InSight will shed light on the current state of the martian interior, the path to the present remains poorly constrained. For example, a factor of two uncertainty in the absolute ages of Hesperian lava plains has large implications for the source of internal heat responsible for driving interior processes through time. Increasing uncertainty in the absolute ages for the Amazonian results in even less awareness of how interior processes and associated igneous activity



evolved over the past ~2-3 Ga. Critical advances in understanding planetary volcanism at benchmark igneous provinces, coupled with elemental and mineralogical analyses, would provide geologic context and critically distinguish mantle sources.

The Mars Sample Return program represents an extensive effort that may bring back samples from materials within Jezero Crater. The selected Perseverance landing site, Jezero crater, contains an areally extensive, well-cratered unit overlying the basin fill material and embaying the delta outcrops, though the origin of the unit as volcanic or sedimentary is not yet established (Goudge *et al.*, 2018; Rogers *et al.*, 2018; Shahrzad *et al.*, 2019). Investigations with the rover payload will determine if this unit is volcanic, volcanoclastic, or sedimentary; returned samples from the unit may determine its age – perhaps a crystallization age that would be relatable to the martian crater flux function, or the formation and exposure age of the detrital precursors. Evaluating these possibilities will begin early next year as Perseverance lands and begins investigating. However, even if the Jezero samples represent a major step forward in correlating absolute ages and relative crater density, there is a bigger, broader issue in knowing the systematic factors that relate martian crater spatial density to age throughout its history. By analogy to the lunar curve, multiple data points on Mars are needed to provide a reference frame for understanding whether scaling factors between the Moon and Mars are correct and how the changing Solar System dynamical environment affected both planets.

In situ dating precision of ± 200 Myr (2σ) is sufficient to radically improve our understanding of Mars' volcanic history, with relevance to geodynamics and interior cooling, assign widely-separated igneous provinces absolute ages, and examine the compositional progression of igneous sources with time. Perhaps most importantly, such a dating precision should enable the pinning of absolute ages associated with geologic history in middle and late martian history, thereby significantly reducing the current $\sim 2\times$ uncertainty in the timing of late aqueous activity and the persistence of past habitability conditions. This would also provide a direct test of the quality of the adaptation of the lunar cratering chronology to Mars.

Mars 2: Establish the epoch of martian habitability by measuring the radiometric age of Noachian clay-bearing stratigraphies

Incomplete knowledge of absolute martian geochronology limits our ability to understand the timing of martian evolutionary milestones (*e.g.*, Cohen *et al.*, 2019; Doran *et al.*, 2004; Tanaka *et al.*, 2014), specifically when Mars changed from a habitable environment to its present state (Ehlmann *et al.*, 2016a). For example, we are not confident of the absolute age of the Noachian-Hesperian boundary, where a warm, wet Mars became arid (Bibring *et al.*, 2006), or whether it occurred before, after, or concurrent with the Imbrium impact on the Moon and the oldest intact rocks on Earth. Thus, martian climate change cannot yet be put into the context of Solar System history and the evolution of life on Earth. Results from the MSL Curiosity rover mission have demonstrated that aqueous habitable settings existed on Mars in surface environments well into the Hesperian and maybe later (Cohen *et al.*, 2019; Grotzinger *et al.*, 2015; Martin *et al.*, 2017). Yet, most models for the evolution of the martian climate suggest conditions were not likely favorable for surface habitable environments in much of the Hesperian, much less into the Amazonian. Knowing whether such environments could be older or younger than predicted in the current chronology is critical to understanding how the habitability of the planet evolved over time. Absolute age constraints with the precision of *in situ* dating would help resolve the large uncertainty in when Mars changed from a habitable environment to its present state, and, importantly, allow the extension of this chronology to other parts of the planet via crater density statistics.

In situ dating precision of ± 200 Myr (95% confidence, or 2σ) is sufficient to constrain the timing of Noachian unit formation. This would provide an important anchor for crater spatial densities of terrains hosting geologic evidence from Mars' most habitable period. For example, the broadest epoch boundaries for the Late Noachian period span ~ 3.9 - 3.6 Ga (Michael, 2013) in different crater chronology models. Resolving the age of, for example, a late Noachian clay-bearing unit would test whether crater spatial densities from Mars have been correctly modeled. This has concomitant implications



for reconciling the timing of the development of life on Earth (~3.5 Ga age for the oldest confirmed fossil evidence) and hypothesized spikes in early impact bombardment (~3.9 Ga).

Vesta: Establish the radiometric ages of vestan samples with well-established provenance

The Main Asteroid Belt represents a large reservoir of bodies that have largely been devoid of endogenic processing since very early in Solar System history. However, they have experienced intense, often disruptive impact events, some of which contributed to the flux of material that impacts the inner planets. The asteroids also serve as probes of the dynamical history of the Solar System, but except for laboratory-derived ages of a few meteorites that originated from mostly unknown asteroids (*e.g.*, Bogard, 2011; Swindle *et al.*, 2014), our knowledge of the chronology of the Main Belt relies either on dynamical models or, for the few asteroids that have been visited by spacecraft, on model crater retention ages based on extrapolations of the lunar chronology curve applied to a set of bodies in a different dynamical environment.

One of the best targets for calibrating timescales is Vesta, the second-most massive object in the Main Belt. Vesta has a basaltic crust, and basaltic meteorites linked to Vesta by the Dawn mission and by earlier spectroscopic work have crystallization ages within a few million years of the birth of the Solar System. Hence Vesta is an object that formed early and then survived intact until the present, serving as a witness to all that has occurred in the Main Belt since more than 4.5 Ga. The major basin ages on Vesta have wildly different inferred ages, depending on which lunar chronology curve is applied. The giant basins Rheasilvia and Veneneia may be nearly as old as the large lunar basins, with the formation of Rheasilvia proposed at 3.4 ± 0.1 Ga and Veneneia somewhat older (Schmedemann *et al.*, 2014), or possibly as young as 1-2 Ga (Schenk *et al.*, 2012). Meanwhile, most radiometric ages for meteorites derived from Vesta are >3.47 Ga (Bogard, 2011; Cohen, 2013; Kennedy *et al.*, 2013), although there are some feldspar grains with ages only slightly older than 1 Ga (Lindsay *et al.*, 2015).

In situ dating precision of ± 200 Myr (95% confidence, or 2σ) is more than sufficient to constrain Vesta's geologic timescale by dating key stratigraphic craters and contiguous geologic terrains. Given the large disparity in ages derived by different logical assumptions, this level of precision would not only reveal the ages of key basins but would also set firm constraints on the impactor flux estimates used throughout the Main Asteroid Belt. These measurements would also provide a direct test of the quality of the adaptation of the lunar versus asteroid cratering chronologies to Vesta and the rest of the Main Asteroid Belt.

1.3 Science Requirements

Having selected several science goals and objectives across the inner Solar System addressable with *in situ* dating, we constructed a Science Traceability Matrix (STM) (**Table 1** in the **Main Report**) to establish the measurement and mission requirements needed to address these goals.

Radiometric dating, or the process of determining the age of rocks from the decay of their radioactive elements, has been in widespread use for over half a century. Dating techniques require measuring the parent and daughter isotopes in a pair (for this study, Rb-Sr and K-Ar) to determine when a rock closed to addition or loss of its radioactive elements or their decay products. Many rocks are amenable to Rb-Sr and K-Ar dating in terrestrial labs, including igneous rocks, phyllosilicates/clays, and sulfates. Each mineral can record a different event in the rock's history, from initial crystallization to alteration events *e.g.*, impact or weathering. A radiometric age needs context, requiring accurate and precise measurements of the isotopic systems and adequate knowledge to interpret that analysis.

Each of this Study's defined Science Objectives can be met using the same set of measurement requirements. The overarching requirement in all cases is to measure the age of the desired lithology. To accomplish this, several measurements and associated observations are needed, including a) using radiometric chronology to directly measure the age of samples derived from the target lithology with precision better than or equal to ± 200 Myr (95% confidence, or 2σ); b) contextualizing the desired lithology using petrology, mineralogy, and/or elemental chemistry; and c) relating the measured lithology age to crater counting of the lithology's terrain.



Additionally, the composition of the surface unit must be determined to place its lithology into a regional and global context; this would ensure the measured samples represent the desired source region and support interpretation of the measured age. A notional payload would thus be able to distinguish different lithologies, for example by a) mapping mineralogy (*e.g.*, olivine, pyroxene, iron oxides, plagioclase, and aqueous alteration minerals including phyllosilicate, sulfate, carbonate, and other hydrated salts); b) imaging the samples at the microscale to determine grain size distributions, textural relationships, etc.; c) measuring the major- and trace-element geochemistry of the samples to establish parentage, trace geological processes, and constrain the lithologic evolution; and d) contributing to understanding the geology of the landed site and its lithologic units, and relating them to maps and crater counts determined from remote sensing.

For this study, measurement requirements for all goals and objectives are met by carrying a single notional payload comprising representative instruments (**Table B1-2**). All instruments, except the inductively coupled plasma mass spectrometer (ICPMS), will be TRL 6 in 2023 (the start of the next Planetary Decadal Survey), and no additional development costs nor technology maturation would be required before a mission Phase B (see **Appendix B2** for technical details about payload elements). Additional technology maturation investments that would be beneficial to this class of missions might include improving the sensitivity of geochronology instruments to improve age measurement precision, developing end-to-end sample acquisition and handling to feed samples to multiple instruments (*e.g.*, Curiosity, Europa Lander), and refining flight system technologies (*e.g.* peak power, night survival, communications throughput, etc.) to enable the spacecraft operations to increase science return.

Table B1-2: Notional payload for geochronology mission concept studies.

Measurement Requirement	Measurement	Payload Element
Geochronology	Rb-Sr geochronology, mineralogy	CDEX
	K-Ar geochronology, major- and minor-element composition	KArLE
Sample & site context	Trace-element geochemistry	ICPMS
	Mineralogy	UCIS
	Visible/color imaging and micro-imaging	Panoramic and microimagers
Sample Handling	Acquire, prepare, and introduce samples to analysis instruments	PlanetVac and other hardware

To make significant advances in creating a geochronologic framework, *in situ* geochronology must yield ages that are both precise and accurate – that is, the measurement techniques must yield small uncertainties on the calculated age, and that age must be recognizable and interpretable as a geologic event. Multiple groups have made substantial progress on bringing some of these techniques closer to flight implementation; a comprehensive review of developments and proposals appears in Cohen *et al.*, 2019. Armed with this knowledge, we are able here to narrow our consideration to a subset of potential instruments, their precision, and potential for implementation. For many planetary materials, it may be possible to measure ages using more than one system, which is common practice in terrestrial laboratory geochronology. Agreement between multiple chronometers increases confidence in the interpretation of the geologic events experienced by the sample, though disagreement does not negate the inherent value of each measurement. We therefore baselined two independently-developed *in situ* dating instruments that together can access both the Rb-Sr and K-Ar radiometric systems.

Geochronology analyses should be paired with other observations that provide context and further enhance the science return of a prospective mission. The uncertainty in a geochronology measurement is influenced not only by technological capabilities but also by the complexity (*e.g.*, mineralogy, alteration history, etc.) of the planetary material and geologic setting being investigated. Thus, sample selection, location, and geological context are just as important as the analytical methodologies that enable radiometric dating. Remote imaging (from visible, or VIS, to mid-infrared, or IR, wavelengths) and trace-element compositional measurements (enabled by ICPMS) are included in the baseline payload so that samples identified for processing are well-understood and suitable for dating. Verifying that selected samples are associated with cohesive surface units, rather than deposits not definitively



representative of the specific locality under investigation, further enables interpretation of radiometric ages and deduction of relationships to mapped surface features.

Mission requirements include the need to identify and collect samples, measure the radiometric age of multiple (minimum ~10) samples, corroborate isochron ages among samples analyzed independently for statistical confidence, and conduct this operations scenario at multiple sites located hundreds to thousands of km from each other. As we progressed in this Mission Design space, we considered the implications of these choices on payload resource requirements, spacecraft mobility, and mission design.

1.4 Sampling Statistics

The number of samples that need to be collected and analyzed is a function of three things: a) how many aliquots of the lithology of interest are needed to ensure statistical confidence in assigning an age to the lithology; b) how much of the lithology of interest makes up the regolith at the landing site; and c) how many rocks of correct size (0.5 – 2 cm in diameter) exist in the regolith.

The number of aliquots of any given lithology required for confidence in the measured age of that lithology depends on multiple factors, including the accuracy and precision of the instrumental measurement and the cooperation of the samples themselves. Geochronology work in terrestrial laboratories takes these factors into account by running duplicates or triplicates of key samples to ensure that the sample behavior and age agree and the quoted precision on the age is a combination of the measurement uncertainties and deviation among samples. For the science questions *in situ* geochronology missions hope to answer on the Moon, Mars, and Vesta, which are complicated by overprinting impact events and other factors, running multiple aliquots of key samples increases the likelihood of obtaining robust age constraints. Increasing the number of samples decreases the mean residual error and calculated standard deviation, potentially enabling the age of the geologic event to be interpreted with better precision than any individual measurement (*e.g.*, Coutts *et al.*, 2019), though we do not take this potential improvement in precision into account for this study. Analyzing multiple aliquots would also ensure mitigation of secondary events that might be recognized in geochronology data, for example, thermal or aqueous alteration. If results disagree among three aliquots of a lithology, the analysis shows that they were not all reset by the same event, or that there is some other complicating factor involved. The exact number of samples required to obtain robust statistical results depends on the exact question being asked; for this study, we adopt 10 samples as the requirement to achieve robust counting statistics that could improve the precision on the interpreted age by a factor of three if all samples yielded the same measured age.

Geologic setting and context are both crucial for missions intending to sample specific lithologies. Regolith formation on all bodies works to vertically and laterally mix materials to varying degrees, but geochemical signatures of different terrains are preserved, as observed from orbit. Sample return missions have shown that the most prominent component of any regolith sample is the substrate on which it formed, so samples collected from it would contain the lithology of interest. For example, the Apollo 17 mission landed on the edge of the Serenitatis basin with the intent to sample Serenitatis ejecta and young basalt (Spudis and Pieters, 1991). The Lunar Excursion Module landed directly on the basaltic surface of Mare Serenitatis, so there is little ambiguity about the origin of the high-Ti basaltic material seen in the returned samples (**Figure B1-2**) – that is, landing on the basalt yielded samples of the underlying basalt (Rhodes *et al.*, 1976). Though the regolith is developed primarily from the substrate, vertical and lateral mixing does occur. The disagreement in the community over whether the poikilitic impact melt breccias brought back from the ejecta-emplaced South Massif represent the Serenitatis impact (Dalrymple and Ryder, 1996; Schmitt *et al.*, 2017; Zhang *et al.*, 2019) is an example of the complexities involved when interpreting the origin of samples from ejecta deposits. However, away from large basin ejecta sites, regolith mixing on the Moon and Mars is primarily local.

In the Geochronology mission payload, we include instruments that would assist in distinguishing materials and associating them with remotely sensed data for the landing site and nearby units to enable identification of outliers that might be associated with fragments derived from more distant impact events. To further support science objectives, we have chosen candidate landing sites that are



well characterized from orbit and are geologically homogeneous with a lithology of interest that is clearly identifiable via remote sensing. For this study, we chose sites where our current understanding of remote sensing and geologic setting make it probable that the majority of the samples retrieved would represent the lithology of interest (**Section 1.5**). Nonetheless, this assumption would need to be thoroughly vetted and refined for any proposed mission at any site. For conservatism in this study, we include a factor of three on the sample estimates to account for potential mixing. This factor drives the number of samples that need to be collected and examined in triage.

Both geochronology instruments require rocks of 0.5 - 2 cm in diameter to conduct their analyses. To bound the total amount of sample that needs to be collected to yield enough rocks in this size fraction, we considered data from landing sites on the Moon and Mars and from a vestan meteorite. It is worth noting here that robotic sampling of these smaller rocks, either vertically or laterally, is an excellent way to ensure sampling the complete lithologic diversity at any given site; comparing small rocks separated from rake samples to samples carefully chosen by astronauts shows the same range of composition and frequency at the Apollo 17 site (**Figure B1-2**).

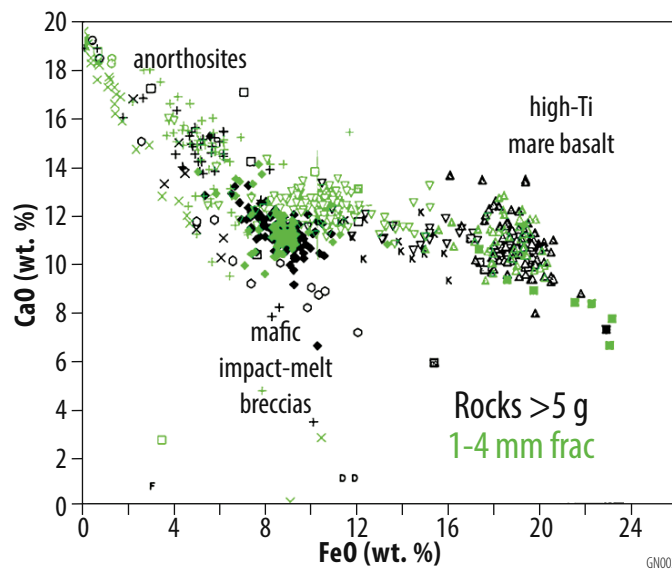


Figure B1-2: Samples derived from raking and sieving lunar regolith represent the complete geologic diversity of any individual site, as shown by the composition and range of 1-4 mm rocks sieved from rake and soil samples at the Apollo 17 site, which completely overlap that of individually-collected lunar rocks weighing >5g (adapted from data in Jolliff et al., 1996).

There are significant challenges to accurately estimating the frequency of 0.5 - 2 cm-sized rocks from returned lunar soil samples. Generally, lunar soil is defined as the size fraction <1 cm; therefore, samples were treated differently across the 1-cm boundary (*e.g.*, McKay *et al.*, 1991). The Apollo 11 soils clumped together during sieving, so the recorded grain-size frequency distributions for the Apollo 11 samples skew towards coarser fractions and are not representative of the lunar surface (Carrier, 1973). For later missions, soils were passed through a 1-mm sieve before distribution to investigators for grain-size frequency distribution analyses, meaning that the recorded >1-mm size fraction data was variable. Aliquots of soil dedicated to grain size-frequency distribution analysis typically only included fragments <1 mm and reported size fractions as percentages, so the results cannot be extrapolated to larger grain sizes (Graf, 1993).

Several researchers used photographs of the lunar surface to obtain the size-frequency distribution of boulder-sized rocks on the lunar surface. This type of image analysis is limited by image resolution (*i.e.*, only boulders equal to or greater than the size of the pixels will be apparent). At the limits of the resolution of the image, where boulder size approaches pixel size, there is a roll-off in the number of countable blocks. Block counts at the Surveyor landing sites from orbital imagery follow a power law and rapidly roll-off as the resolution limit is approached (**Figure B1-3**), which was ~2.5 m from Lunar

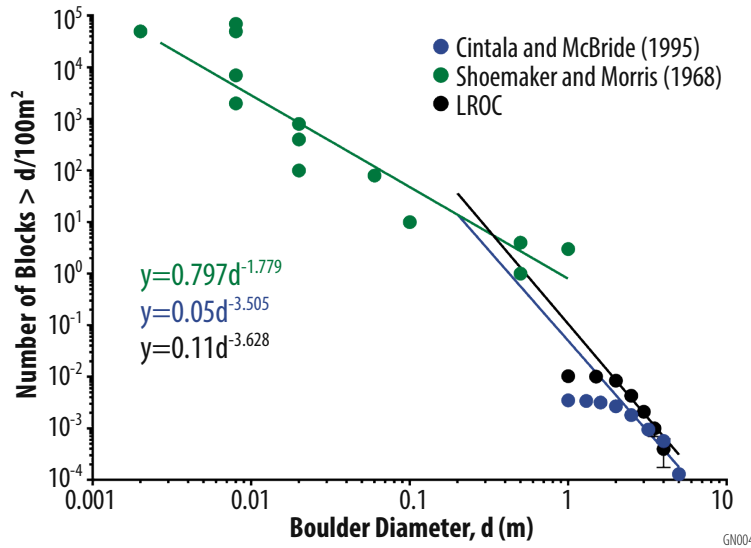


Figure B1-3: Comparison of grain size distribution estimates using data from the Surveyor I landing site. Roll-offs in block count using both Surveyor images and LROC NAC images are due to resolution limitations of the data.

Orbiter photography (Cintala and McBride, 1995) and 0.5 m in Lunar Reconnaissance Orbiter images (Watkins *et al.*, 2019), both of which are too coarse to confidently extrapolate to cm-sized rocks. A much smaller area (essentially within the radius of the lander footpads) allowed grain sizes to be counted down to 1 mm at the Surveyor 1 and 3 sites using television images; these images encompass the grain size of interest and show thousands of fragments of appropriate size at the surface (Shoemaker and Morris, 1970) (**Figure B1-4**). Their depth distribution is unknown, but if the surface density were extrapolated as uniform at depth, a volume of 0.6 L would be sufficient to yield 30 rocks 0.5 cm or larger (**Table B1-3**).

Because lunar soil statistics do not scale up and boulder counting does not easily scale down, we undertook a more accurate estimation of rock abundance with depth using the Apollo core samples. Drive tubes were used to collect regolith core samples from all Apollo sites, representing a secular sampling of the upper ~0.5 m of regolith across different lunar geologic settings, which is analogous to material a robotic mission would be expected to sample. Therefore, for this study, we counted fragments in core dissection diagrams of Apollo drive tubes, counting all fragments with long axis dimensions 0.5 - 2 cm as a proxy for rock diameter (**Table B1-4**). The mission drive tubes used to collect the cores were 2 cm in diameter for Apollo 11, 12, and 14 and up to 4 cm in diameter for the later missions. Historical core sketches only capture the axial plane of the core sample; considering this geometry and the tube diameter, our method should capture most 0.5 - 2 cm rocks in the 2-cm cores but may undercount rocks in the larger, 4-cm diameter tubes. The 76001/2 double-drive tube currently being dissected under the ANSGA program will have a complete 3D CT scan that will make this method much more accurate.

Among the 21 drive tubes and double drive tubes examined, the total number of rocks in the desired size range (0.5 - 2 cm) ranged from one to 72 (**Table B1-4**). Very mature soils have fewer large fragments while immature mare surfaces and landslide deposits range to the higher numbers. Surface age likely dominates this variability, because young surfaces have had less exposure to bombardment and are thus less broken down (*i.e.*, grain sizes are larger). The number of fragments per volume using this method yields slightly lower abundances than simply extrapolating the surface count to a uniform distribution with depth. We adopted 0.6-1.2L as the amount of regolith that would yield 30 samples, including 100% margin on our estimates (**Table B1-3**).



Table B1-3: Rock size-frequency counts for lunar cores counted using sketches and scans (Allton, 1978; Fruland et al., 1982; Fryxell and Heiken, 1971; Lindsay et al., 1971; Meyer, 2016; Nagle, 1979, 1980a, b, 1982; Ryder and Norman, 1980).

Sample	Volume (cm ³) *	Maturity	Rock Count		
			0.5-1.0 cm	1.0-1.5 cm	1.5-2.0 cm
10004	41.8		6	0	0
10005	29.9		5	0	0
12026	60.6		3	0	0
12027	53.4	Submature-mature	5	0	0
12025 & 12028	128.8		5	1	0
14210 & 14211	118.1	Mature	16	4	0
14220	51.8	Mature	10	0	0
14230	39.3	Submature	3	0	0
15009	377.0	Submature	43	8	1
15007 & 15008	711.3	Submature	17	3	0
15011 & 15010	841.9	Maturity decreases with depth	38	8	6
60010 & 60009	738.9		32	9	3
60014 & 60013	792.9		5	0	1
64002 & 64001	824.4		12	3	0
68002 & 68001	782.9	Range	59	13	0
70012	231.2		4	1	1
76001	433.5		1	0	0
73002	276.5		7	2	2
74002 & 74001	857.0		1	3	0
79002 & 79001	644.7		16	8	6

*Calculated using recovered sample core length, assuming 100% filling of the core tube.

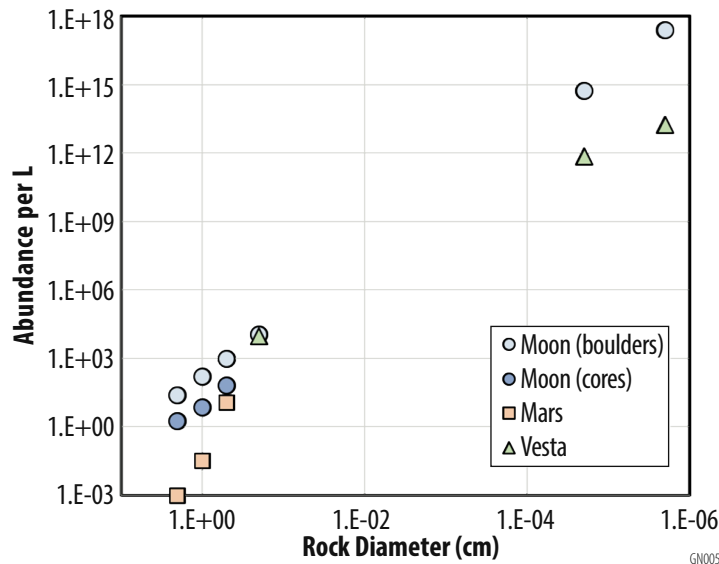


Figure B1-4: Compilation of grain size-frequency distributions for 0.5-2 cm rocks in the mature regolith of the Moon, Mars, and Vesta.



Table B1-4: Rock size-frequency calculations for the Moon, Mars, and Vesta, and resulting volume estimated excavation.

	Diameter (cm)	Surface density (m ⁻²)	Volume density (L ⁻¹) ¹	Volume required for 30 rocks (L)
Moon (boulders) ²	0.5	9.89E+03	9.83E+02	2.58E-02
	1.0	2.88E+03	1.55E+02	
	2.0	8.39E+02	2.43E+01	
Moon (cores) ³	0.5	—	4.42E+01	6.17E-01
	1.0	—	3.93E+00	
	2.0	—	5.00E-01	
Mars (hollows) ⁴	0.5	5.00E+02	1.12E+01	2.68E+00
	1.0	1.00E+01	3.16E-02	
	2.0	1.00E+00	1.00E-03	
Vesta ⁵	2.0E-06	—	1.78E+13	Similar to lunar
	2.0E-05	—	7.07E+11	
	2.0E-01	—	9.71E+03	

¹ calculated using (surface density)^{3/2}
² Shoemaker and Morris (1968)
³ median values from 21 core samples
⁴ order-of-magnitude visual estimates from InSight images
⁵ Pun et al. (1988)

The martian regolith is much different from the lunar case. The Moon has been subjected to billions of years of meteorite bombardment, creating a meters-thick, fine-grained regolith with few areas of exposed bedrock. In contrast, the martian surface has been dominated by aeolian scouring and transport during the Amazonian, constantly exposing bedrock in some places and covering other areas with sediment. Previous mission landing sites have shown that in areas of active or recent deflation (*e.g.*, the plains of Gusev crater, the lower flanks of Mt. Sharp in Gale crater), surfaces are covered by a scattered to continuous lag of coarse rock fragments too large to be transported by the wind. In many instances, fragment size distributions are as expected by impact fragmentation, with fragment composition consistent with derivation from local bedrock/materials (Grant *et al.*, 2006). For example, the Spirit landing site on the Gusev plains is dominated by a regolith of basaltic materials punctuated by variable, broadly circular patches of finer sediments trapped and filling small impact craters (dubbed “hollows”). Because the plains often display a lag of fragments too large for aeolian transport, access to fragments of suitable size (>0.5 cm) for delivery to geochronology instruments would be straightforward and likely involve minimal processing.

However, the Spirit and InSight landing sites have a large number of small, sediment-filled craters whose fragments are dominated by accumulation of finer materials capable of aeolian transport. These fragments are derived via mostly local impacts of varying size that create and eject an inventory of fines that can be transported by the wind into the source or other nearby craters where it can be sequestered. The majority of infilling occurs relatively soon after a crater forms and is related to transport of sediment produced by the impact, though prevailing winds dictate that some is transported in directions that will not contribute to infilling of the parent crater. Infilling continues over time as nearby impacts create additional inventories of fines, some of which can be transported downwind and trapped in other craters. Because the wind is the dominant transport mechanism over the past ~1-2 Ga on Mars, these sediments are quite fine (less than 1 cm) and may be less suitable for delivery to geochronology instruments. Nevertheless, there is also a lesser component of coarser fragments (mostly cm-scale) that contributes to fill and is the result of direct emplacement of ejecta fragments during formation of nearby craters (mostly tens to hundreds of meters away). At the InSight landing site, the concentration of coarser fragments on the west side of Homestead Hollow and referred to as Rocky Field is probably an example of ejecta from a nearby crater (Grant *et al.*, 2020; Warner *et al.*, 2020).



Given that several prior landings on Mars (Opportunity, Spirit, InSight) have ended up in small, sediment-filled craters, a mission without active hazard avoidance capability has to ensure access to enough cm-scale fragments in the event that landing should occur within a sediment-filled crater. Information from the fill within Homestead Hollow at the InSight landing site and Laguna Hollow at the Spirit landing site suggests this should be possible. At the InSight landing site, the lander workspace contains ~500-600 fragments larger than 0.5 cm/m², a handful fragments >1.0 cm/m², and only ~1 or so fragment >2.0 cm/m², on the hollow floor (Weitz *et al.*, 2020) (**Figure B1-4**). However, on the west side of the hollow (“behind” the lander), there are greater numbers (~2-4×) of cm-scale fragments in Rocky Field. An important caveat to these numbers is that the rocket motors stripped off dust and fines from the surface that likely concentrated these coarser fragments to some degree. For comparison, the fragment size distribution in Laguna Hollow in Gusev Crater (where there was no rocket motor blast) is broadly similar to that at Homestead Hollow, but there are slightly more larger fragments that increase in number toward the rim, and the fragments are slightly more elongate.

If the fragments were distributed uniformly with depth in the same density as their surface abundance, 2.7 L of material would yield ~30 fragments that are ~0.5 cm or larger in diameter (**Table B1-3**). In this case, a PlanetVac device would be appropriate for collecting the samples (though importantly, PlanetVac should be tested to ensure it can work with an indurated sediment/duricrust at the near-surface, as is seen at the InSight landing site). However, if the fragments represent a lag deposit and are not uniformly abundant at depth, as appears to be the case at InSight as a result of rocket motor blast during landing, then an arm to reach and acquire surface and near-surface samples may be more appropriate to retrieve fragments for analysis.

For Vesta, we looked at the particle size-frequency distribution in howardites, lithified regolith samples presumed to come from Vesta. A particle size-frequency distribution was reported by Pun *et al.* (1998) for the meteorite Kapoeta, but only for grains 0.2 cm and smaller. Nevertheless, plotting the Kapoeta grain size-frequency distribution in **Figure B1-4** shows the Kapoeta data at small grain sizes are a close approximation to lunar size-frequency data extrapolated to the grain sizes of interest. We may therefore be confident that the estimates developed for the lunar and martian cases would also be appropriate for the vestan regolith. Furthermore, Vesta does not have the aeolian processes that Mars does, so we would expect the variability from site to site to be more like the lunar case, and would not expect the complications that are potentially present on Mars.

1.5 Site Selection

To drive the engineering constraints for these studies, we needed to consider candidate landing sites for each body. Although these are notional landing sites based on our identified science questions, we made an effort to ensure that these sites were representative of the range of sites that the science community might desire for a mission with geochronology capabilities (**Table B1-5**).

We assessed candidate lunar sites for mission safety using LRO data, specifically LROC NAC images, NAC Digital Terrain Models (DTMs), and Diviner rock abundance data. NAC-scale DTMs (5 m/px) were used to assess the topography, slopes, and roughness. Roughness was measured in terms of the Terrain Ruggedness Index (TRI), which is calculated by determining the mean elevation difference between adjacent pixels in the DTM (Riley *et al.*, 1999; Wilson *et al.*, 2007). TRI values (unitless) were generated using an open source Geospatial Data Abstraction Library (GDAL) script (GDAL/OGR contributors, 2019). Because TRI values are relative, the range of values in an area vary depending the scale of features and the range of topography. Given the range of TRI values present at our landing sites, we define values <10 as safe. We also used NAC DTMs to generate slope maps for each landing site, with low slope areas that are suitable for landing (<15 deg) shown in black. Finally, Diviner data were used to assess rock abundance for each area. Diviner rock abundance (DRA) measures the cumulative areal fraction of the surface covered by rocks >1 m (Bandfield *et al.*, 2011), with low values indicating surfaces with a low percentage of rock coverage. Suitable landing sites are those with low TRI (<10), low slopes (<15 deg), and low DRA values. Features of concern for the hazard assessment include impact craters, boulders, slopes, and shadows. Use of NAC images with resolution 0.5 m/px permits identification of boulders 2-3 m in diameter and larger. Using images with different



illumination geometry, especially low-sun images, smaller boulders can be identified and confirmed using their elongated shadows. Diviner data can also be used to assess rock abundance over large areas and to support the LROC NAC data. Information derived from the LROC data and supported by Diviner data made it possible to place landing ellipses in areas with a suitably high probability of a lander not encountering a mission-ending hazard. With terrain-relative navigation and/or active hazard avoidance and small landing ellipse capabilities, landing sites can be selected with a very high probability of safe landing. We considered only nearside sites to maintain direct-to-earth communication capabilities.

Table B1-5: Summary of potential landing sites considered for this study.

Body	Science Goal	Site	Location	Characteristics
Moon	Establish the chronology of basin-forming impacts by measuring the radiometric age of samples directly sourced from the impact melt sheet of a pre-Imbrian lunar basin	Peirce Crater	18.26°N, 53.35°E	18-km diameter crater, excavates noritic Crisium impact-melt floor. Several-km landing ellipses exist.
		Rosse Crater	17.9°S, 35.0°E	11-km diameter crater, excavates noritic Nectaris impact-melt floor. Several-km landing ellipses exist.
	Establish the age of a “middle-aged” lunar basalt to correlate crater size-frequency distributions with crystallization age	P60	21°N, 40°W	Multiple flow units as young as ~1 Ga. Widely accessible, safe landing sites exist.
		Le Monnier	26.86°N, 30.08 W	57-km diameter crater embayed by Mare Serenitatis; basalt age ~2.4 Ga. Several-km landing ellipses exist.
Mars	Establish the age of an extensive and well-exposed Hesperian martian lava terrain and extend the lunar geochronologic framework to Mars and Establish site epoch of martian habitability by measuring the radiometric age of Noachian clay-bearing units	Nili Fossae Trough	74.481°E, 21.0108°N	Provides access to representative sections of widely distributed units, including Noachian units with clay minerals and Hesperian lavas. Ellipse was proposed and vetted for Mars 2020 Landing Site selection.
		NE Syrtis	77.0767°E, 17.8034°N	Access to a broad range of Noachian and Hesperian materials: clays, carbonates, sulfates, lavas. Landing ellipses not fully vetted for Mars 2020
		Mawrth	21.1343°W, 24.5537°N	Access to representative sections of widely distributed units including Noachian clay-bearing stratigraphies and Hesperian dark mantling materials. Ellipse was proposed and vetted for Mars 2020 Landing Site selection.
Vesta	Establish the radiometric ages of Vestan samples with well-established provenance	Rheasilvia Basin	71.95°S, 86.30°E	Flat, high-standing plateau at basin central peak enables access to basin material. Current best image resolution ~70 m/px.
		Marcia Crater	15°N, 180°E	Marcia is a key stratigraphic marker, location sited among a variety of geologic units spanning geologic history. Current best image resolution ~70 m/px.

For objective Moon 1, to establish the chronology of basin-forming impacts by measuring the radiometric age of samples directly sourced from the impact melt sheet of a pre-Imbrian lunar basin, we took advantage of newly-identified potential sites. Basin interiors are fundamentally different geologic settings than the Apollo sites. Basin formation is an extremely energetic process that melts large volumes of target rock. This process resets isotopic ratios in re-crystallized impact melt minerals, recording the age of basin formation (the impact melt radiometric age is technically the age of impact melt crystallization, which can lag behind basin formation by >100,000 years for thick, convective melt sheets). While some impact melt is ejected during basin formation, the ejected melt is mixed with and diluted by non-melted basin ejecta and the ejecta substrate. Therefore, attempting to identify and characterize impact melt in basin ejecta has resulted in ambiguous interpretations. Conversely, the impact-melt sheet is an in-place relic of basin formation that was unaffected by the chaotic ejecta process. Directly sampling the impact-melt sheet would provide the most reliable record of the basin’s age. In most of the nearside basins, volcanic activity flooded the basins, covering their impact-melt sheets. But in



several locations, younger impact craters punched through this basaltic veneer to expose the original impact melt sheet, as revealed by their geochemical signatures from orbit.

The Crisium basin has a model age of ≥ 3.94 Ga (van der Bogert *et al.*, 2017) and ≤ 4.07 Ga (Orgel *et al.*, 2018) as determined by crater size-frequency distribution measurements but is significantly overprinted with Imbrium secondaries. An *in situ* dating precision of 0.20 Ga (2σ), may not be enough to distinguish the age of Crisium from Imbrium, but an age constraint on Crisium might increase the number of basins known to have formed in a cataclysm, including Crisium and Humboldtianum (which sits stratigraphically between Crisium and Imbrium (Fassett *et al.*, 2012)). A greater number of basins (~ 12) have crater density model ages suggesting that they formed between Nectaris and Imbrium. If the age difference between the Nectaris and Imbrium is negligible, then a greater number of basins had to form in a short time strengthening a cataclysm interpretation. But, if the age difference between Nectaris and Imbrium were measurable, then those twelve basins would have had a longer time window in which to form. As yet, no returned samples have been definitively linked to the Nectaris basin impact-melt sheet; consequently, the Nectaris basin has been interpreted to be as young as 3.85 Ga or as old as 4.17 Ga (Fischer-Gödde and Becker, 2012; James, 1981; Neukum and Ivanov, 1994; Orgel *et al.*, 2018; Stöffler *et al.*, 2006), though the younger interpretation is inconsistent with geological mapping and stratigraphy (Fassett *et al.*, 2012). The differences between the two suggested ages may be resolvable within the precision assumed in this study; if 3.8 ± 0.2 Ga, we would appear to confirm the younger option; if 4.1 ± 0.2 Ga, we would confirm the older. However, on the face of it, a single age determination having a 200 Myr uncertainty may be insufficient to confidently distinguish the age of these early basins from the Apollo sample-derived age of Imbrium. Therefore, the aforementioned strategies of using two independent techniques (**Section 1.4**) on multiple samples (**Section 1.5**) must be more rigorously developed to understand how best to address this objective.

In Crisium, several candidate impact-melt exposures were identified by Spudis and Sliz (2017). In examining these candidate sites, Runyon *et al.* (2020) investigated Yerkes crater (36 km, 14.6° N, 51.7° E) as a promising exposure of the Crisium impact-melt sheet. Yerkes predates the most recent mare flows, but the rim and central peaks of Yerkes have not been fully buried by those flows. The rim and central peak structures exhibit a noritic mineralogical signature, distinguishing Crisium impact melt from the mare basalts (Runyon *et al.*, 2020). Similar compositional patterns are observed at other craters within central Crisium, including Peirce (18.8 km, 18.26° N, 53.35° E) (**Figure B1-5**), Picard (22.3 km, 14.6° N, 54.7° E), Lick (31.6 km, 12.4° N, 52.8° E), and several smaller craters, where noritic impact melt is exposed from beneath the mare fill. For this study, we further characterized Peirce as a potential landing site. Based on crater degradation and embayment relationships apparent in LROC WAC imagery and LOLA topography, Peirce appears to postdate the most recent mare basalt emplacements. The floor of Peirce exhibits a distinctive noritic character in Moon Mineralogy Mapper (M3) mafic abundance and pyroxene composition parameters generated using techniques developed and validated by Moriarty and Pieters (2016); this composition is similar to the rim and central peak of Yerkes, indicating that Peirce also exposed the pre-mare Crisium impact-melt sheet. As in Crisium, the melt sheet of Nectaris has been mostly obscured by post-basin mare resurfacing. However, Rosse crater (11.4 km, 17.9° S, 35.0° E) in central Nectaris appears to have excavated through the mare basalts, exposing noritic impact melt material from the melt sheet (**Figure B1-6**). In Rosse, impact melt material is abundant and mineralogically and spectroscopically distinct from local mare basalts, allowing unambiguous *in situ* identification. While each of these features have exposed the underlying basin impact-melt sheet, landing sites with access to material from crater central peaks may be the best targets for obtaining the age of the basin itself, rather than the reset age of the younger crater (Young *et al.*, 2013). Furthermore, identifying the composition of Nectaris impact melt may make it possible to definitively identify basin-specific impact-melt samples in the Apollo sample collection.

For objective Moon 2, to establish the age of a very young lunar basalt to correlate crater count with crystallization age, we considered two sites: P60 basalt and Le Monnier crater. The P60 basalt unit, located just south of the Aristarchus plateau (approximately 21° N, 40° W), has a CSFD age as young as ~ 1 Ga (Hiesinger *et al.*, 2003; 2011; Stadermann *et al.*, 2018), which makes it the youngest observed extensive mare basalt unit on the lunar surface. The P60 unit is a prime target for geochronology



studies because dating a young lunar surface would help to anchor the young end of the crater size-frequency distribution curve (*e.g.*, Jawin *et al.*, 2019); accordingly, several robotic missions have been proposed to go to this uniquely young basalt (Carson *et al.*, 2016; Draper *et al.*, 2019). We used M3 data to assess the mineralogical diversity of the P60 area using mafic mineral abundance and pyroxene composition (Moriarty III and Pieters, 2016). The P60 mare emplacement exhibits a distinctly basaltic mineralogy based on strong, relatively long-wavelength spectral absorption bands (**Figure B1-7**). Most of the P60 area is relatively flat, has low slopes, and low Terrain Ruggedness Index (TRI) values. However, owing to its young age, the regolith is relatively immature, resulting in areas of higher Diviner-derived rock abundance (DRA) than older mare surfaces. **Figure B1-8** outlines two potential landing areas that have low slopes and low TRI, as well as few measurable boulders.

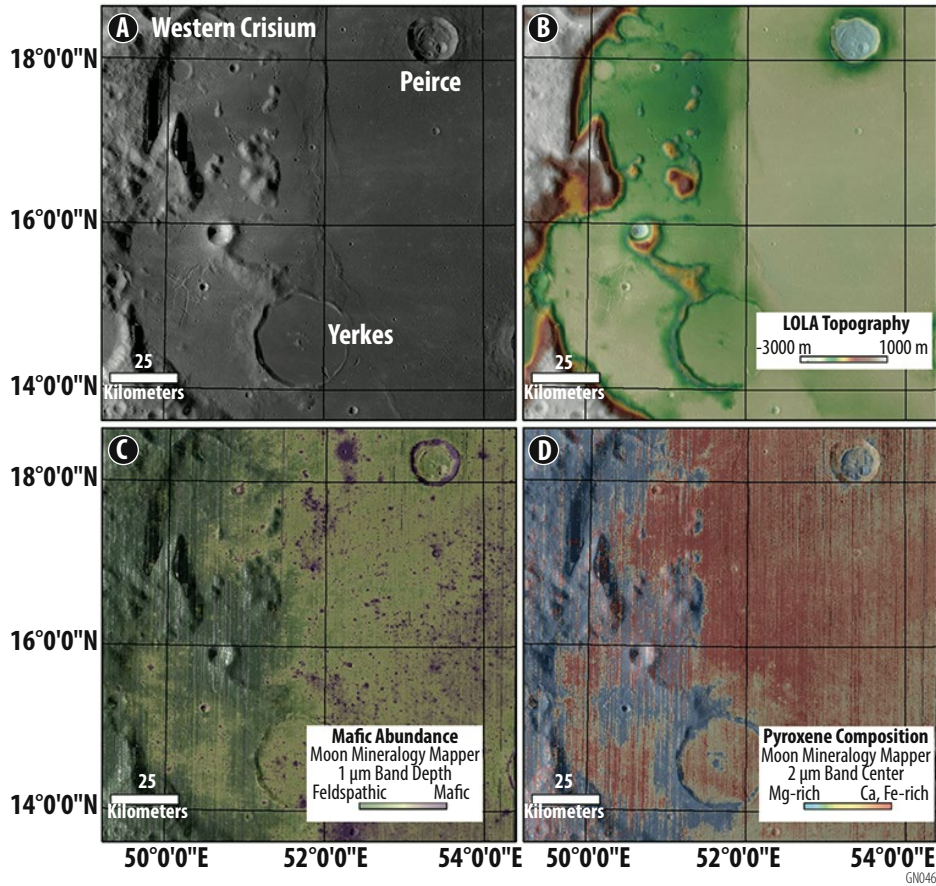


Figure B1-5: Peirce crater geologic and mineralogic context in (A) LROC WAC imagery, (B) LOLA topography, (C) M³ mafic abundance, and (D) M³ pyroxene composition parameters showing that Peirce excavated noritic Crisium impact melt, which is recognizably distinct from local mare basalts, enabling unambiguous discernment for *in situ* analyses.

Le Monnier is a 57-km diameter impact crater on the western rim of Serenitatis basin, at 26.86°N, 30.08° E (**Figure B1-9**). The eastern rim of Le Monnier is absent and the crater is infilled with mare basalt, forming a bay off of Mare Serenitatis. The basalt pond that covers the surface of Le Monnier has a model age of 2.4 Ga, based on crater counts (Hiesinger *et al.*, 2011). The young age of the basalt in Le Monnier makes it a particularly interesting target. Geologic context and mineralogic diversity for the Le Monnier region (**Figure B1-9**) show that the crater floor also has a distinctly basaltic mineralogy, based on strong, relatively long-wavelength spectral absorption bands in M3 data. Landing site assessment shows that there are many possible safe landing ellipses in the smooth, flat interior of Le Monnier, making it an ideal candidate for a landed mission (**Figure B1-10**) and a complement to

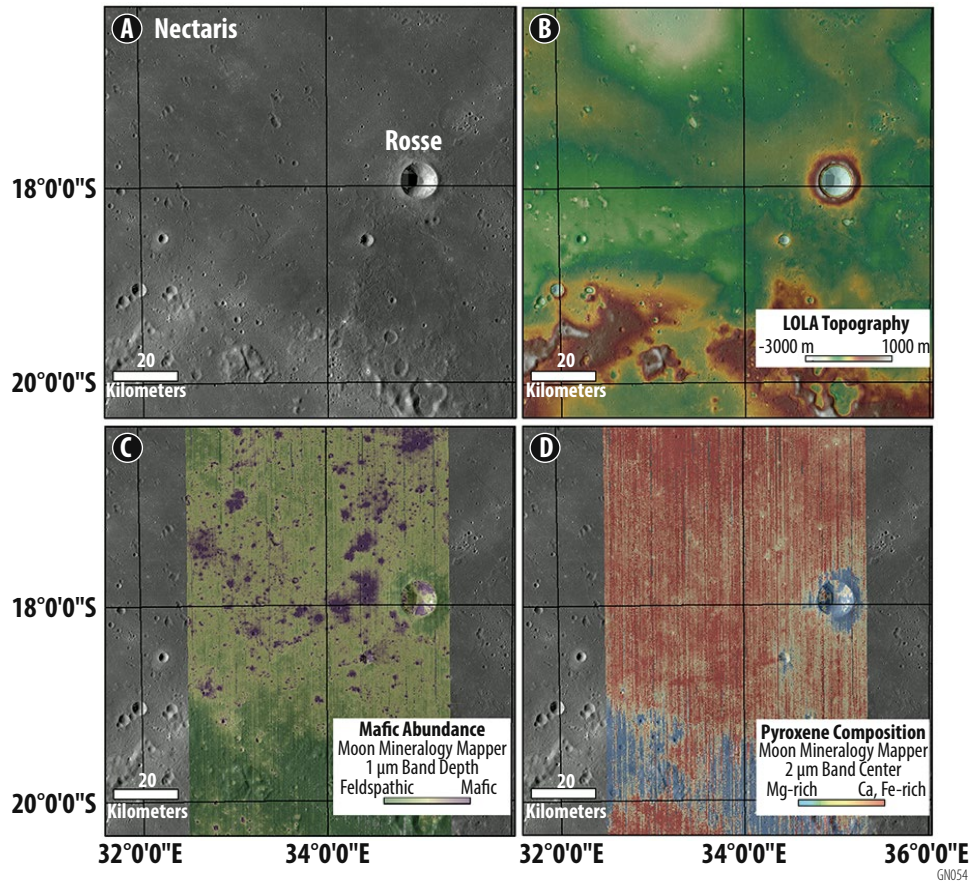


Figure B1-6: Rosse crater geologic and mineralogic context in (A) LROC WAC imagery, (B) LOLA topography, (C) M3 mafic abundance, and (D) M³ pyroxene composition parameters showing that Rosse excavated noritic Nectaris impact melt from beneath the mare-flooded surface of Nectaris.

the P60 basalt or a comparably young basalt, such as the proposed target of Chang'E 5 sample return, northeast of Mons Rümker (Zhao *et al.*, 2017).

Our Mars study objectives are to establish the age of a well-exposed Hesperian martian lava terrain to correlate crater density with crystallization age, and establish the epoch of martian habitability by measuring the radiometric age of Noachian clay-bearing stratigraphies. We initially identified sites for this study that would enable access to both lithologies of interest, taking advantage of the significant engineering and scientific research expended on potential landing sites for previous, current and future landed missions to maximize confidence in accessibility and interpretations. Examples include the broad lava plains of Syrtis Major, including lavas exposed at the Nili Fossae Trough and to the south of the NE Syrtis candidate landing sites for MSL and Mars 2020. The Nili Fossae Trough (**Figure B1-11**) provides access to representative sections of widely distributed units, including Noachian units with clay minerals and Hesperian lavas. The Northeast Syrtis region also provides access to representative sections of widely distributed units including clays, carbonates, sulfates, and lavas (**Figure B1-12**). The extensive characterization studies in this area provide the geologic context with which to interpret geochronology dating (Bramble *et al.*, 2017; Ehlmann and Mustard, 2012; Mustard *et al.*, 2007; Scheller and Ehlmann, 2020).

The addition of mobility to a geochronology mission to either of these sites could enable access to lavas and clay-bearing strata within short distances of the landing site (~5 km for Nili Fossae Trough, ~20-30 km for NE Syrtis), and could enable achieving both Mars 1 and Mars 2 objectives. Both sites would also be suitable for a fixed lander, though a fixed lander would enable access to only one type of terrain and solve only one objective. Additional examples exist across Mars for one or both of

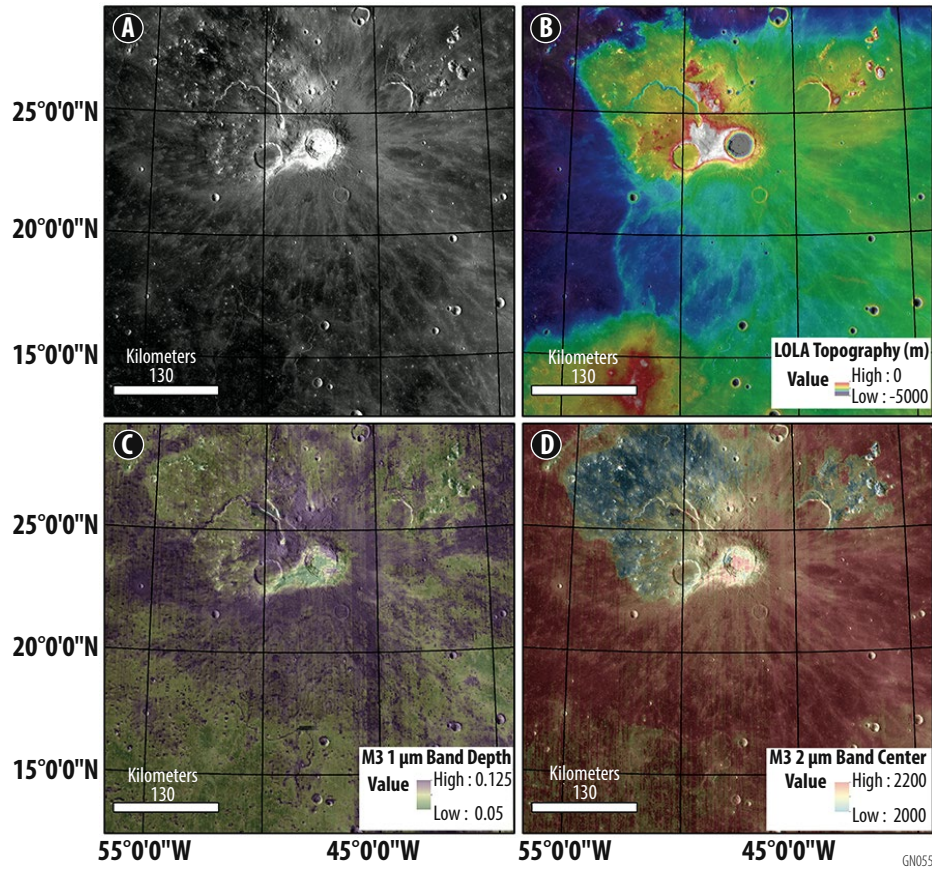


Figure B1-7: Geologic context for the P60 region: (A) LROC WAC imagery, (B) LOLA topography, (C) mafic mineral abundance, and (D) pyroxene composition showing that it exhibits a broad expanse of distinctly basaltic mineralogy, based on strong, relatively long-wavelength spectral absorption bands in M³ data.

these objectives, such as the landing sites considered as candidates for the MSL and Mars 2020 missions (Grant *et al.*, 2011; Grant *et al.*, 2018). For example, other widely exposed lava plains occur (*e.g.*, Hesperia Planum) as candidate landing sites, though these sites would require considerable additional analysis to certify. Mawrth Vallis (**Figure B1-13**) represents a widespread, ancient clay-bearing sequence of rocks that has also been well-characterized for suitable landing (Poulet *et al.*, 2020); other examples include sedimentary/hydrothermal materials with mineralization conducive to age-dating such as the jarosite-sulfate sediments at NE Syrtis Major; (*e.g.*, Quinn and Ehlmann, 2019); jarosite bearing weathering sequences or sediments both inside and outside of Valles Marineris (*e.g.* Milliken and Bish, 2010; Weitz *et al.*, 2015) and jarosite and alunite within clay-bearing sedimentary deposits in Columbus or Cross crater paleolakes (*e.g.*, Ehlmann *et al.*, 2016b; Wray *et al.*, 2011).

Expanding the absolute chronological framework of an asteroid within the precision of *in situ* dating would be most impactful by establishing the radiometric ages of samples with well-established provenance; this constraint limits landing sites to well-studied bodies with specific geologic epochs, such as Vesta. Key stratigraphic craters and contiguous geologic terrains would yield age determinations that constrain the body's geologic timescale. The most prominent impact structures on Vesta, and those that pin vestan stratigraphy, are the Veneneia, Rheasilvia and Marcia craters (**Figure B1-14**). Ideal landing sites would allow sampling of all three key impact structures, as well as some of the youngest impact melt deposits. Here we assume that sampling would be similar to a mature lunar soil, in terms of the number of fragments available and the geologic diversity of the fragments. The best-resolution images of Vesta from the Dawn mission's low altitude mapping orbit (LAMO) are 70 meters per pixel, too coarse to identify hazards at the lander scale, meaning a mapping survey would be needed to identify suitable landing locations.



The first site would be the Rheasilvia central peak. Deep-seated material brought to the surface yields, information about internal structure and composition (*e.g.*, potential mantle material). A flat, high-standing plateau means resurfacing should be minimal, yielding a good location to derive the age of Rheasilvia. Since published ages range from 1-2 Ga to 3.4 ± 0.1 Ga, this is a prime target for *in situ* geochronology, assuming the samples can be tied to Rheasilvia through chemical or other means. The second site is Marcia crater, the youngest large crater on Vesta (Williams *et al.*, 2014a). Dark Veneneia material may be exposed in Marcia, as well as superposed bright Rheasilvia material and Marcia ejecta material. The age of Marcia is not as contentious as the age of Rheasilvia or Veneneia, but the possibility of learning about the composition and age of all three at a single site would mean a well-studied suite of samples could potentially provide as many as three tie-points for calibrating the chronology of Vesta, and by extension the entire middle portion of the main asteroid belt. However, a mission to such a complex site would require analyzing more samples at the site, nominally 10 for each of the three target lithologies.

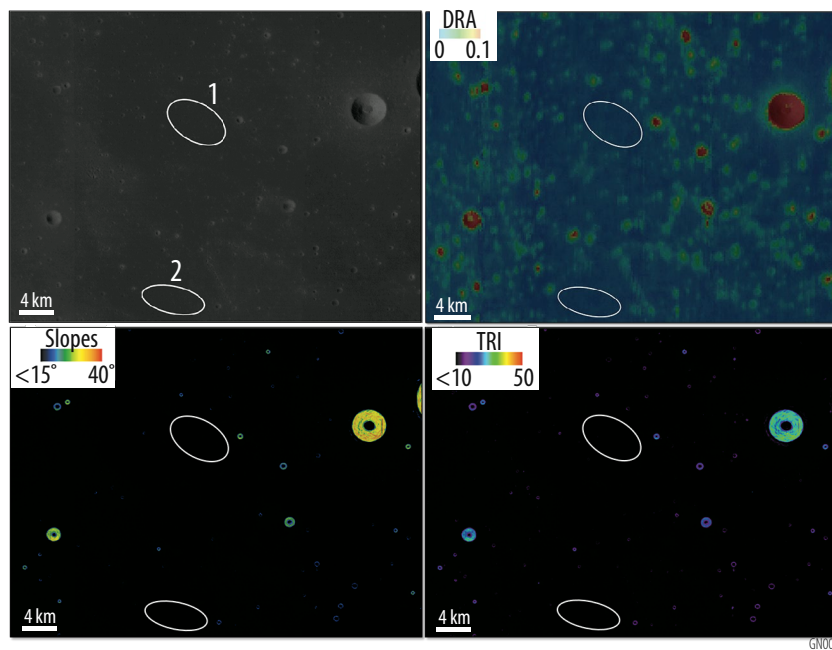


Figure B1-8: Potential landing areas in the P60 region, indicated by ellipses. Ellipse 1 is centered at 21.06°N , -40.43°E , Ellipse 2 is centered at $(20.36^{\circ}\text{N}$, $-40.70^{\circ}\text{E})$. Upper left: WAC mosaic. Upper right: Diviner rock abundance (DRA). Lower left: Slopes, with slopes < 15 deg (i.e., safe slope ranges) shown in black. Lower right: Terrain Ruggedness Index (TRI), with safe values (TRI < 10) shown in black.

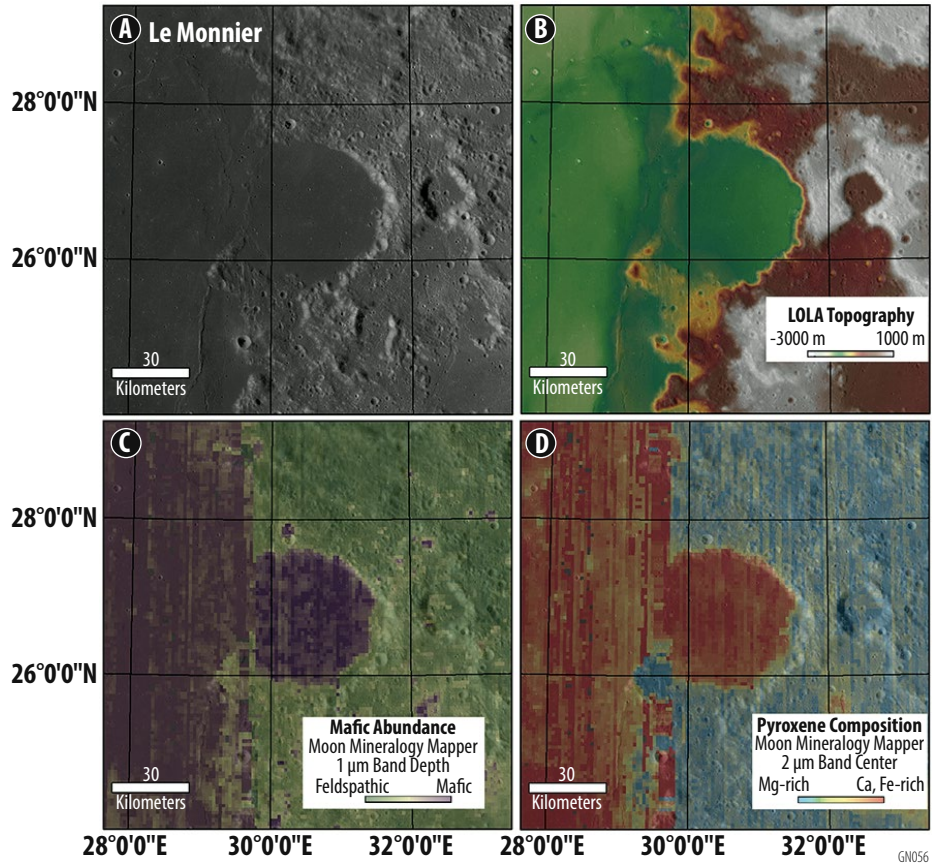


Figure B1-9: Geologic context for the Le Monnier crater region was assessed using (A) LROC WAC imagery and (B) LOLA topography. Mineralogical diversity, including (C) mafic mineral abundance and (D) pyroxene composition, was assessed using Moon Mineralogy Mapper data. The mare floor of Le Monnier exhibits a distinctly basaltic mineralogy, based on strong, relatively long-wavelength spectral absorption bands in M³ data.

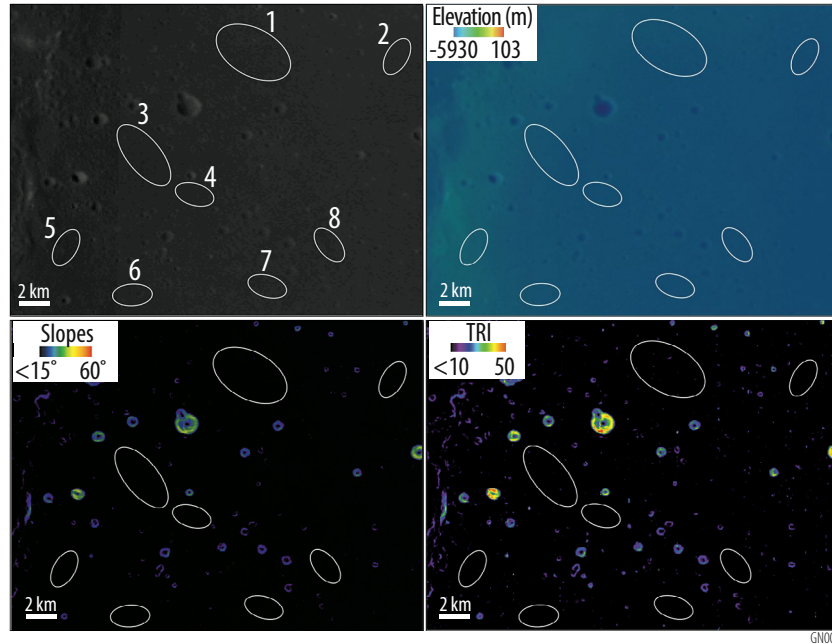


Figure B1-10: Potential landing areas inside Le Monnier crater, indicated by ellipses. Coordinates for ellipses are listed in **Table B1-2**. Upper left: WAC mosaic. Upper right: Diviner rock abundance (DRA). Lower left: Slopes, with slopes < 15 deg (i.e., safe slope ranges) shown in black. Lower right: Terrain Ruggedness Index (TRI), with safe values (TRI < 10) shown in black. Image centered at (26.86°N, 30.08°E).

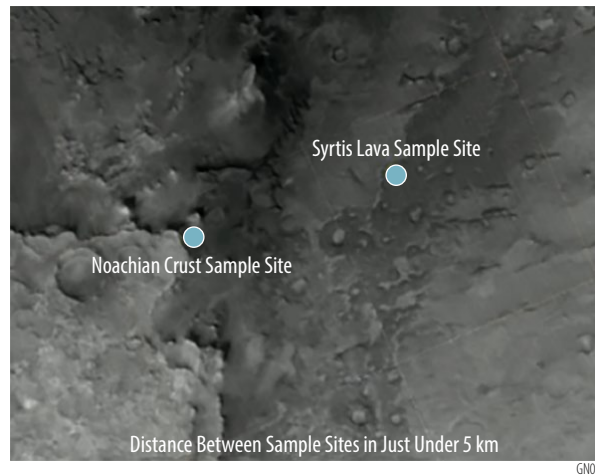


Figure B1-11: CTX image of the floor of Nili Fossae Trough (right two thirds) and Noachian-aged crust (with orbital signatures of low-Ca pyroxene and clay) to the west (left one third), proposed as the landing site for both the MSL Curiosity and Mars 2020 Perseverance missions (e.g., Grant et al., 2010; 2018). The yellow dots are just under 5 km apart and the image is ~15 km across; north is toward the top.

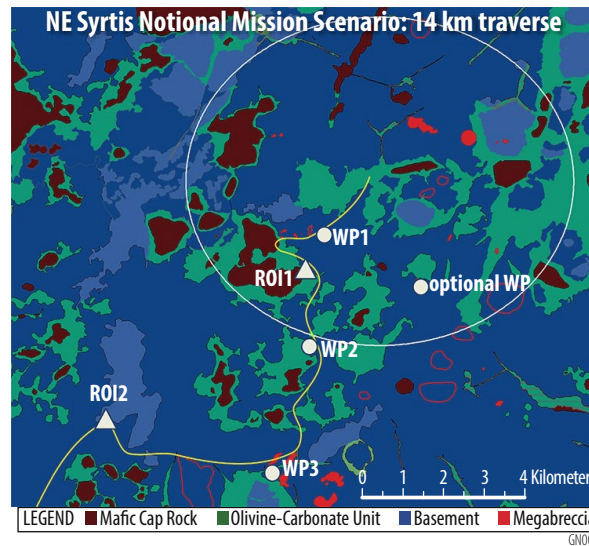


Figure B1-12: Northeast Syrtis Major lithologic map showing exposures of Noachian crust and mafic capping units. Adapted from Bramble et al. (2017) with landing site ellipse for Mars 2020 (12×10 km) and notional traverse to regions of interest (ROI) as shown in Sun et al. (2018).

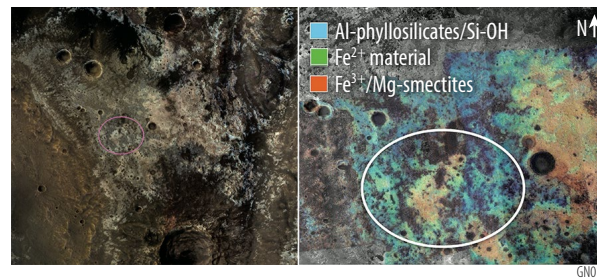


Figure B1-13: Mawrth Vallis landing site showing High-Resolution Stereo Camera color (left) and CRISM-derived mineralogy (Bishop et al., 2008). The ellipse envelopes are drawn for Mars 2020 (12×10 km) as shown by Bishop et al. (2017).

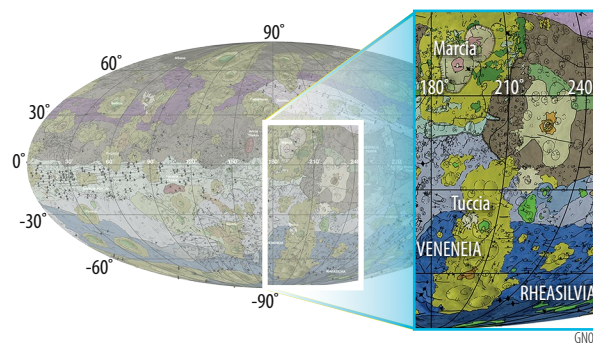


Figure B1-14: Excerpt from the geological map of Vesta derived from Dawn spacecraft data, showing the Rhea Silvia and Veneneia basins (dark blue colors) near the south pole, and Marcia crater (light brown and yellow) near the equator. Map is a Mollweide projection, centered on 180 degrees longitude using the Dawn Claudia coordinate system.



Appendix B2 – Payload

1. OVERVIEW

For this study, measurement requirements for all goals and objectives would be met by carrying a single notional payload comprising representative instruments (**Table 2** in the **Main Report**). All instruments, except the inductively coupled plasma mass spectrometer (ICPMS), will be TRL 6 in 2023 (the start of the next Planetary Decadal), and no additional development costs nor technology maturation would be required before a mission Phase B. Additional technology maturation investments that would be beneficial to this class of missions might include improving the sensitivity of geochronology instruments to improve age measurement precision, development of end-to-end sample acquisition and handling to feed samples to multiple instruments (*e.g.* Curiosity, Europa Lander), and flight system technologies to enable the spacecraft operations to increase science return (*e.g.* peak power, night survival, communications throughput, etc.).

To make significant advances in creating a geochronologic framework, *in situ* geochronology must yield ages that are both precise and accurate – that is, the measurement techniques must yield small uncertainties on the calculated age, and that age must be recognizable and interpretable as a geologic event. Multiple groups have made substantial progress on bringing some of these techniques closer to flight implementation; a comprehensive review of developments and proposals appears in Cohen *et al.* (2019). Armed with this knowledge, the team narrowed consideration to a representative set of instruments based on their precision and potential for implementation. For many planetary materials, it may be possible to measure ages using more than one system, which is common practice in terrestrial laboratory geochronology. Agreement between multiple chronometers increases confidence in the interpretation of the geologic events experienced by the sample, though disagreement does not negate the inherent value of each measurement. The team therefore baselined two independently-developed *in situ* dating instruments that together would access both the Rb-Sr and K-Ar radiometric systems.

Geochronology analyses should be paired with other observations that provide context and further enhance the science return of a prospective mission. The uncertainty in a geochronology measurement would be influenced not only by technological capabilities but also by the complexity (*e.g.*, mineralogy, alteration history, etc.) of the planetary material and geologic setting being investigated. Thus, sample selection, location, and geological context would be just as important as the analytical methodologies that enable radiometric dating. Remote imaging (from visible, or VIS, to mid-infrared, or IR, wavelengths) and trace element compositional measurements (enabled by ICPMS) would be included in the baseline payload so that samples identified for processing would be well-understood and suitable for dating. Verifying that selected samples were associated with cohesive surface units, rather than deposits not definitively representative of the specific locality under investigation, would further enable interpretation of radiometric ages and deduction of relationships to mapped surface features.



1.1 Instrument Definition

Rb-Sr Geochronology

The Chemistry and Dating EXperiment (CDEX) is a Laser Ablation Resonance Ionization Mass Spectrometer (LARIMS) developed via the NASA PIDDP and MatISSE Programs (Anderson *et al.*, 2015a; Anderson *et al.*, 2015b). CDEX uses LA-MS to obtain elemental abundance and LARIMS to obtain isobar-free rubidium-strontium (Rb-Sr) dates (in addition to lead-lead (Pb-Pb) dating in development). Because CDEX uses an isochron approach, scanning the laser beam over the sample to map elemental abundances at microscopic scales, it can provide context with which to interpret isotopic age data, for example by recognizing secondary alteration. CDEX is based on two prototypes and designs proposed for Mars 2020 and Discovery 2015. The first generation CDEX system has been used to demonstrate Rb-Sr and Pb-Pb measurements on terrestrial analogues with precision of ± 50 -180 Myr and ± 40 -80 Myr (Anderson *et al.*, 2015a; Anderson *et al.*, 2015b). CDEX uses laser ablation to vaporize a small sample of the target rock, generating >99.9% neutral atoms. Sr is selectively ionized by using lasers tuned to electronic resonances (461 and 554 nm for Sr) in the neutral atoms, followed by photoionization of the excited atoms with a 1064-nm laser. This process for Sr is followed by a couple of microseconds thereafter by the corresponding process for Rb (using 780 and 776 nm for the resonances) in the same ablation plume. This staggered ionization offsets the arrival of Sr from Rb ions at the detector of a time-of-flight mass spectrometer, eliminating isobaric interferences between Rb and Sr, and ensuring that the atoms come from the same ablation event. For Pb resonance ionization, the ablated plume is illuminated with lasers tuned to the 283.3-nm and 600.2-nm resonances and use the same 1064-nm light for photoionization. CDEX typically measures 100-300 locations on a sample in a raster pattern, ablating 50- μ m diameter laser spots, thus sampling a range of different minerals for Rb-Sr and Pb-Pb isotope ratios. Every fifth spot, CDEX measures a well-characterized standard in the same manner. Spots with an isotope signal-to-noise ratio (SNR) > 2 are kept for the final analysis. When mapped onto a photomicrograph, the magnitude of the $^{87}\text{Rb}/^{86}\text{Sr}$ ratio derived from corrected spectra highlight the different minerals in the sample, commonly matching with elemental abundance maps produced in LA-MS mode. The CDEX RI lasers can be turned off to map elemental chemistry in LA-MS mode, or measure organics in two-step laser mass spectrometry (L2-MS) mode.

Table B2-1: CDEX characteristics.

Type of instrument	LARIMS
Dimensions (cm x cm x cm)	51x51x51
Mass without contingency (kg)	55
Mass with 30% contingency (kg)	71.5
Average power without contingency (W)	140
Average power with 30% contingency (W)	182
Average data rate without contingency (Mbit/sample)*	2240
Average data rate with 30% contingency (Mbit/sample)*	2912
*Prior to 2:1 compression	

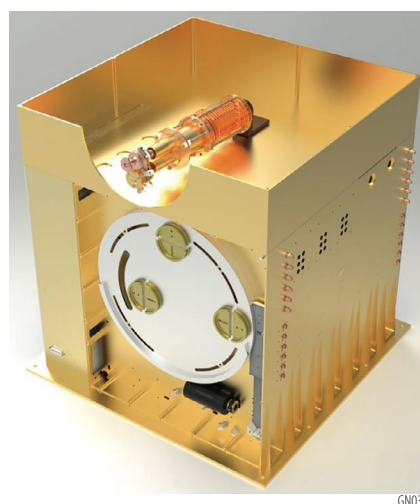


Figure B2-1: Rendering of the CDEX instrument (Southwest Research Institute).



K-Ar Geochronology

Several laboratories have developed breadboards that provide comprehensive compositional analysis, including mineralogical identification, major element chemistry, and K-Ar dating, of solid samples by measuring the parent K via laser induced breakdown spectroscopy (LIBS), and daughter Ar via mass spectrometry (MS) (Cattani *et al.*, 2019; Cho and Cohen, 2018; Cohen *et al.*, 2014; Devismes *et al.*, 2016). Of these prototypes, the KArLE investigation developed through the NASA PIDDP and DALI programs is the most mature; in fact, the core technologies of this instrument have already been demonstrated on the MSL mission (*e.g.*, (Cohen *et al.*, 2019; Conrad *et al.*, 2016; Farley *et al.*, 2014; Le Deit *et al.*, 2016; Sautter *et al.*, 2014). KArLE completely releases Ar from small pits using laser ablation (LA) and admits the released gas to the MS. Using laser ablation enables the technique to be applied to solid, unprepared samples such as chips or pebbles rather than crushed/processed powders, and surface contamination can be ablated away without interfering with the chemical analysis. KArLE also permits multiple laser measurements to be made on a single sample, creating a linear array of measurements with a slope proportional to the age of the rock (an internal isochron). Using multiple measurements to construct an isochron decreases the uncertainty in the inferred age and increases the robustness of the interpretation. The isochron approach also obviates the need to independently assume or determine any initial or trapped contributions to ⁴⁰Ar in a bulk sample. The LIBS-MS family of instruments is promising for near-term implementation because its components (LIBS, MS, and cameras to measure the ablation pit volume) have successfully flown aboard the Curiosity and Rosetta missions. The quantification of elements by LIBS and the volume measurement by optical metrology are relatively imprecise compared with mass spectrometry, leading to estimated uncertainty using this technique of ±8-16% (2σ) in individual mass measurements, with reduced uncertainty in the inferred age potentially achievable using multiple-point isochrons, approaching the guidelines set out in the NASA Technology roadmap. Each element (LIBS, MS, camera) makes measurements beyond geochronology, providing microimaging, complete elemental analysis (including rare metals and volatile elements like H and Cl), and volatile compound mass spectrometry. The same measurements also yield cosmic-ray exposure ages.

Table B2-2: KArLE characteristics.

Type of instrument	LIBS-MS
Dimensions (cm x cm x cm)*	35x55x48
Mass without contingency (kg)**	22.9
Mass with 30% contingency (kg)	30
Average power without contingency (W)	100
Average power with 30% contingency (W)	130
Average data rate without contingency (Mbit/sample)	1061
Average data rate with 30% contingency (Mbit/sample)	1379
*Volume encompasses ICPMS instrument	
**Instrument mass not including the mass spectrometer, which is carried in the ICPMS allocation	

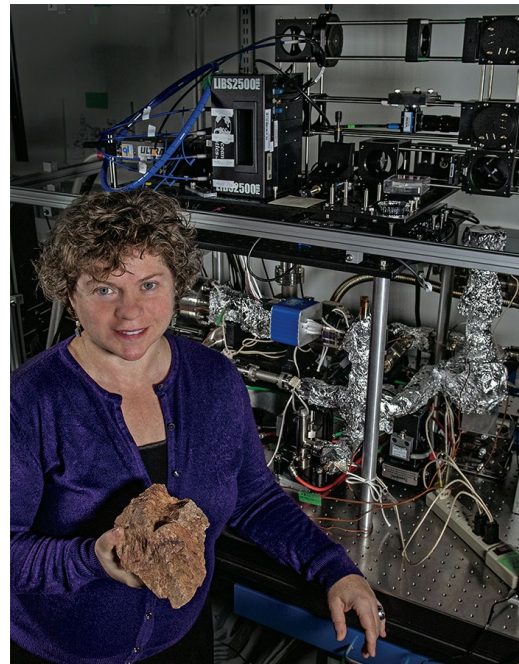


Figure B2-2: KArLE laboratory breadboard (GSFC).



Trace-element Composition

Determining geological context and characterizing associations between sampled rock fragments and specific geologic units observed by remote sensing would rely on establishing compositional and lithologic groupings. Both geochronology instruments, CDEX and KARLE, detect a range of major and minor elements that would assist in associating samples with specific lithologies, but complementary trace element analysis (ppmw levels and below) would enable the ultimate discrimination of putative genetic relationships between different planetary materials. For example, basalt flows with common mineralogies and/or major element characteristics, but derived from distinct source regions, may be distinguished by rare earth element (REE) abundance patterns, redox-sensitive trace element ratios (*e.g.*, V/Sc or Ce/Ce*), or temperature-sensitive partition coefficients (*e.g.*, Ni in olivine). Aqueous alteration could be tracked via the dynamics of fluid-mobile elements (*e.g.*, solubility B > Ca > Ba), and exogenous materials identified by enrichments in siderophile elements (*e.g.*, Mo/Ce) in impact melts. Further, enhanced science return from trace elements could include: determining volatile element depletion (*e.g.*, Na, Zn, and Pb) and/or refractory element enrichment (*e.g.*, Al, Ti, and REE); evaluating distributions of heat-producing elements (K, Th, and U) in silicate minerals; and tracking fluid interactions and chemical weathering via ⁷Li/⁶Li isotopes. In terrestrial laboratories, ICPMS is the benchmark for the quantitative measurement of trace element abundances in solid and/or liquid samples. The adaptation of such technology for spaceflight applications is currently being pursued through the NASA PICASSO Program (Arevalo Jr. *et al.*, 2019); a low-pressure plasma pioneered through the NASA SBIR/STTR Program (Taghioskoui and Zaghoul, 2016) is being interfaced to a quadrupole mass spectrometer originally manufactured as a flight spare for the Sample Analysis at Mars (SAM) investigation onboard the Curiosity rover (Mahaffy *et al.*, 2012). A custom stack of ion optics, including a quad deflector in the image of those flown on the LADEE/NMS and MAVEN/NGIMS instruments (Mahaffy *et al.*, 2015a; Mahaffy *et al.*, 2015b), serves as an interface between the plasma and mass analyzer, separate charged and neutral particles, maximize ion transmission, and relax pumping requirements. A laboratory demonstration of the end-to-end system is currently underway; thus, this technology is on track to be available for a geochronology mission in the next decade. Notably, such instrumentation could provide access to additional geochronometers, such as the U-Th-Pb system, providing corroborative age measurements. The team considered an ICPMS instrument a valuable, though not essential, augmentation to the payload.

Table B2-3: ICPMS characteristics**

Type of instrument	Mass Spectrometer
Dimensions (cm x cm x cm)	Enveloped in KARLE volume
Mass without contingency (kg)	9.5
Mass with 30% contingency (kg)	12.4
Average power without contingency (W)	102
Average power with 30% contingency (W)	132.6
Average data rate without contingency (Mbit/sample)	1.9
Average data rate with 30% contingency (Mbit/sample)	2.5
**Laser ablation system carried in KARLE allocation	



Imaging

Geologic context would provide the framework necessary for interpreting the results of *in situ* geochronology. Visible/color imaging of the ingested samples at hand-lens scale would yield information regarding lithology, grain characteristics (modal proportions, crystal habits, etc.), and petrology (*e.g.*, textural relationships, such as overgrowths versus disequilibria), while millimeter- to centimeter-scale images of the sampling location would provide an understanding of the surface components from which the sample would be acquired. Finally, panoramic imaging of the landing site would reveal the local outcrop features, textures and morphology at mm to m-scale, yielding information about lithology and relationships, and facilitating reconstruction of the local and regional geology of a site. Color imaging, in particular, would capture differences in regolith materials that are expressed through subtle color variations (*e.g.*, orange and black glasses were visible by the Apollo 17 astronauts against the background of surrounding non-pyroclastic regolith). Instruments that acquire images in color at both hand-lens and mm to cm-scale within the environs of the lander are considered essential to the site characterization effort. For this effort, the team included a suite of imagers that are part of Malin Space Science Systems' commercial ECAM product line (Maki *et al.*, 2012; Maki *et al.*, 2003; Maki *et al.*, 2018), though suitable imagers have flown on a variety of planetary missions in diverse environments.

Table B2-4: Imaging systems characteristics.

	Panoramic Imager (each)	Microimager	Postgrind Imager
Type of instrument	Color camera	Color camera	Color camera
Dimensions (cm x cm x cm)	7.8x5.8x4.4	11.7x10.4x21	12x11x11
Mass without contingency (kg)	0.58	1.07	0.25
Mass with 30% contingency (kg)	0.75	1.4	0.33
Average power without contingency (W)	7.4	7.5	7
Average power with 30% contingency (W)	9.62	9.62	9.62
Average data rate without contingency (Mbit per image)*	23.7 (lossless); 11.6 (lossy)	25 (lossless); 12 (lossy)	10 (lossless); 5 (lossy)
Average data rate with 30% contingency*	30.8 (lossless); 15.1 (lossy)	33 (lossless); 15.6 (lossy)	13 (lossless); 6.5 (lossy)
Instrument Fields of View	80 diagonally WFOV	16x12cm	N/A
Pointing requirements (knowledge)	Loose	Loose	N/A
Pointing requirements (control)	N/A	N/A	N/A
Pointing requirements (stability)	0.0037 rad/s	0.0037 rad/s	N/A

*Data rates are postcompression



GN035



GN036

Figure B2-3: Examples of MSSS cameras (left, OSIRIS-REx TAGCAMS, right, MSL MAHLI).



Mineralogy

Infrared (IR) spectroscopy is used to understand the mineralogy of the samples and the surroundings. The most important role of the IR spectrometer would be to identify samples of targeted lithologies, differentiating them from other materials. An IR imaging spectrometer would be particularly well-suited to this task to provide mineralogical composition with spatial context for every pixel in an image. Thus, at landscape-scale, the IR spectrometer would identify and map at centimeter-scale discrete lithologic units in order to relate them to mapped lithologic units and crater densities of lithological units determined from orbital remote sensing. At pebble/cobble scale in the triage station, the IR spectrometer would resolve candidate samples at millimeter-scale, allowing discrimination of samples by petrologic type. Infrared spectral data would be used to determine the diversity of lithologies present at the landing site and differentiate target lithologies for further measurement. Shortwave visible infrared imaging spectroscopy (SWIR; 0.6-3.6 μm) is most appropriate for this mission concept study because Mars dust obscures the rock in visible and near-infrared (VNIR) wavelengths, providing less compositional information (*e.g.*, (Murchie *et al.*, 2019)), and VNIR signatures on the Moon are modified by the effects of nanophase Fe0 particles that are produced by space weathering (Pieters and Noble, 2016). While space weathering on the Moon can be a rough proxy for age, these data would be assessed via the payload camera. SWIR data from the IR imaging spectrometer would be used to identify different lithologies by mapping electronic and vibrational absorptions in reflected light that are related to mineralogy: olivine, pyroxene, ferric iron oxides, Fe plagioclase, and aqueous alteration minerals including phyllosilicates, opaline silica, sulfates, carbonates, and other hydrated salts. Thermal infrared data would be extremely powerful for this purpose as well (*e.g.*, (Christensen *et al.*, 2001)); however, data available from orbit have spatial and spectral resolution insufficient to determine individual lithologies on Mars, the Moon, and Vesta. Several high TRL, low mass, high capability systems for SWIR imaging and point spectroscopy have been developed (Cook and *et al.*, 2016; Ehlmann and *et al.*, 2019; Pilorget and Bibring, 2013; Van Gorp and *et al.*, 2014). The team chose for this study UCIS, an instrument that has substantial heritage from the Moon Mineralogy Mapper imaging spectrometer, but was further matured to TRL 6 for Mars and Vesta under MatISSE (Van Gorp and *et al.*, 2014), and is now being adapted to TRL 6 for the Moon's challenging thermal environment through the DALI Program (Fraeman *et al.*, 2020).

Table B2-5: UCIS characteristics.

Type of instrument	Infrared Imaging Spectrometer
Number of channels	300
Dimensions (cm x cm x cm)	10x20x24
Mass without contingency (kg)	5
Mass with 30% contingency (kg)	6.5
Average power without contingency (W)	30.0
Average power with 30% contingency (W)	39.0
Average data rate without contingency (Mbit/sec)	700
Average data rate with 30% contingency (Mbit/sec)	910
Field of View	FOV: 30deg x 30deg IFOV: <1.5mrad
Pointing requirements (knowledge)	N/A (within degrees of target)
Pointing requirements (control)	N/A
Pointing requirements (stability)	0.28 mrad jitter over 50ms

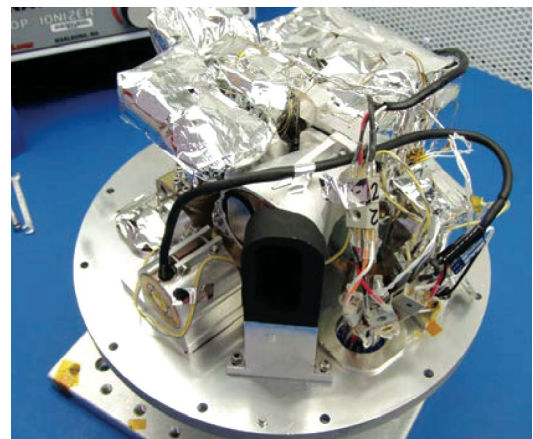


Figure B2-4: JPL UCIS instrument.



Sample Acquisition and Manipulation

At present, geochronology measurements are not standoff or remote techniques; all share a common need for sample acquisition, manipulation, and analysis in a sealed and evacuated chamber to prevent neutral particles and ions liberated from the sample from escaping, and to enable quantitative measurements of parent and daughter isotopes and abundances. Therefore, a sample acquisition and sample handling system would be a required payload element. For this study, tens of individual samples would need to be acquired and dated for each science objective to achieve statistical confidence in the results.

Sample manipulation of rocks using an arm or carousel is at TRL 9, having been used successfully on multiple missions such as the Sample Analysis at Mars (SAM) instrument on Curiosity (Mahaffy *et al.*, 2012), and may be expected to be reasonably adaptable to other bodies and missions with only minor engineering modification. There are several methods that could acquire suitable rocks from various planetary surfaces, depending on the characteristics of the surface. For Mars, drilling capabilities have been extensively developed and will fly on the Mars 2020 rover (as well as the ExoMars rover in 2022); core collection and insertion into a chamber has been laboratory tested (Zacny *et al.*, 2014b). For surface and near subsurface regolith, scoops and sieves with robotic arms have been used on missions such as Apollo and Phoenix (Arvidson *et al.*, 2009). A robotic arm to collect and sieve regolith could provide access to a wider workspace around the lander, potentially mitigating circumstances such as landing in an area with very fine regolith or small-scale heterogeneity.

Alternatively, pneumatic-type systems are being developed that can loft and sort regolith into rocks and fines. A pneumatic system, such as Honeybee Robotics’ PlanetVac (Zacny *et al.*, 2014a), would be mounted on the lander footpads and capture regolith directly underneath the spacecraft. Pneumatic sample delivery is currently at TRL 5-6 maturity, having been tested on an actual lander (Masten) and in vacuum chambers; such a system is also slated to launch on the JAXA Mars Moons eXplorer (MMX) mission. For this mission study, we selected PlanetVac as a baseline system, though any of the others could be considered with appropriate modifications to the concept of operations.

PlanetVac comprises sampling cones, pneumatic nozzles inside the cone, compressed gas tanks, and pneumatic sample transfer lines. Pneumatics released from the nozzle would be directed at the surface, exciting the regolith and directing material through pneumatic plumbing. Samples would be transferred by the pressure differential caused by the released compressed gas and the environmental vacuum at the transfer lines’ exhaust. Sieves in line with the cone and transfer lines would restrict the size of particles allowed to enter the transfer lines, preventing clogging and only allowing through rocks within the desired sampling size range. The samples of desired size would exit the PlanetVac system into a triage station, where they would be examined by onboard instruments, prioritized, and moved to individual instrument for analysis.

Table B2-6: Sample handling system characteristics.

	PlanetVac (Each)	Triage Station	Sample Manipulation Arm	Grinding Station
Component type	Mechanism	Mechanism	Mechanism	Mechanism
Dimensions (cm x cm x cm)	15x26x15	35x25.3x38	30x13x38	27.4x16x11
Mass without contingency (kg)	8	2.5	10	5.7
Mass with 30% contingency (kg)	10.4	3.3	13	7.4
Average power without contingency (W)	16.0	6.0	20.0	20.0
Average power with 30% contingency (W)	20.8	7.8	26.0	26.0
Average data rate without contingency	10 Mbit/Actuation	10 Mbit/Actuation	10 Mbit/Actuation	10 Mbit/Actuation
Average data rate with 30% contingency	13 Mbit/actuation	13 Mbit/actuation	13 Mbit/actuation	13 Mbit/actuation

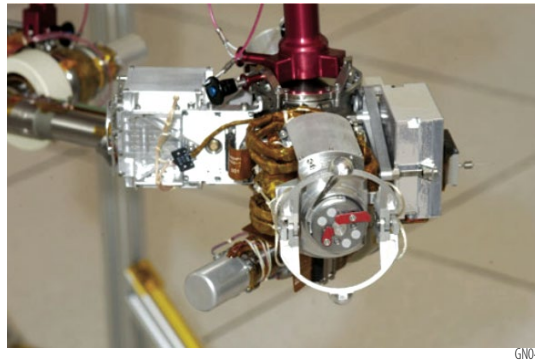
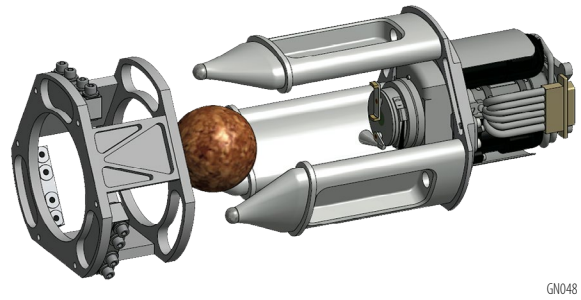


Figure B2-5: Sample acquisition and handling hardware from Honeybee Robotics (left) PlanetVac foot unit, (right) sample manipulation arm, (bottom) MER RAT.

1.2 Payload Concept of Operations

The number of samples that would need to be collected and analyzed is a function of three things: a) how many aliquots of the lithology of interest are needed to ensure statistical confidence in assigning an age to the lithology; b) how much of the lithology of interest makes up the regolith at the landing site; and c) how many rocks of correct size (0.5 – 2 cm in diameter) exist in the regolith. For this study, we adopted a requirement to analyze 10 samples of each lithology of interest to achieve robust counting statistics. The team selected candidate landing sites where current understanding of remote sensing and geologic setting make it probable that the majority of the samples retrieved would represent the lithology of interest, but adopt a further factor to account for potential mixing, thus requiring 30 samples to be collected and triaged per lithology of interest. Finally, we derived the abundance of appropriately-sized rocks to determine the number of samples that would need to be collected and examined in triage. The estimated excavation volume on all bodies would be a few liters or less, a volume easily accommodated by PlanetVac. See **Appendix B1** for more details on sampling statistics and landing sites.

We developed a reference sample analysis process where the samples would be acquired, analyzed, prioritized, and sequentially introduced to each of the Geochronology instruments (**Figure 7** in the **Main Report**). This reference sequence would be repeated for each sample until the required number of samples were completed at each site. All times given are CBE plus 100% margin. The sequence may be paused at multiple points for additional data analysis, troubleshooting, or power reasons. Adaptation of the sequence for each destination is described in **Appendix B3**.

For all mission concepts, the first several days post landing would be dedicated to lander and instrument functional checkout. A limited set of images taken by the panoramic cameras would be down-linked to Earth to verify landing went as intended. With lander systems verified, science operations can



commence. The stereo imagers and IR spectrometer begin to observe the regolith around the lander footpads to provide sample context at the landing site.

PlanetVac would pneumatically gather surface samples and, using a dual sieve system, filter samples to the 0.5-2 cm diameter required for analysis. These samples would be gravity fed into the triage station for identification and prioritization using data from the UCIS spectrometer and Microimager. Sample collection and delivery to the triage station would take 0.4 hours, based on the expected abundance of rocks in the regolith (see **Appendix B1** for rock abundance analysis). The operational time for characterization and prioritization would depend on the process used – onboard algorithm matching using preselected characteristics (2 hrs) or requiring scientific ground-in-the-loop characterization (8 hrs). For this study, we enveloped the time by assuming ground-in-the-loop. After the initial triage data were analyzed, prioritized samples would be selected for further analysis.

The Sample Manipulation Arm (SMA) would use pincers to obtain the prioritized sample from the triage station. The SMA would move the sample to interface with the other instruments. CDEX requires that the rock sample present a flat, polished surface for analysis, so the SMA would first present a sample to a grinding station. At the grinding station, the rock would be ground millimeters of depth into the sample and polished to a 10-micron finish using a heritage design Rock Abrasion Tool (RAT), previously flown on Mars Exploration Rovers (MER). One significant difference from MER is that the RAT would not have to place and align with a large surface rock. Instead, the RAT would have alignment features that would be used to position and dock with the SMA, forming a ridged connection to transfer the grinding force. Load sensors would be used to identify loss of grip on the sample during the grinding operation.

After grinding, the SMA would deliver the rock with the polished surface to the CDEX aperture. CDEX would perform its analysis by rastering the flat, finished surface of the sample over the instrument entrance aperture. The rastering mechanism would be integrated into the CDEX instrument. Typically, CDEX would measure 100-300 locations on a sample in a raster pattern, ablating 5- μm diameter laser spots, thus sampling a range of different minerals for Rb-Sr isotope ratio measurements. The ionization lasers could be turned off to map elemental chemistry. The CDEX analysis time would be 4 hours.

Upon completion of CDEX analysis, the SMA would drop the sample into the KArLE/ICPMS carousel inlet. KArLE and ICPMS share a laser ablation unit, a mass spectrometer, and an internal sample-handling carousel, which is based on the Sample Analysis at Mars (SAM) sample carousel on the Mars Science Laboratory (MSL) mission. Neither KArLE nor ICPMS require samples to have a flat, polished surface, but can accept either a natural sample or a polished sample. Therefore, if the grinding or imaging station fail, KArLE and ICPMS could still analyze the sample. However, samples could not be retrieved from the KArLE carousel after analysis, so this step occurs last in the operations. The sample would be dropped into an individual cup in the carousel; the carousel would rotate the sample cup to the analysis station and elevate the cup to form a seal. The sample would be laser ablated to measure elemental chemistry (including parent K) using Laser-Induced Breakdown Spectroscopy (LIBS). The material liberated by laser ablation would be let into a mass spectrometer either by static expansion and electron impact ionization (neutral species including Ar for KArLE analysis) or via a plasma torch (ionized species including trace elements for ICPMS). KArLE analysis of 6-10 individual locations on each rock sample, including calibration and standard analysis, would take 12 hours. The ICPMS would take an additional 3 hours to analyze several additional locations on each sample using the same laser ablation system and mass spectrometer as KArLE.

While KArLE and ICPMS analyze the rock sample, the SMA could return to the triage station for the next rock sample. After collection and triage, the total sample analysis cycle for one rock sample would be performed within 24 hours. This cycle would be repeated 20 times at the Mars and lunar sites and 10 times at each of the Vesta landing sites. The triage process could be repeated multiple times in the surface operations timeline to obtain a fresh set of samples.

In parallel with sample science, the Panoramic Imagers and UCIS spectrometer would obtain 360-degree coverage of the landing area from lander to horizon. They would be mast mounted on a



rotation/tilt mechanism. Because of lighting constraints, the collection cadence of the context images would be specific to each destination and described in **Appendix B3**.

A total of 20 samples would be analyzed in all concepts, so the data generated by the geochronology instruments would be the same for all destinations. On Vesta, where there would be two science sites, two context imaging datasets would be acquired and there would be additional triage processes planned. Data summaries for the Moon, Vesta and Mars concepts are shown in **Table 2** in the **Main Report**.

1.3 Payload Technology Maturation Plan

CDEX, KArLE, and UCIS are currently funded in NASA instrument maturation programs intended to achieve TRL 6 (System/sub-system model or prototype demonstration in an operational environment). These programs will be completed by 2023, the start date of the next decadal survey. Under the current funding, each of these instruments will have built a high fidelity system/component prototype and operated the prototype in a representative spaceflight environment. They will therefore be ready for infusion into a mission with no additional technology investment needed in Pre-Phase A or Phase A. However, these instruments would require mission-level investment to build a flight version that meets the requirements of the specific mission, including any unique environment and payload integration needs.

The Chemistry and Dating EXperiment (CDEX) is being developed via the NASA PIDDP and MatISSE Programs (Anderson *et al.*, 2015a; Anderson *et al.*, 2015b). CDEX is based on two prototypes and designs proposed for Mars 2020 and Discovery 2015. The KArLE investigation is being developed through the NASA PIDDP and DALI programs (Cho and Cohen, 2018; Cohen *et al.*, 2014). The core technologies of this instrument have been demonstrated on the MSL mission (*e.g.*, Cohen *et al.*, 2019; Conrad *et al.*, 2016; Farley *et al.*, 2014; Le Deit *et al.*, 2016; Sautter *et al.*, 2014). KArLE is based on a prototype proposed for Mars 2020 and currently being developed under DALI. UCIS has substantial heritage from the Moon Mineralogy Mapper imaging spectrometer, further matured to TRL 6 for Mars and Vesta under MatISSE (Van Gorp and *et al.*, 2014), and adapted to TRL 6 for the Moon's challenging thermal environment through the DALI Program (Fraeman *et al.*, 2020).

The adaptation of ICPMS technology for spaceflight applications is currently being pursued through the NASA PICASSO Program (Arevalo Jr. *et al.*, 2019); a low-pressure plasma pioneered through the NASA SBIR/STTR Program (Taghioskoui and Zaghoul, 2016) is being interfaced to a quadrupole mass spectrometer originally manufactured as a flight spare for the Sample Analysis at Mars (SAM) investigation onboard the Curiosity rover (Mahaffy *et al.*, 2012). Under these current investments, ICPMS will achieve TRL 4 by 2023, building a low fidelity system/component breadboard to demonstrate basic functionality and performance predictions. Further maturation to TRL would be required by mission PDR. This could be accomplished by a follow-on MatISSE or DALI investment to mature the ICPMS independent of a flight mission, or a mission investment to mature the instrument. If the ICPMS were to fail to achieve TRL 6 prior to mission PDR, it could be descoped at that time with a moderate loss to science, bearing in mind that major-and minor-element analysis would still be conducted by the other instruments in the payload.

Imagers in this study are part of Malin Space Science Systems' commercial ECAM product line (Maki *et al.*, 2012; Maki *et al.*, 2003; Maki *et al.*, 2018), though suitable imagers have flown on a variety of planetary missions in diverse environments, including Mars (MAHLI, WATSON, ECAMs, Mastcam, and Pancam) and asteroids (ECAMs on OSIRIS-REx). The Heimdall investigation will use four of these imagers on a CLPS mission to the Moon in 2022. Therefore, all considered imagers will be TRL 9 and available for any mission in the next decade.

Sample manipulation of rocks using an arm or carousel is at TRL 9, having been used successfully on multiple missions such as the Sample Analysis at Mars (SAM) instrument on Curiosity (Mahaffy *et al.*, 2012), and may be expected to be reasonably adaptable to other bodies and missions with only minor engineering modification. Honeybee Robotics' PlanetVac (Zacny *et al.*, 2014a) system will be at TRL 6 maturity for Mars, having been tested in vacuum chambers; but a PlanetVac system is slated to



PMCS: Geochronology for the Next Decade

fly on the JAXA Mars Moons eXplorer (MMX) mission in 2024 and on a CLPS lunar lander in 2022, so it will have been fully developed for flight for these destinations.



Appendix B3 – Design Team Study Report

1.1 Introduction

All versions of the Geochronology mission would use a single lander. GSFC developed a lunar lander in detail and performed parametric deltas to develop a lander for Vesta. The Mars lander was designed by Lockheed Martin. The study assumptions were for a Class B, PI-led mission, consistent with a New Frontiers Announcement of Opportunity (AO). The scientific payload was selected to provide complementary, robust science with technologies that would be ready for implementation in a New Frontiers timeframe. Mission requirements for all Geochronology mission studies are provided in **Table 3** in the **Main Report**. Some specific trades in the functional requirements that crosscut all missions are discussed below.

Visit Multiple Destinations: The need for in situ analysis necessitated a lander design. The team investigated whether the lander could hop to at least one additional site after the initial landing to take science samples in data from multiple locations in each destination. The goal to stay within an anticipated New Frontiers cost cap would preclude hopping or roving to multiple scientifically-interesting destinations on the Moon and Mars (**Appendix C** provides mobility trade details).

Power and Mission Lifetime: Based on the surface concept of operations (see **Appendix B2**), the requirement to complete 20 samples would take longer than one lunar, Vestan, or Martian day. Therefore, the lander would need to operate for multiple days and survive multiple nights in all locations. The team enveloped this derived requirement with a surface mission lifetime of one terrestrial year on the Moon and Vesta and 450 sols on Mars to provide margin, ease operations, enable data downlink, and provide potential opportunities for additional landed science. A surface mission lifetime of a least a year would require heat and power to survive night periods, provided by either a large battery or another power source such as a next-generation radioisotope thermoelectric generator (NGRTG). For missions to the inner planets (Moon, Mars, and Vesta), solar power would be sufficient to accomplish the mission, so the team baselined solar arrays and batteries rather than NGRTG. Night power use would drive the mass of the batteries. To minimize nighttime power usage, the instruments would be placed in a low power mode (<16 W). The lander C&DH subsystem would be designed to have minimal functionality at night and to throttle the processor. Communications would be restricted to daylight, although the receiver would be left on at night.

Land Safely: The team designed a lander with enough clearance between its lower deck and the surface to accommodate 0.5 m rocks, which is currently the best resolution imaging available for the Moon. To land safely, the Moon and Vesta landers would use a combination of Terrain Relative Navigation (TRN) and active Hazard Avoidance (HA). TRN would be used to estimate the lander local relative position by comparing terrain maps in memory with terrain measurements from navigation sensors (lidar, optical camera, altimeter). The HA would assess the hazards in the projected landing site and prompt the ACS to take action. Assessment would be based on pre-defined obstacle features that should be avoided, such as rocks of a certain size or slopes of a certain value. The image/measurement used to determine whether these features were within the landing site would be obtained from the TRN images. If a hazard were identified, the HA would take the appropriate action based on the current state and pre-defined decision path to place the lander on a descent trajectory. The TRN and HA systems are detailed in **Section 1.2.4.4**.

Table B3-1 summarizes additional key trades that were performed and their results. Trades at the subsystem level are found in the following sections.



Table B3-1: Geochronology mission key trades.

Trade	Options	Results
Mobility	<ul style="list-style-type: none"> • Hopping • Rover • None 	<ul style="list-style-type: none"> • Hopping feasible on Vesta but, hopping drove propulsion system to be large and costly on the Moon • Rover-based mobility out of cost cap for Mars • Increased the number of samples to be studied at a single site to compensate for loss of mobility
Launch Vehicle	<ul style="list-style-type: none"> • Falcon Heavy Recovery 7,049 kg • Atlas 551 6,330 kg • Delta IV Heavy 10,566 kg • ULA Future Vulcan w/Centaur 8,299 kg 	<ul style="list-style-type: none"> • All launch vehicles considered have the same diameter but different lengths, with Falcon Heavy being the shortest • Moon launch requirement 5,333.7 kg • Vesta launch requirement 6,804.9 kg • Both the Atlas 551 and Falcon Heavy Recovery would be viable options • Due to expected availability issues with the Atlas 551, the team selected the Falcon Heavy Recovery
Descent Propulsion	<ul style="list-style-type: none"> • Chemical • Solid • Mix 	<ul style="list-style-type: none"> • Chemical would be lowest cost and best attitude control and landing velocity • Solid would be required if chemical needs large burn times to reduce finite burn losses, but selected chemical design would not have a finite burn time issue • A mix of propulsion types would add complexity and cost. Most efficient if hopping.
Surface Power	<ul style="list-style-type: none"> • Fuel cells • NGRTG • Solar with batteries 	<ul style="list-style-type: none"> • Fuel cells cannot survive the lunar day and night cycle for the mission duration • NGRTG would add costs, regulatory and thermal issues • Solar arrays with batteries were selected for all missions
Land Safely	<ul style="list-style-type: none"> • Probabilistic approach • Terrain Relative Navigation • Terrain Relative Navigation with Hazard Avoidance 	<ul style="list-style-type: none"> • Use knowledge of landing site and landing ellipse to define site with low risk • Use pre-existing maps of landing area to identify hazards and define flight path • Adds ability to use ACS thrusters to avoid hazards during descent on defined flight path

1.2 Lunar Geochronology Lander

1.2.1 Overview

The lunar Geochronology flight system (**Figure 11** in the **Main Report**) would consist of a lander (4.6 m tall, 3.9 m long, 3.3 m wide) that would easily fit within the Falcon 9 Recovery fairing. The lander would use four main engines with a thrust of 4 kN each and 12 ACS thrusters (two sets of six pairs, one set for primary and one for redundancy). Its three solar arrays (totaling 12 m² total area) to provide a daylight peak power of 928 W BOL, 785 W EOL at lunar noon. An 1,176 AH battery (packaged as four separate batteries) would support night loads. Communications and science operations would be restricted to lunar daylight, although the receiver would be left on during the lunar night. The thermal design would use louvers to keep the lander cool during the lunar daytime and warm during the lunar night. To reduce the distance the samples must travel, CDEX, KArLE, and the sample handling system would be located on a shelf on one side of the lander, as close as possible to the lunar surface.

Table 6 and **7** in the **Main Report** summarize the Geochronology lunar lander characteristics.

1.2.2 Mission Design

The target lunar landing site was near Copernicus crater on the lunar nearside (10°N, -21.5°E). The spacecraft propulsion system would consist of four Aerojet Rocketdyne R-40B engines that use liquid propellant and provide 4000 N of thrust with a specific impulse (I_{sp}) of 293 s. The lander would have a total current best estimate (CBE) wet mass of 4,986.0 kg and total maximum expected value (MEV) wet mass of 5,236.3 kg. **Table 8** in the **Main Report** shows the lunar mission design summary on a Falcon 9 Heavy Recovery. There would be two launch opportunities per day for a minimum energy direct transfer to the Moon: a short coast and a long coast during the 3 day launch window that occurs every two weeks. The two solutions achieve the lunar transfer in two different orbit planes and differ in launch time as well as coast time. Additional constraints (*e.g.*, total eclipse time during the transfer phase) lead the team to choose a direct transfer to achieve a polar orbit.

Flight operations would consist of three phases: launch and lunar transfer, 250 km-altitude circular lunar orbit, and landing. A trade study performed in this mission scenario showed that a direct landing trajectory would be less efficient in terms of propellant (**Figure B3-1**). The orbit that the spacecraft



would initially achieve would not guarantee passing over the desired longitude for landing. To wait for the proper orbit alignment, the spacecraft would remain in orbit until the selected landing site comes into the correct orbital alignment. This could take as long as 30 days. This strategy, as opposed to attempting a direct landing, would not require extra propellant to modify the arrival vector in order to target the landing site. This would be achieved by placing the spacecraft in orbit and landing on the first available opportunity, in which the landing site would be in place (Figure B3-2 and B3-3). Shortly after the orbit condition were achieved, the vehicle would proceed to the landing phase (Figure B3-3).

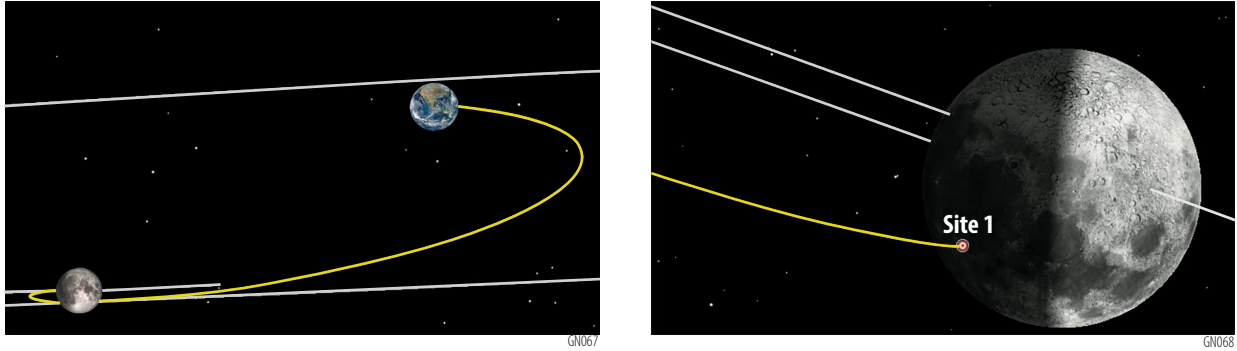


Figure B3-1: Moon-centric view of lunar transfer trajectory (left) and landing trajectories (right) for the direct landing.

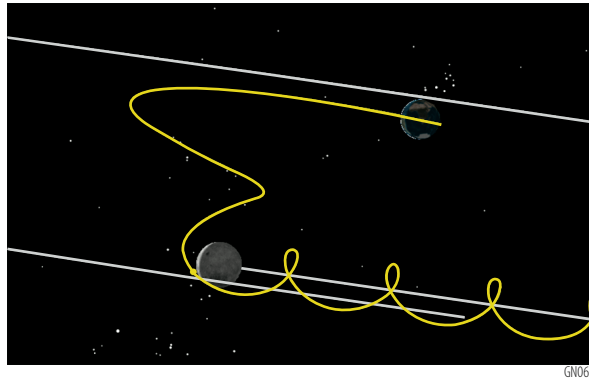


Figure B3-2: Earth-centric view of Moon transfer trajectory.

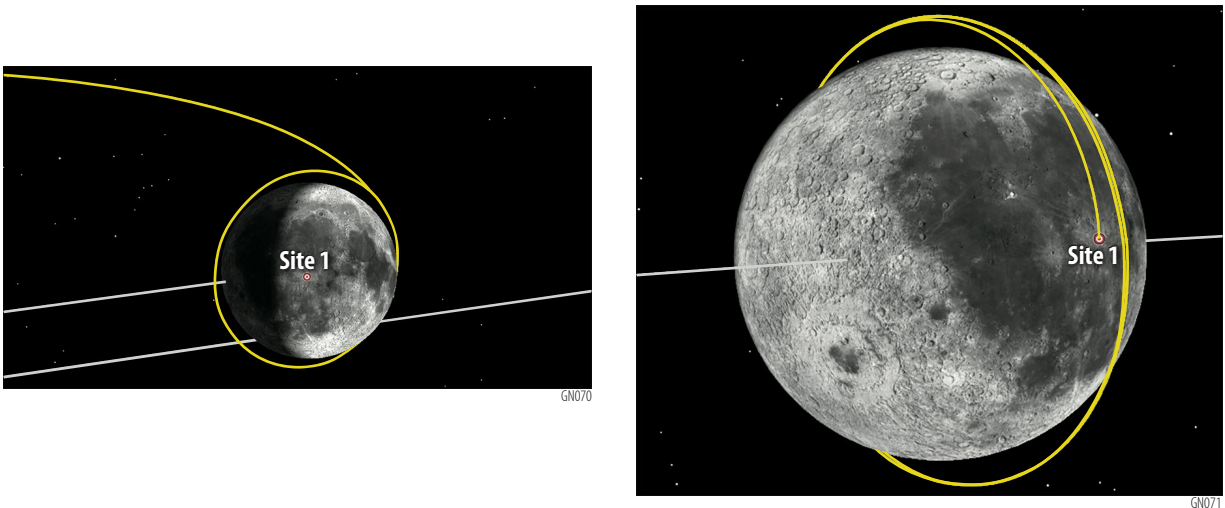


Figure B3-3: Moon-centric view of lunar transfer trajectory (left) and landing trajectories (right) for landing from orbit



The trade between direct insertion and orbit-first options (**Table B3-2**) included propellant margin and derating of the 293s I_{sp} to 290 in the calculations. The difference between the landing masses and the MEV values indicates there may be room for additional mass. Increasing the mass, however, might affect other systems not considered in this study. Notably, the MEV landing mass value of 1,921.3 kg for the orbit-first concept lies within the range of past lunar missions.

Table B3-2: Lunar landing trade: direct vs. orbit staging.

	Direct	Orbit		
Liquid Engine	4x4kN, 293s	4x4kN, 293s		
Launch Mass	5,924.0 kg (fuel: 4,002.8 kg)	5,236.3 kg (fuel: 3,315.0 kg)		
Liquid			LOI	Land
	ΔV	3020.5m/s	774.4m/s	1906.6m/s
	Fuel	4,002.8 kg	3,315.0 kg	
	Burn time	724.7s	357s	1724s
Landing Mass	1,921.3 kg	1,921.3 kg		

1.2.3 Mission Operations

1.2.3.1 Launch and Landing

The Geochronology mission would launch from Cape Canaveral, Florida on a single Falcon 9 recoverable vehicle with 5m fairing. The launch vehicle upper stage would place the lander on a direct transfer to the Moon. The lander would provide navigation, power, communication and attitude control during the five day lunar transfer. Upon arrival at the Moon, the lander would perform the LOI maneuver to place itself into a 250-km circular polar orbit around the Moon. Once in the 250-km lunar orbit, the lander would be commanded by the flight operations team to begin landing operations. Landing would be targeted for ~9:00 am local lunar time to provide sufficient contrast for the terrain navigation and hazard avoidance systems.

The lander would perform a De-Orbit Insertion (DOI) maneuver to lower the lander orbit periapsis. A Braking Maneuver would bring the spacecraft down to an attitude of 100 m above the landing site with a velocity magnitude of 8.2 m/s (**Figure 12** in the **Main Report**). The spacecraft would perform a vertical descent to land with a terminal velocity of ≤ 0.5 m/s vertical and ≤ 0.1 m/s horizontal at 5 m above the surface above the surface. Terrain relative navigation (TRN) would be used to avoid landing on any hazards (**Section 1.2.4.4**). Once landed, the propulsion system would vent any remaining propellant using the ACS thrusters. The entire landing operation, from the start of the DOI to touchdown, would take a little over an hour.

1.2.3.2 Post-Landing Checkout Operations

After landing, a five-day lander checkout would be performed. The first 24 hours would be used to verify the health and safety telemetry received during landing from the lander subsystems. Then, the ground would command deployment of the panoramic camera and acquisition of landing site images (full azimuth and elevation to horizon) for site context. Ground operations would also command the lander to image the instrument platform and the footpads with PlanetVac and return those images to Earth for evaluation. Following completion of the post-landing checkout, instrument commissioning and initial data collection would begin. The estimated daylight remaining at the landing site after the 9:00 am local time landing would be ~261 hours (10.8 days), providing sufficient margin prior to lunar night should any anomalies occur during checkout.

The lander would have 24-hour DSN coverage throughout deployment and instrument commissioning. Once initial data collection began, the lander would need an hour of contact with the DSN each Earth day during the sunlit portion of the lunar day. There would be no planned contacts with Earth during the lunar night.



1.2.3.3 Surface Operations

After the lander has completed post-landing checkout operations, it would transition into normal surface operations. During the daylight portion of the lunar day (14.5 Earth days), the lander would collect sample and perform the science operations cycle (**Figure 7** in the **Main Report**), while recharging the lander batteries and communicating with Earth. It would then enter the lunar night for 14.5 Earth days. During lunar night, the science instruments would be in sleep mode. The lander subsystems would also enter a reduced power mode, with the communication subsystem in receive-only mode. By restricting primary communications to the sunlit portion of the lunar day, nighttime power use would be minimized. Nominal science and surface operations would continue for a year.

The available power would allow each sample analysis cycle to directly follow the reference flow described in **Appendix B2**. Surface operations would include two sample analysis cycles per lunar day, with time allotted for wakeup/checkout and shutdown. Sample gathering and triage would occur upon landing and again after samples 6 and 12, though this timing would be flexible. A second full set of context imaging would be acquired on Earth day 4, under mid-day lighting, though there is flexibility to acquire additional images under other lighting conditions. The downlink data rates (**Table 9** in the **Main Report**) would allow for the full sample science data of ~3 Gbits to be downlinked in the DSN pass following acquisition. The data and power profile for lunar surface ops is shown in **Figure 13** in the **Main Report**.

The lunar Geochronology Mission Operations Center (MOC) would manage sustained mission operations, long-term mission planning, and uplink of command loads. Lander automation features, driven by Flight Software (FSW) would allow day-to-day operations to become less complex over time, once the post-landing checkout operations and first several surface operation day/night cycles were complete. The Deep Space Network (DSN) would be used as the primary means for all communications during flight operations, post-landing checkout operations and surface operations. The lander would use Direct-to-Earth (DTE) communication links for forward commanding and for receiving science and housekeeping data back from the lunar surface. Link budgets show 10 Mbps for the lander to DSN link with 6.3 dB of margin (**Table 9** in the **Main Report**). The ground system architecture is shown in **Figure 14** in the **Main Report**.

1.2.4 Subsystem Details

1.2.4.1 Communications

The lunar Geochronology lander RF communications subsystem would use transceivers compatible with the DSN. X-band was selected because it provides sufficient bandwidth to offload the mission data volume within the allocated contact time with DSN and meets the bandwidth allocations for direct to Earth allocations. The design would incorporate a 0.5-m High Gain Antenna (HGA) with X-band 17 W RF amplifiers to provide the necessary radiated power for DTE contacts. A single +Z Low Gain Antenna (LGA) would also be included, supporting contingency or emergency communication contacts. The HGA would be gimballed to permit contact with the DSN during the 5-day transfer from Earth to the Moon and during the lunar surface mission. **Figure B3-4** shows a functional block diagram of the Lander RF communications subsystem.

Link budgets for DSN contact show 10 Mbps with 6.3 dB margin with DSN. The team also evaluated the utility of the Universal Space Network 11m class systems, which would provide 1.0 Mbps with 5.7 dB of margin. With a daily downlink volume of 327 Mbits/day, the USN would be a viable alternative to the DSN. **Table B3-3** summarizes the communication link analyses. **Table B3-4** provides the link analysis for DSN links and **Table B3-5** provides the link analysis for the USN links.

The communication subsystem design would use high-TRL class transceivers and power amplifiers. The HGA is available as a commercial product and the gimbals would be similar to those developed for Euclid (launching in 2022). No delivery risks would be anticipated for a expected 2030 launch date. A double pull double throw (DPDT) switch would be included after the diplexers allowing one communication slice access to both antenna systems.

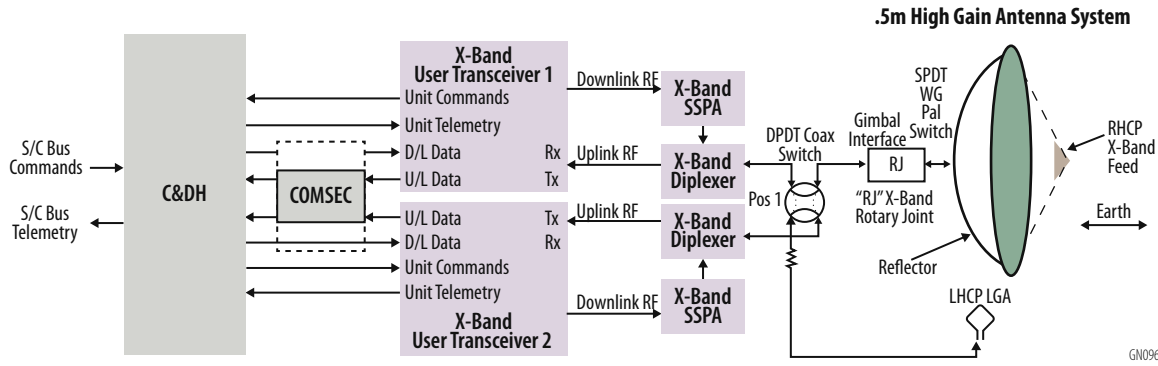


Figure B3-4: Lunar Geochronology lander RF communications subsystem functional block diagram.

Table B3-3: Lunar Geochronology lander RF communications subsystem summary of link analyses.

Link	Type	From	Transmit Power (W)	Antenna	To	Antenna	Data Rate	Margin (dB)
1	Downlink	Lander	17	LGA	DSN	34 m	12.0 ksps	3.2
2	Uplink	DSN	1000	34 m	Lander	LGA	32.0 kbps	8.9
3	Downlink	Lander	17	HGA	DSN	34 m	10.0 Msps	6.3
4	Uplink	DSN	200	34 m	Lander	HGA	32 kbps	33.5
5	Downlink	Lander	17	LGA	USN	11 m	1.0 ksps	3.5
6	Uplink	USN	1000 W	11 m	Lander	LGA	32.0 kbps	8.9
7	Downlink	Lander	17	HGA	USN	11	1.0 Msps	5.7
8	Uplink	USN	200 W	11 m	Lander	HGA	32.0 kbps	23.7

A great deal of international lunar communication coordination is still in development. For example, the NASA IOAG “The Future Lunar Communications Architecture” (2019) study presently limits X-band downlink symbol rates to 4 Mbps with GMSK modulation formats. The lunar Geochronology lander would use 10 Mbps, staggered quadrature phase-shift keying (SQPSK), and low-density parity-check (LDPC) 7/8 formats. Coordination with the lunar community would be required to use the higher data rate and LDPC to avoid a DSN contact time of 22.5 hours.

1.2.4.2 Structures

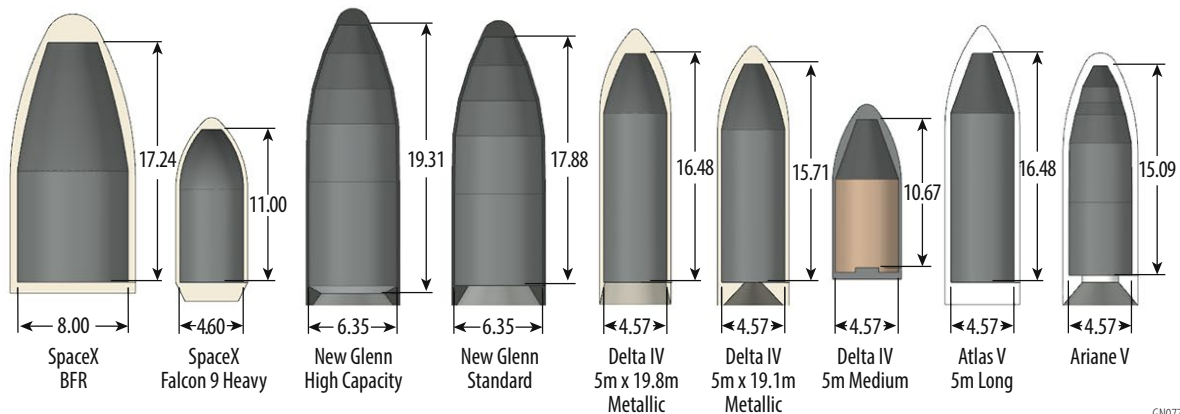


Figure B3-5: Launch vehicle fairing sizes.

Packaging all elements of the lunar Geochronology lander would be bounded by the Falcon 9 Heavy fairing size. The diameter of the fairing would be within scope of standard 5-m fairings used on the Delta IV, and Atlas (Figure B3-5), but the height would be significantly smaller. From a packaging standpoint, choosing the smaller fairing would ensure that a broad spectrum of fairings would be viable. All current launch vehicles have a limited center of mass offset. Although this was not a specific



Table B3-4: Lunar lander to DSN communication link analyses.

Lander X-band Downlinks			Lander X-band Uplinks		
8.4 GHz Downlink Lander LGA to USN 34m 410416 km Range LDPC 7/8			7.2 GHz Uplink USN 34m to Lander HGA 410416 km Range No FEC		
17 W	12.30 HPA pwr (dBW)	7.30 EIRP	1000 W	30.00 HPA pwr (dBW)	94.08 EIRP
	-3.00 pass loss (dB)			-1.50 pass loss (dB)	
	-2.00 Lander ant gain (dBi)		34.00 m	65.58 DSN ant gain (dBi)	
	-233.19 pass loss (dB)			-221.85 pass loss (dB)	
	-0.50 pointing + pol (dB)		-0.50 pointing + pol (dB)		
34.00 m	66.92 DSN ant gain (dBi)	38.63 G/T		2.00 Lander ant gain (dBi)	-33.76 G/T
1.0 db NF	-21.00 pass loss (dB)		2.0 db NF	-3.00 pass loss (dB)	
26.9 dBK	-27.29 Ant temp (dB)		24.7 dBK	-28.76 Ant temp (dB)	
100k sys			290k sys		
1.0 Msps	228.60 Boltz (dBW/Hz-K)		228.60 Boltz (dBW/Hz-K)		
	-40.00 data rate (dB-Hz)		-45.05 data rate (dB-Hz)		
	-3.85 Min Es/No (dB)		-9.59 Min Es/No (dB)		
	-3.00 imp (dB)		-3.00 imp (dB)		
	3.20 Margin (dB)		8.93 Margin (dB)		

Lander X-band Downlinks			Lander X-band Uplinks		
8.4 GHz Downlink Lander HGA to USN 34m 410416 km Range LDPC 7/8			7.2 GHz Uplink DSN 34m to Lander HGA 410416 km Range No FEC		
17 W	12.30 HPA pwr (dBW)	39.57 EIRP	200 W	23.01 HPA pwr (dBW)	87.09 EIRP
	-3.00 pass loss (dB)			-1.50 pass loss (dB)	
0.50 m	30.27 Lander ant gain (dBi)		34.00 m	65.58 DSN ant gain (dBi)	
	-233.19 pass loss (dB)			-221.85 pass loss (dB)	
	-0.50 pointing + pol (dB)		-0.50 pointing + pol (dB)		
11.00 m	66.92 DSN ant gain (dBi)	38.63 G/T		28.93 Lander ant gain (dBi)	-2.33 G/T
2.0 db NF	-1.00 pass loss (dB)		2.0 db NF	-3.00 pass loss (dB)	
26.9 dBK	-27.29 Ant temp (dB)		20.0 dBK	-28.16 Ant temp (dB)	
100k sys			290k sys		
1 Ksps	228.60 Boltz (dBW/Hz-K)		228.60 Boltz (dBW/Hz-K)		
	-70.00 data rate (dB-Hz)		-45.05 data rate (dB-Hz)		
	-3.85 Min Es/No (dB)		-9.59 Min Es/No (dB)		
	-3.00 imp (dB)		-3.00 imp (dB)		
	6.26 Margin (dB)		33.47 Margin (dB)		

GN106

design driver, it was a consideration that nudged the design to as squat a height as possible. This would have the additional advantage of a more efficient mass design.

The lander would be built around a co-axial central cylinder with a 1575 mm bolt diameter for attachment to the launch vehicle payload adapter via a Marmon clamp band or light band. The central cylinder diameter of 1575 mm would match the standard Falcon 9. To provide a longer moment arm for the thrusters, the main engines would be placed on the bottom deck in the corners providing significant ACS capability. Packaging the propulsion tank sizes and avoiding deployable systems where possible drove the mechanical design to have fixed solar arrays and non-deploying legs. Though simplifying the design, this would make packaging a challenge, particularly because of the requirement for 50-cm clearance to allow for a 50 cm boulder. From a packaging standpoint, the structure would be heavily driven by the two primary propulsion tanks (fuel and oxidizers) which consume a substantial portion of the lander volume. Smaller pressurant tanks would be also required but would be more easily accommodated. Placing the tanks inward toward the centerline would offer a significant reduction in the primary lander structure footprint, allowing fixed solar arrays and eliminating the need to deploy the legs.

The panoramic imagers and UCIS would need to be deployed on a 1-m boom attached using a single hinge to top of the “front” panel on the lander’s +x axis. A small Omni antenna would be also mounted on the front panel. The two PlanetVac sample handling systems would be mounted on the



Table B3-5: Lunar lander to USN communication link analyses.

Lander X-band Downlinks				Lander X-band Uplinks			
8.4 GHz Downlink Lander HGA to USN 11m 410416 km Range LDPC 7/8				7.2 GHz Uplink USN 11m to Lander HGA 410416 km Range No FEC			
17 W	12.30 HPA pwr (dBW)	-3.00 pass loss (dB)	39.57 EIRP	200 W	23.01 HPA pwr (dBW)	-1.50 pass loss (dB)	77.29 EIRP
0.50 m	30.27 Lander ant gain (dBi)	-233.19 pass loss (dB)		11.00 m	55.78 DSN ant gain (dBi)	-221.85 pass loss (dB)	
		-0.50 pointing + pol (dB)			-0.50 pointing + pol (dB)		
11.00 m	57.12 DSN ant gain (dBi)		28.09 G/T	0.50 m	28.93 Lander ant gain (dBi)		-2.33 G/T
2.0 db NF	-2.00 pass loss (dB)			2.0 db NF	-3.00 pass loss (dB)		
26.9 dBK	-27.03 Ant temp (dB)			20.0 dBK	-28.16 Ant temp (dB)		
100k sys				290k sys			
	228.60 Boltz (dBW/Hz-K)				228.60 Boltz (dBW/Hz-K)		
1.0 Msps	-60.00 data rate (dB-Hz)			32.0 Msps	-45.05 data rate (dB-Hz)		
	-3.85 Min Es/No (dB)				-9.59 Min Es/No (dB)		
	-3.00 imp (dB)				-3.00 imp (dB)		
	5.72 Margin (dB)				23.67 Margin (dB)		
Lander X-band Downlinks				Lander X-band Uplinks			
8.4 GHz Downlink Lander LGA to USN 11m 410416 km Range LDPC 7/8				7.2 GHz Uplink DSN 34m to Lander LGA 410416 km Range No FEC			
17 W	12.30 HPA pwr (dBW)	-3.00 pass loss (dB)	7.30 EIRP	1000 W	30.00 HPA pwr (dBW)	-1.50 pass loss (dB)	94.08 EIRP
	-2.00 Lander ant gain (dBi)	-233.19 pass loss (dB)		11.00 m	65.58 DSN ant gain (dBi)	-221.85 pass loss (dB)	
		-0.50 pointing + pol (dB)			-0.50 pointing + pol (dB)		
11.00 m	57.12 DSN ant gain (dBi)		28.09 G/T		-2.00 Lander ant gain (dBi)		-33.76 G/T
2.0 db NF	-2.00 pass loss (dB)			2.0 db NF	-3.00 pass loss (dB)		
26.9 dBK	-27.03 Ant temp (dB)			24.7 dBK	-28.76 Ant temp (dB)		
100k sys				290k sys			
	228.60 Boltz (dBW/Hz-K)				228.60 Boltz (dBW/Hz-K)		
1 Ksps	-30.00 data rate (dB-Hz)			32.0 Msps	-45.05 data rate (dB-Hz)		
	-3.85 Min Es/No (dB)				-9.59 Min Es/No (dB)		
	-3.00 imp (dB)				-3.00 imp (dB)		
	3.45 Margin (dB)				8.92 Margin (dB)		

GN107

two “front legs” to provide a short distance for the sample to travel to the triage station. The instrument deck would be mounted to the front panel, providing a shelf for the instruments to access the samples. The hazard avoidance and landing sensors (lidar, optical cameras, and laser rangefinder), would be mounted to the bottom deck.

The four main engines would be mounted to the bottom deck with 0.5 m clearance to the ground. The large radial distance from the engines to the center of mass of the lander would provide additional ACS capability. Four pairs of two ACS thrusters would be mounted to the edges of the bottom deck. A 4 m² solar array panel would be located on the top deck. Two pairs of two ACS thrusters would be mounted on the east and west sides, along with the 0.5-m, two-axis gimbaled HGA that is used during the cruise phase and during surface operations. Most heat-generating boxes would be mounted to a panel that includes radiators with louvers. Inside the structure, the four large batteries would be mounted in pairs and the other low power boxes would be located throughout various equipment panels.

The legs would use a simple tripod design, similar to Viking or Surveyor. The upper leg tube would consist of two telescoping tubes and a crushable material cartridge to provide energy absorption on impact and to passively stabilize the lander until all four legs touch the ground. The passive compliance in the landing legs would settle when a load beyond one-third of the landing weight were applied to any of the legs, until the load per leg drops below one-third (which would only happen when all four



legs touch) or the stroke distance of the stabilizer reaches a maximum allowable limit not defined in this study. Active leveling or other self-stabilizing concepts for four legs on uneven surfaces was not considered to be a driver and were not pursued in this study.

Sizing was based on conservative hand calculations and rules-of-thumb. For the purposes of structural sizing, the component masses in the MEL were approximated in the CAD model. This was used in sizing the structural elements. The resulting structural mass and the load it would carry (called “Relevant Mass”) was then used to calculate a structural efficiency of the design. The Relevant Mass is defined as the mass directly carried by the primary structure. The structural efficiency is defined as the mass of the primary structure divided by the Relevant Mass. The dry mass was used since all the propellant load would be in the central cylinder load path, providing a direct route to the launch vehicle. The study design would have an overall structural efficiency of 11%, which would be comfortably within the acceptable historical ranges of structural efficiencies on flight missions.

The lander engine cut-off would be expected to occur 5 m above the moon’s surface with a decent velocity at cut-off of 0.5 m/s. This would result in an impact velocity of ~4.5 m/s. At this velocity, the stroke of the legs during impact must be at least 87 mm to keep the landing g-loads at or below axial loads requirement of 12 g. This would exceed the Falcon 9 maximum launch loads of 6g axial and so became the driving case. The leg geometry would require the telescoping upper legs to compress a minimum of 58 mm to achieve the minimum vertical stroke distance. The worst-case scenario for keeping landing loads down would be if all four legs were to hit at the same time. In that situation, the crush force of the energy absorbing material must be low enough to maintain the minimum vertical stroke distance. This could be achieved with material selection and crush cartridge geometry. Many flight-qualified, crushable material options are available. The other landing scenario would be only three legs absorbing the impact energy. The crush strength of the energy absorbing material would be set by the four leg case.

The team designed the lander structure as a structural box with composite face sheet/aluminum honeycomb core panels using the clip and post method, a central cylinder, radial and equipment panels. Lateral stiffness would be adequate only when including the surrounding box structure. This suggests that the structural design, while very preliminary, would be reasonably conservative. Studies of stability gain compared to the mass and cost drove the design to a four-leg layout, though a tripod leg concept could also be implemented without requiring deployment. A wider stance using a deployable leg was considered but the addition of the hazard avoidance system obviated the need for a wider leg stance for the preliminary concept. Fixed arrays would fit within the launch vehicle and were chosen as the better option due to simplicity and expected mass and cost savings.

The structural concepts developed for this study would be within the current state-of-the-art and have heritage. It is likely that the landing dynamics, energy absorption, and self-stabilizing system would require customization for the specific landing environment, but the technology maturity is high, with numerous planetary landings providing heritage and extensive methodologies. Future work should include a detailed structural analysis, a propulsion tank mounting location study, detailed landing dynamics, kinetic energy absorption methodologies and trades, and study, selection and development of a baseline landing leg stabilizing system to ensure all four legs engage with the ground.

1.2.4.3 Propulsion

The lunar Geochronology lander propulsion subsystem would be a large regulated bi-propellant system. The propellant would be stored in COTS tanks and the main engines would be a set of four 4,000 N engines (AJ PN R-40B, **Figure B3-6**). Three redundant sets of 2 x 450 N engines (AJ PN R-4D-15 HIPAT, **Figure B3-6**) would be used for attitude control during maneuvers. Separate pressurization manifolds would be used to provide regulated pressure to both the fuel and oxidizer tanks. The system would be single fault tolerant. Each pressurization string would be fully redundant, and there would be separate strings of redundant attitude control thrusters. A schematic of the subsystem is shown in **Figure B3-7**.

The pressurant tanks would be isolated by redundant pyro valves during launch. The system would be pressurized during the transfer to lunar orbit insertion and a calibration maneuver would

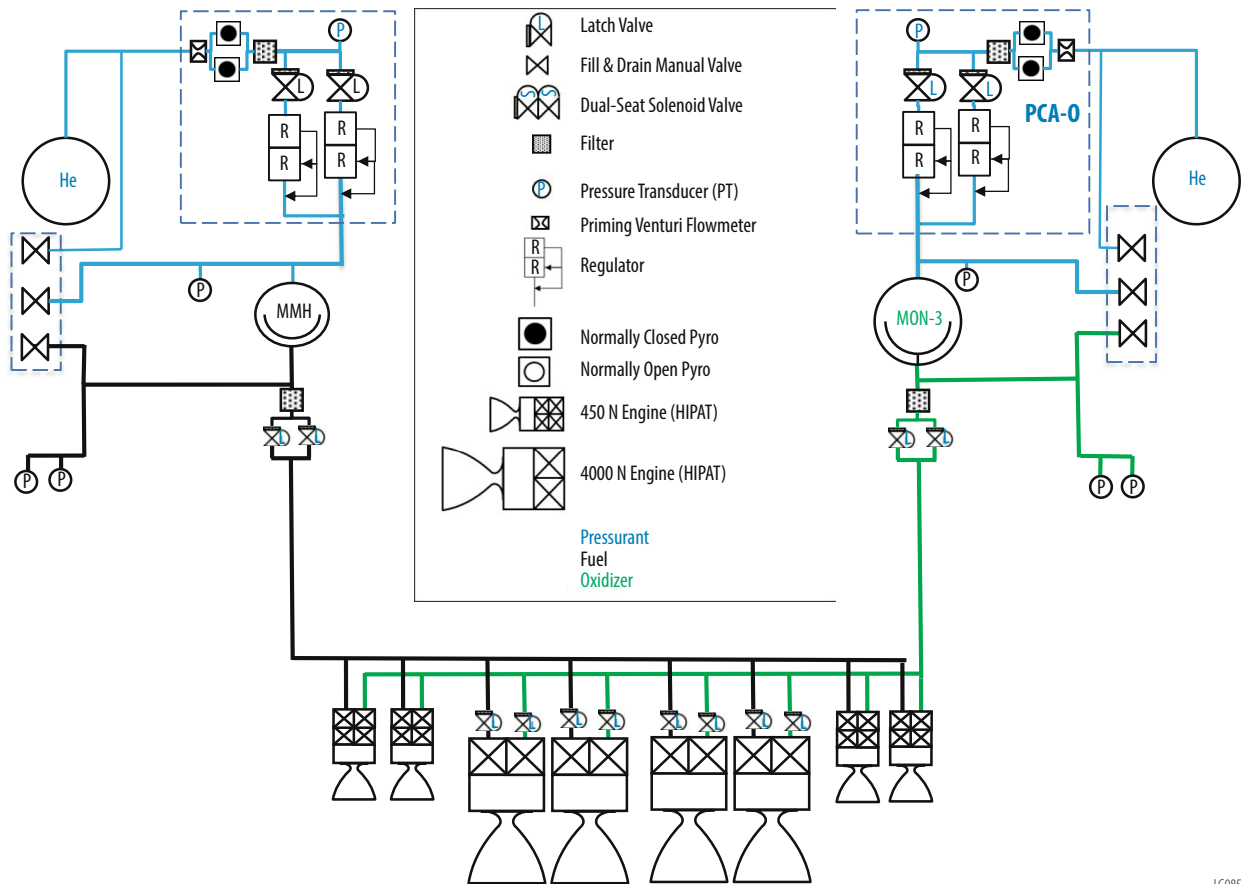


be performed. All maneuvers would be performed with the main engines, except for smaller orbit maintenance maneuvers. All of the components would be TRL 9. Several of the components would be long-lead items (*e.g.*, engines, pressure transducers, regulators, tanks).



GN074

Figure B3-6: R-40B 4,000N and R-4D-15 450N (HiPAT) rocket engines (not to scale).



LG085

Figure B3-7: Schematic of the lunar Geochronology lander propulsion subsystem.



1.2.4.4 Attitude Control System

The Attitude Control System (ACS) controls the orientation of the vehicle in the presence of disturbances. The principal requirements that influence the ACS design are the science requirements (target, needed accuracy/knowledge, needed orbital maneuvers). After safely landing, stabilizing, and initializing, the lander ACS would no longer be needed. The driving requirements for the lunar Geochronology lander are:

- Lander final actual position within 1 km of target site
- Lander final position knowledge within 2 km
- Lander final orientation relative to gravity (nadir) $<5^\circ$
- Lander velocity at touchdown @ 5 m ≤ 0.5 m/s vertical, ≤ 0.1 m/s horizontal

All lunar Geochronology lander ACS system components have flight heritage. The lander concept of operations would be based on both heritage and new algorithms. The new algorithms would be developed based on earth reentry vehicles and other proposed landers. A laser rangefinder and optical/IR camera would be used in combination with the navigation algorithms to provide positional knowledge of the lander. The position information would be used in closed-loop navigation and the TRN controller. The ACS block diagram is provided in **Figure B3-8**.

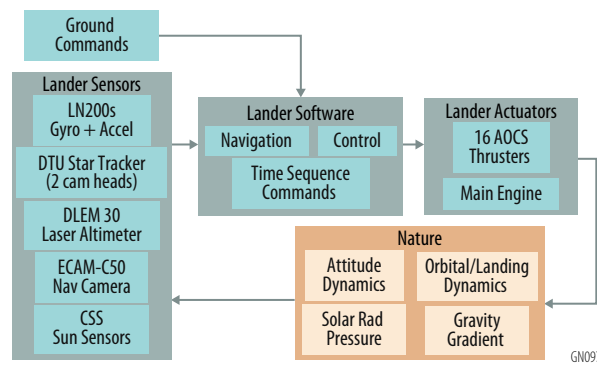


Figure B3-8: Lunar Geochronology lander ACS block diagram.

Prior to separation, the lander would be initialized with the stack configuration states. After separation and rate null, the lander ACS would start to deorbit the vehicle while maintaining the desired attitude. The navigation portion of the orbiter Flight Software (FSW) would be required to reduce the errors within the decent corridor. This part of the FSW would contain the Hazard Avoidance (HA) algorithms during the final portion of decent. Since there would not be ground in the loop, the navigation algorithm must be robust to account for uncertainties and disturbances. The lander ACS would have three modes: Stowed, ΔV , and Sun Safe (Sun Acq, Rate Null). The ΔV mode would receive attitude and positions targets from the navigation algorithm. This would be a deviation from most heritage ΔV modes and would require new flight software development. The descent and landing maneuvers are described in **Figure 12** in the **Main Report**.

The DOI would be the first maneuver the lander performs. The turn-and-burn maneuver would result in a ΔV of 50m/s and an altitude reduction of 240 km during the cruise phase. During this phase, the lander would maintain a power positive or communication attitude. After the cruise phase, a braking maneuver would be performed to produce a ΔV of 1,850 m/s and reduce the altitude to 100 m. During this maneuver, the lander would maintain the local vertical to horizontal attitude to place the ΔV opposite the ram direction. The final decent (50 m/s) would start at 100 m above the surface and the ACS thrusters would be used to maintain a vertical attitude (parallel to the gravity direction).



At a 5 m above the surface, the thrusters would be turned off and the lander allowed to fall the rest of the way.

TRN estimates the vehicle local relative position by comparing terrain maps loaded into memory prior to launch with terrain measurements from navigation sensors (lidar, optical camera, altimeter). Two different approaches to TRN estimates would be used: local position, and velocity. Two primary algorithms would be used for TRN: correlation and pattern matching. In the correlation approach, the TRN correlation algorithms place the sensor-generated terrain image (the patch) at every location in the map and measure the similarity between the patch and the map values. The location in the map with the highest correlation is the best estimate of the current position of the vehicle. In the pattern matching algorithm, predefined landmarks and their defined characteristics (lighting, shape, location, etc.) are matched with those in the sensor-generated images. The TRN algorithms require a significant amount of processing speed and memory to obtain estimates at a useful cadence to ensure the successful landing with hazard avoidance. The TRN architecture for the mission is shown in **Figure B3-9**.

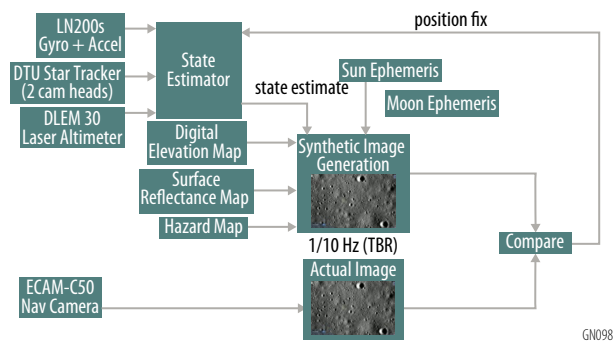


Figure B3-9: Lunar Geochronology lander terrain-relative navigation (TRN) architecture.

The ACS algorithms and technology associated with the lander are mature and have flight heritage. The separation mode would be an extension of existing launch vehicle modes that would be modified to meet the needs of the mission. This would also be true for the lander technology and algorithms. The key technology development for the lander would be the interface between the HA and the TRN. No ACS long-lead time components require more than 18 months. However, the ACS design and algorithm development would require development time. Flight software costs were accounted for using standard “wraps” in the costing exercise. In a mission proposal, trades should be performed to optimize the lowest allowable altitude for thruster operation, C&DH memory and speed for TRN, the TRN algorithm (pattern matching vs correlation) and map size and resolution, and HA maneuver size.

1.2.4.5 Avionics

The lander avionics would consist of a block-redundant system for Command and Data Handling (C&DH), attitude control sensors, power conditioning and distribution, mechanisms for launch locks, deployments and motors, and control of the main engine propulsion. The avionics implementation (**Figure B3-10**) would consist of three enclosures, C&DH unit, the Power System Electronics (PSE) and the Mechanism and Propulsion Unit (MPU).

All units would be block redundant and internally redundant within the mechanical enclosure. Only one block side would be hot (powered) at a time and the other block side would be cold (un-powered). There are two mechanisms for switchover from one block side to the other: autonomous or via hardware ground command. Autonomous switchover would occur when missing heartbeats from a processor to the Multi-Interface Cards (MICs), which perform the decision between them. The MIC would implement the hardware command decoder, Forward Error Correction (FEC) encoding of telemetry transfer frames, and the communication interface to the transponder or transmitter, among other functions.

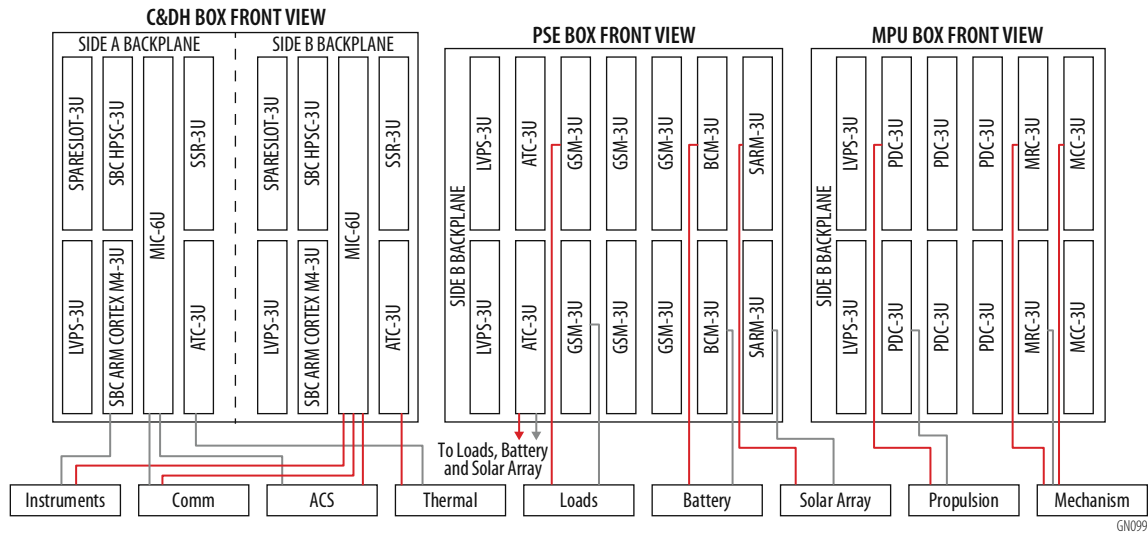


Figure B3-10: Lunar Geochronology lander avionics schematic.

The C&DH portion of the avionics would perform basic command and control of the lander, including Entry, Descent and Landing (EDL) to the lunar surface. This phase would be the highest-risk because a fault of a portion of the system may result in destruction of the lander. Because of the short duration of the EDL phase of the mission, and therefore the low probability for a fault in the portions of the system that could end the mission, the avionics would not be designed to fail operate (*i.e.*, fly-through fault operation).

The C&DH would use a low-power processor based upon the VORAGO ARM Cortex-M4. The processor chip would have a power of less than 1W; the board peripherals would use an additional 3W. This would help reduce required power during the lunar nighttime, reducing the required battery capacity. During science operations, the processor would execute stored commands, gather telemetry and housekeeping data, and perform Fault Detection, Isolation, and Recovery (FDIR). The processor would perform Consultative Committee for Space Data Systems (CCSDS) Acquisition of Signal (AOS) transfer frame generation of telemetry data and pass it to the Multi Interface Card (MIC). The MIC would provide the communication interface function, perform Forward Error Correction (FEC) encoding (Reed Solomon or Turbo), and interface to the transponder (S-band and X-band).

A second Single Board Computer (SBC) based on the High Performance Spacecraft Computing (HPSC) chip that uses several ARM Cortex A53 64 bit processors or other rad hard high performance processor, would be used for TRN processing during EDL. This SBC would require higher power and therefore would only be used during EDL. After landing, it would be powered down.

The MIC would hold the communications and sensor and instrument interfaces. The C&DH would be compatible with typical spacecraft interfaces, such as RS-422 UART interface, I2C, LVDS interfaces, SpaceWire and Mil-Std 1553B. The instrument interfaces would reside on the MIC along with the communication interface. The MIC board also would have the GN&C sensor interfaces such as sun sensors, IMU, accelerometers, star tracker, etc., as well as typical spacecraft interfaces for other avionic units. The MIC would also carry communication functions (transfer frame FEC encoding, hardware command decoding and execution, transponder interface, and transmitter interface for the different RF bands). The MIC's non-volatile memory as well that may be used to supplement or replace the SSR depending upon the memory size requirements. The Mission Elapsed Timer (MET) on the MIC would provide the One Pulse Per Second interface (1 PPS) to spacecraft sub-systems, as well as the watch-dog timers and logic that determine block switch-over. Because of this, the MIC would be the only card that would be powered on both sides. The two MICs would communicate to help determine the switch-over condition using Triple Modular Redundant (TMR) logic. The dual,



redundant Low Voltage Power Supply (LVPS) would also be powered on both sides to support powering of the redundant side MIC.

The dual, redundant Analog Telemetry Cards (ATC) would have analog digital converters (ADC) and analog multiplexers to gather temperature and other telemetry. The dual, redundant Solid State Recorders (SSR) would have 4 TB of non-volatile memory (Flash) for DTN relay communication storage. The C&DH enclosure would have dual, redundant Low Voltage Power Supplies (LVPS) to power the cards in the C&DH.

The avionics' Power System Electronics (PSE), which would be redundant within the same enclosure, would perform solar array current regulation for the spacecraft loads, control the battery charging, switch power distribution to various spacecraft loads and gather telemetry for power system functions. The dual, redundant Solar Array Regulation Modules (SARM) would have the Field Effect Transistors (FETS) to switch the solar array strings for current regulation. The Battery Charge Module (BCM) card would perform battery charge control. The Geochronology lander would use one per battery, though there are examples where redundant systems use a single battery (e.g., Lucy). Two Analog Telemetry Card (ATC) cards, one primary and one redundant, would read analog telemetry for the PSE. The power switch function would use six Generic Switch Module (GSM) cards, three for the primary side and three for the redundant side. Finally, the PSE would have one internally-redundant housekeeping power supply.

The MPU would serve the mechanisms functions, including launch locks, motors, and propulsion valve drive. Pressure sensor telemetry would also go to the C&DH Unit. All cards would have I2C interfaces. The Motor Controller Card (MCC) would have H-bridge circuits and relays to control 3-phase stepper motors. Each MCC would have the ability to drive four motors. Two MCCs would be baselined for redundancy. The Mechanism Release Card (MRC) would have the ability to control eight mechanisms, switching both high and low side with an arm switch. Two MRCs would be baselined for redundancy. The Propulsion Drive Card (PDC) would have the ability to control eight valves, switching both high and low side with an arm switch. Six PDCs would be baselined for redundancy. Lastly, the MPU would have a dual, redundant LVPS card to provide secondary voltages to the MPU cards.

The EDL operation would use a high performance processor for TRN. After landing, the high performance processor would be powered down and a low-power processor would be used for lunar surface operations. Board designs would be based on the Eurocard form factor 3U and 6U. The C&DH backplane unit would use cPCI. For the PSE and MPU, the backplane would be based on an I2C interface. The HPSC design has heritage to Mars 2020 and is TRL 7.

1.2.4.6 Power

The lunar Geochronology power system would consist of solar arrays, a secondary battery, and supporting power electronics. The power system configuration would be primarily driven by the length of the lunar night, which drives thermal loads and energy storage requirements. Two standard fixed solar array panels would be baselined, one mounted on the east and one on the west side of the lander. TJGaAs solar cells with bare cell efficiency of 29.5%, a solar constant of 1,353 w/m², array operating temp of 120° C, and Space Environmental Effects and Education System (SPENVIS) solar array degradation factors, and an assumed latitude of 10°N were used to derive the array area requirement. The selected design would use two panels, each with 3.57 m² active area (3.96 m² total substrate area each). The arrays would be mounted at a 45° angle on either side of the lander and would produce a daylight peak power of 928W BOL / 785W EOL at lunar noon. An additional 4m of array are placed on top of the Lander. 1,176 AH Li-ion battery, optimized for low temperature operation, would be used to support night loads. The Power System Electronics (PSE) would be a heritage 28VDC battery dominated bus included as cards in the avionics package. The PSE would control battery charging and power distribution. The EPS characteristics are shown in **Table B3-6**. All power subsystem components are currently TRL 6 or above, including state-of-practice solar array (lunar) TRL of 7, battery TRL 7, PSE, 28 V DC battery dominated bus, TRL 7, and harness, TRL 7.

Table B3-6: Lunar Geochronology lander EPS characteristics.

	W/AH	Mass (kg)	Area/Volume
Solar Array	1,570.9 W	26.9	12 m ²
Battery	1,176 AH	320	0.176 m ³



The key trade for the lunar mission was the solar array + battery only system vs. a solar array + battery + Next-Generation Radioisotope Thermoelectric Generator (NGRTG) system. Because the design would close with the solar array + battery option, the team decided not to pursue designs that would use the NGRTG.

1.2.4.7 Thermal

The lunar equatorial region is a challenging location to stay within temperature limits; the daytime has regolith temperatures nearing 110°C during local noon (plus $\sim 1420\text{ W/m}^2$ of solar load), and the nighttime has regolith temperatures nearing -180°C (with zero solar input). **Figure B3-11** shows a plot of lunar regolith temperature vs. time during the daytime.

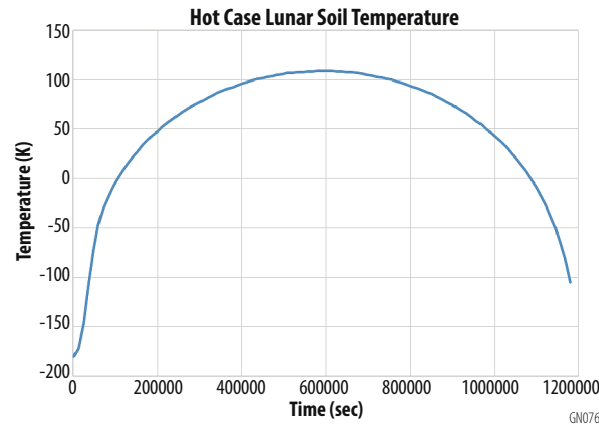


Figure B3-11: Lunar regolith daytime temperature vs. time.

The thermal system would be designed to dissipate 527 W of electronics power during the daytime and stay above survival temperatures during the night while only dissipating 25 W . This would provide margin against the MEV daytime average power usage of 323 W and MEV nighttime average power of 50.5 W . Two radiators would be used on the anti-sun side of the lander to dissipate heat from the avionics, communications, and instrument subsystems. One radiator (1.3 m^2) would be dedicated to the CDEX and UCIS DPU, which have much higher lower temperature limits than other instruments, and a separate avionics radiator (3.8 m^2) would dissipate heat for all other electronics boxes. A heat pipe would transfer heat from the instrument electronics boxes and Li-ion batteries to the radiator. The solar arrays would never be “open circuit” during daytime operation, resulting in lower maximum temperatures. The propellant would be vented after landing, eliminating the need to thermally control the propellant tanks, propulsion lines, and valves. This would avoid damage to the lander structure that could occur if there were frozen propellant in the propulsion system. **Figure B3-12** shows the external and internal thermal models of the lander.

The lander would use louvers that open during mid-daytime hours so that the full radiator area could dissipate 527 W to the environment, partially close during morning and afternoon when the environment would be cooler, and fully close at night. With the louvers totally closed, the lander’s electronics boxes would remain above their cold temperature limits with very little power dissipation (25 W). Bi-metallic springs would passively actuate the louvers’ vanes as the temperature changes, so no power or electronic circuitry would be needed for their operation. Thermal models for hot- and cold-biased conditions are shown in **Figures B3-13** and **B3-14**.

There would be two risks with using louvers: 1) dust could work its way into the louver blades preventing their actuation, and 2) the extremely low required emissivity of the louvers (gold plating or polished aluminum) could be increased by dust settling on the louvers.

All thermal hardware has a high TRL. Louvers have been used on a variety of spacecraft, including Parker Solar Probe, New Horizons, Messenger, and Lucy. Louvers may take 12 months between initial



contract signing and delivery, but this could be planned into the overall lander schedule. Currently, there is only one spaceflight-qualified louver vendor for (Sierra Nevada Corp.), so competing programs might vie for resources.

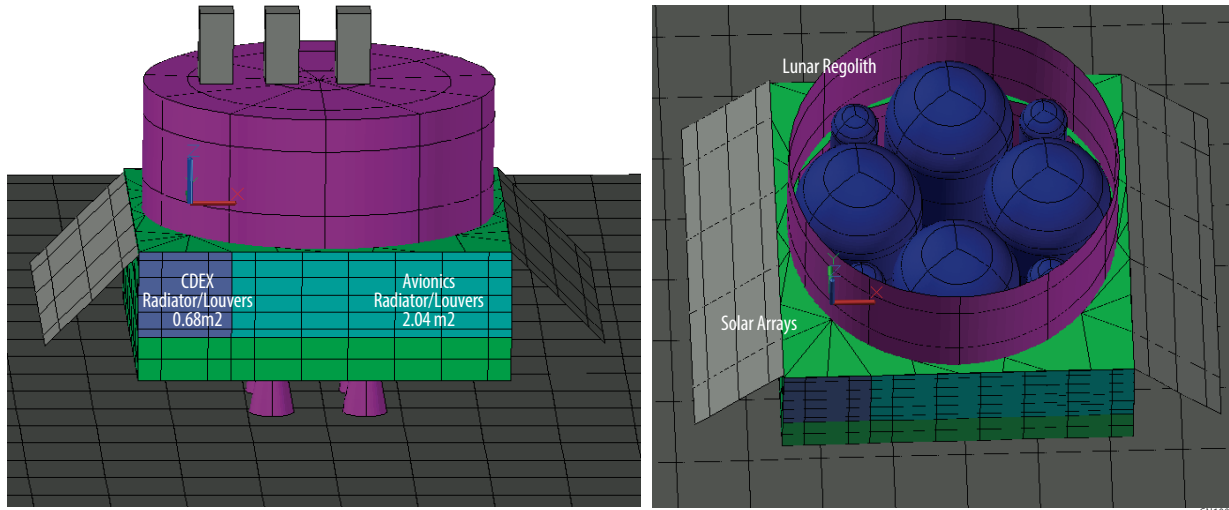


Figure B3-12: Lunar Geochronology lander external thermal model.

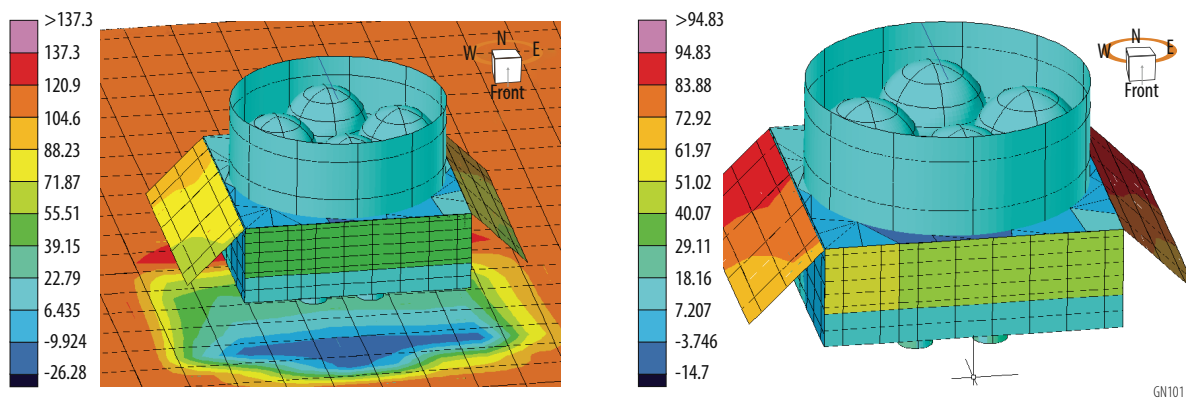


Figure B3-13: Lunar Geochronology lander hot-biased temperatures at lunar noon.

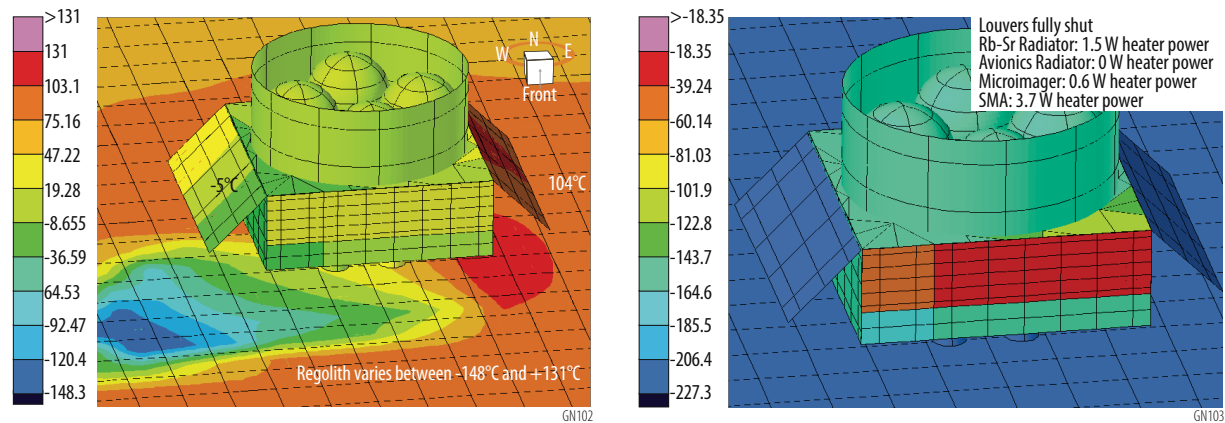


Figure B3-14: Lunar Geochronology lander hot-biased temperatures at lunar 3pm.

Figure B3-15: Lunar Geochronology lander cold-biased temperatures.



1.3 Vesta Geochronology Hopper

1.3.1 Overview

The Geochronology flight system for Vesta (**Figure 15** in the **Main Report**) fits within the Falcon 9-R fairing. The Vesta mission ACS, avionics, and propulsion subsystems would be identical to the lunar lander concept. The power, communications, structures, and thermal subsystems would be appropriately modified for Vesta, as well as the ability to hop to a second site. Instrument accommodation on the Vesta hopper would be identical to the lunar concept, but the surface operations would be different. Since Vesta has a short night (2.65 hours), there is no need to stop instrument operations like there is on the Moon with its 14.5 Earth days of night. **Tables 10** and **11** in the **Main Report** summarize the Vesta Geochronology hopper characteristics.

1.3.2 Mission Design

The Vesta mission design comprise the same three primary phases as the lunar mission design: flight operations, post-landing checkout operations and surface operations, with the addition of a hop phase and a second surface operations phase. Flight operations would be composed of three subphases: launch and cruise, 250 km-altitude circular polar Vesta orbit, and landing. Upon arrival at Vesta, the lander would remain in orbit for ~6 months to develop a terrain map and conduct landing rehearsals, similar in fashion and process to the OSIRIS-REx mission (Williams *et al.*, 2018, Leonard *et al.*, 2019). Further study of the mapping needs and approach is recommended using the lessons learned from OSIRIS-REx. The Vesta landing sites considered in this study were the Rheasilvia central peak (-71.95°N, 86.30°E) and Marcia crater (15°N, 180°E) (**Figure B3-16**). The Vesta Geochronology mission would require mission operations to manage command and control of the lander; the Mission Operations Center (MOC) detailed in **Section 1.2.3.3** would also be applicable for Vesta.

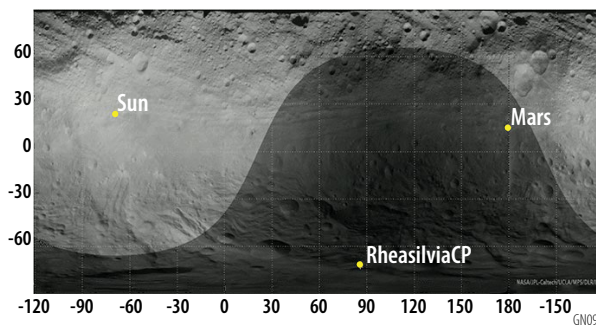


Figure B3-16: Vesta landing sites in this study: Rheasilvia basin central peak and Marcia crater.

The team performed a trade study of possible trajectory designs. Trade parameters included the earliest launch readiness date, launch vehicle, propulsion type (chemical high-thrust or solar electric propellant), inclusion of gravity assist(s), and maximum time of flight (TOF). The Vesta mission design summary is shown in **Table 12** in the **Main Report**. The parameters traded to arrive at the Vesta transfer are summarized in **Table B3-7**.

The results from this trade study are summarized in **Figure B3-17**. For each trajectory optimization, the objective was to maximize the landed mass before the hop. Some options presented higher delivery masses at particular launch periods. These would be ideal as primary launch periods, as they provide the most efficient propellant use. Given the nature of chemical propulsion systems, this would be true even for mission that require lower delivery masses; trajectory solutions for mission using chemical propulsion can easily scale mass using the rocket equation.

The hop trajectory was evaluated by solving Lambert's problem with Vesta as the primary body (**Figure B3-18**). The rotation rate of Vesta was also taken into account. Calculations show 230 kg of extra propellant would be required to hop to Rheasilvia from Marcia, and 212 kg to hop from Marcia



from Rheasilvia. The resulting launch wet masses for a hop to a second landing site are 10,621 kg and 10,603 kg, respectively. These two final values come from adding the extra propellant amounts to the 10,391 kg launch wet mass of the baseline trajectory to land on Vesta. Thus, unlike the Moon and Mars missions, the amount of propellant required by the Vesta mission to add a hopping maneuver would be feasible. The Falcon Heavy Expendable would be capable of launching the full spacecraft wet mass, including the fuel required to perform a hop (Figure B3-19). A launch mass of 10,621 kg (propellant for the hopping phase included) is below the Falcon Heavy Expendable curve for a launch C3 of 7.73 km²/s².

Table B3-7: Alternatives evaluated in Vesta transfer orbit trade study.

Thruster	LRDs	Max. ToF (years)	Flyby	Launch Vehicle	Power	Solar Arrays
Chemical <i>I</i> _{sp} 324 sec	Jan. 1 2028 – Dec. 31 2032 @5-day step	5 10 14	Mars (M) E-M M-M E-M-M M-M-M E-M-M-M	Falcon Heavy Exp. Vulcan Centaur Falcon Heavy Rec. Falcon 9 ASDS	-	-
Low thrust AEPS x 2 T6 x 3	Jan. 1 2028 – Dec. 31 2032 @15-day step	5 10 14	Direct Earth (E) Mars (M) E-E E-M M-M	Falcon Heavy Exp. Vulcan Centaur Falcon Heavy Rec. Falcon 9 ASDS	1/ <i>r</i> ² 15% margin	29kW @1AU

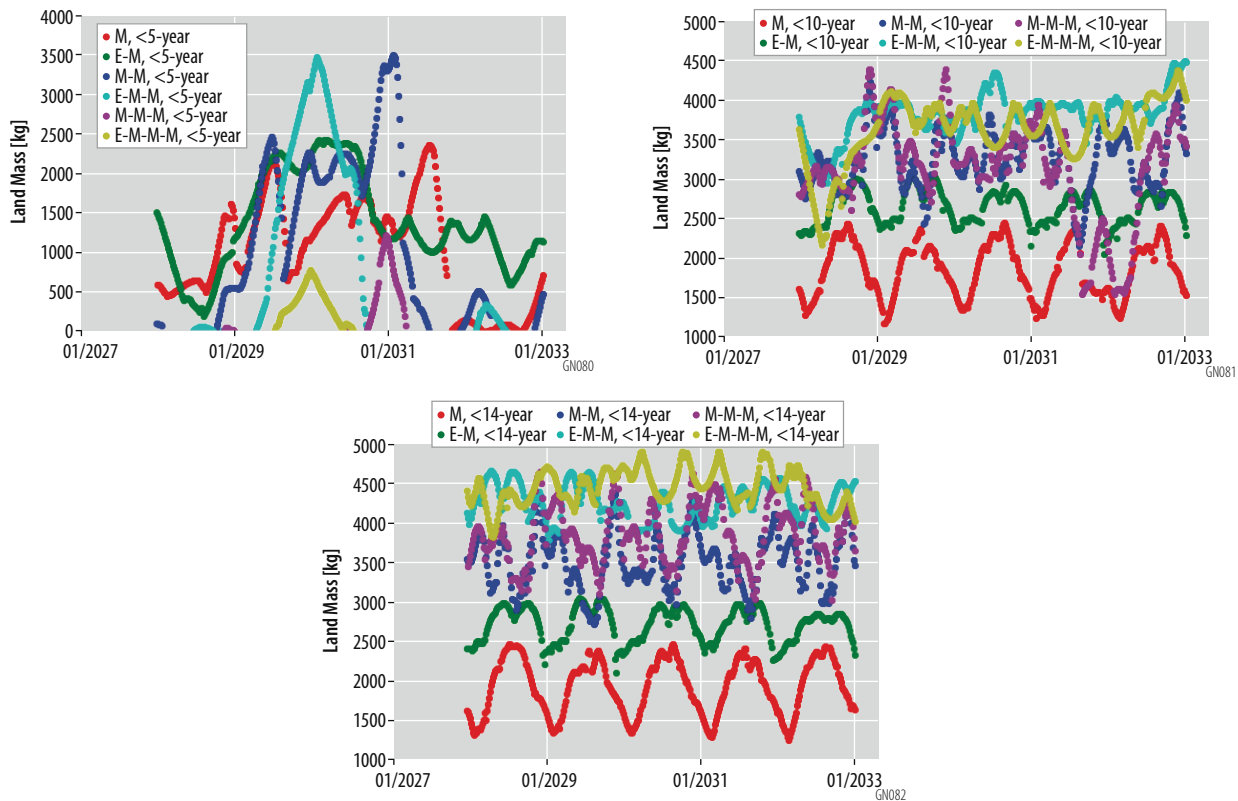


Figure B3-17: Vesta hopper mission dry mass vs. launch date: (top) TOF < 5 years, (right) TOF < 10 years, (bottom) TOF < 15 years.

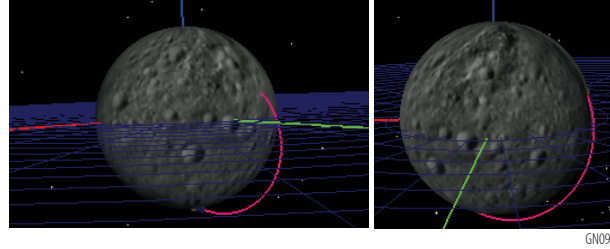


Figure B3-18: Two views of the Vesta hop.

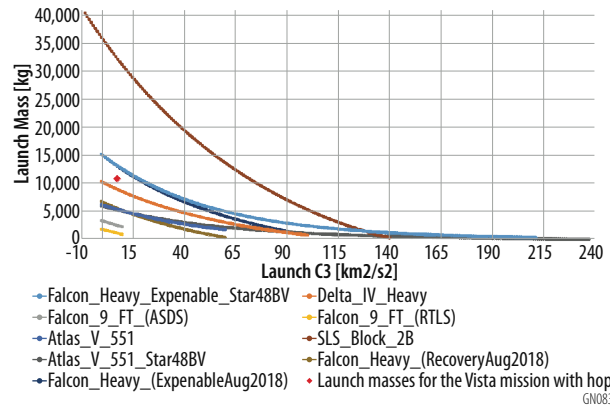


Figure B3-19: Performance comparison of current and future operational launch vehicles.

1.3.3 Mission Operations

1.3.3.1 Launch and Cruise Operations

The Vesta Geochronology mission would launch from Cape Canaveral, Florida, on a Falcon 9 Heavy Expendable vehicle with a 5-m fairing. The launch vehicle upper stage would place the lander on a direct transfer to Vesta. The lander would provide navigation, power, communication and attitude control during the ~49 month transfer. The final trajectory selection was based on a compromise of a short TOF with the most efficient propellant option. Similar to the analysis for the Moon, this scenario would use four Aerojet Rocketdyne R-40B engines, producing 4000 N of thrust each at an Isp of 293 s. The baseline transfer orbit resulting from the trade study would be an orbit showing the peak in the 2-Mars-Flyby orbits (blue dots) in **Figure B3-17**. The launch window to achieve the baseline orbit would be about 20 days. The baseline transfer orbit would last for less than five years and carry sufficient margin for the lander with total landed mass of 1,479.7 kg (CBE) and 1,720.9 kg (MEV). The main trajectory events are summarized in **Table B3-8** and **Figure B3-20**.

Table B3-8: Baseline trajectory main events for Vesta.

Event	Date	MEV Mass (kg)	Δ (m/s)
Launch	01/29/31	6,707.5	7.73704*
DSM	05/31/31	5,627.6	485
Mars Flyby 1	08/20/31	5,627.6	-
Mars Flyby 2	07/07/33	5,627.6	-
DSM	04/23/34	4,186.8	835
Vesta Arrival	03/07/35	2,424.0**	1628

*Launch C3, km²/s²
 **Final mass including propellant for hop and margin

1.3.3.2 Vesta Orbit Operations

Upon arrival at Vesta, the lander would perform an orbital insertion maneuver to place itself into a 250-km circular polar orbit around Vesta. Given that the Vesta environment is already known from the Dawn mission, this time would be allocated to creating a high-resolution map and performing landing rehearsals. The study assumed that the TRN sensors would be sufficient for mapping. It is likely that additional dedicated cameras will be needed. The spacecraft would be required to be on Vesta's



dayside for landing and science operations. The illumination time at Rheasilvia and Marcia during the mission’s timeline is shown in **Figure B3-21**. To provide sufficient contrast for the terrain navigation and hazard avoidance systems, operations would be timed such that the spacecraft would land early in the Vestan day.

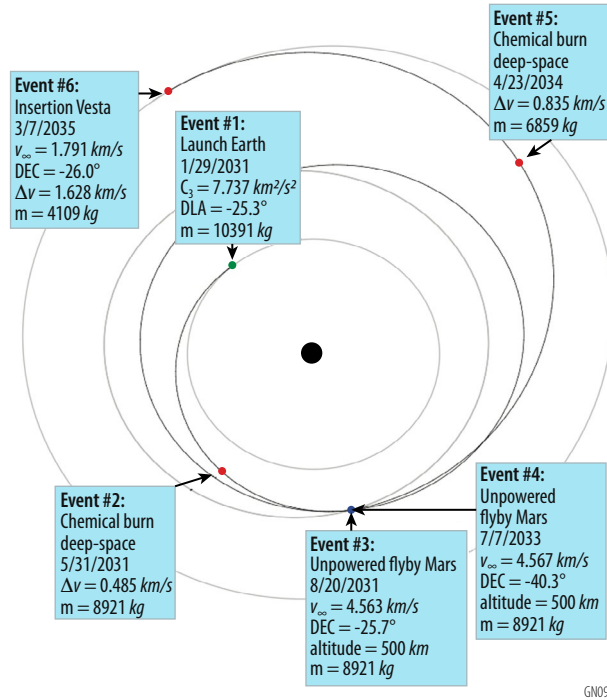


Figure B3-20: Baseline trajectory for the Vesta Geochronology mission.

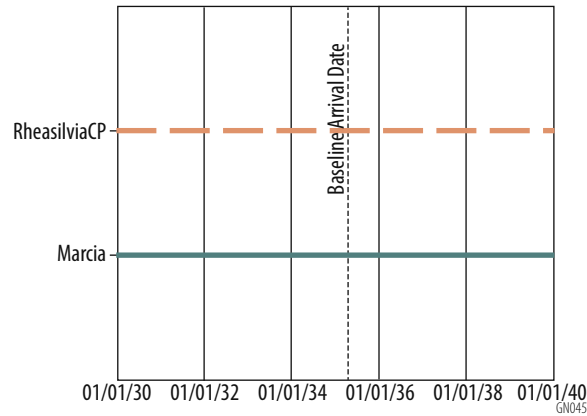


Figure B3-21: Sunlight availability at Rheasilvia central peak and Marcia crater.

1.3.3.3 Landing Operations

Landing operations would be similar to the lunar landing operations (**Section 2.3.1, Figure 10** in the **Main Report**). The main differences would be due to Vesta’s gravity and terrain, which may result in timing adjustments for the various maneuvers.

1.3.3.4 Surface Operations

The Vesta science concept of operations would be essentially the same as the lunar concept, except for timing the context imaging to match local lighting conditions. The same five-day lander checkout



(Section 2.3.3) would be performed. Following completion of the post-landing checkout, instrument commissioning and initial data collection would begin. Available power would allow the sample sequence (Appendix B2) to occur uninterrupted over its nominal ~24 hour duration, or approximately 5 Vesta days. Science operations would not be paused during the Vesta night. At a downlink rate of 50 Kb/sec and assuming 1 DSN pass per Earth day at 50% efficiency, it would take 6 hours of DSN contact to downlink the daily average data volume of 507 Mbits. Context imaging would be spread out within the first 20 Earth days of operations to maintain consistent lighting conditions. Surface science would conclude 130 terrestrial days from landing and data downlink would conclude at Day 142 (Figure 16 in the Main Report). After completing the science and downlink operations at the first site, the lander would hop to the second site. Surface science operations would be identical at both Vesta sites.

1.3.3.5 Hopping Operations

Once the science goals were accomplished at Rheasilvia central peak, the lander would retract its solar arrays and hop to the Marcia crater site. The same TRN and HA algorithms would be used to ensure a safe landing at the second site. The hop between Rheasilvia central peak and Marcia crater would have a duration of ~38 minutes.

1.3.4 Subsystem Details

1.3.4.1 Power

The Vesta Geochronology mission power system would consist of solar arrays, a secondary battery, and supporting power electronics. The power system configuration would primarily be driven by the low solar flux when Vesta is at its furthest point from the sun in its orbit (217w/m^2). TJGaAs solar cells with bare cell efficiency of 29.5% and normal solar array losses would generate 36W/m^2 BOL and 32w/m^2 EOL. The team baselined two furled flexible solar arrays, each providing 16m^2 each of active cell area. The arrays would be oriented at the first landing site (15°N latitude) with wings deployed north and south and rotated to track the sun for the 2.7-hr Vesta day, providing 1114W BOL / 990W EOL of continuous power for science and avionics.

After science operations at the first landing site were complete, the solar arrays would be furled and the spacecraft would hop to the second site. At the second site (72°S latitude), the arrays would be oriented east and west and rotated to offset the angle of latitude. In this configuration, the arrays would provide a peak power of $2,736\text{W}$ BOL / $2,432\text{W}$ EOL at orbit noon. An additional, body-mounted solar panel (4m^2) would power avionics for the flight to Vesta. A 37 AH, high energy density Li-ion battery would support avionics loads during the Vesta night. The Power System Electronics (PSE) would be a heritage 28 V DC battery-dominated bus included as cards in the avionics package. The PSE would control battery charging and power distribution.

The flexible solar array envisioned for use on the Vesta Geochronology mission demonstrated deployment and furling on the International Space Station in 2016 and is TRL 6. Furling array development involves some technical risks that require further evaluation before being proposed, including use in Vesta's low-light, low-temperature environment.

1.3.4.2 Communications

The DSN would be used as the primary means for all communications during the flight operations, post-landing checkout operations, surface operations and hop phases. The lander would use DTE communication links to forward commands and to receive science and housekeeping data. Link budgets show 50 Kbps for the lander to DSN link with 3.1 dB of margin. Communication subsystem details are summarized in Table 18 in the Main Report.

1.3.4.3 Thermal

The Vesta Geochronology lander thermal system would be designed to dissipate heat from the instrument, avionics and communications systems using radiator patches on the lander body. The



radiators would also be thermally connected to the propulsion system to eliminate the need for propulsion heaters. Vesta receives 290 W/m² of solar load when at its closest point to the sun during the day (compared to 1375 W/m² at Earth) and rotates every 5.3 hours from full sun to eclipse (**Table B3-9**). The lander's radiation sink would be required to dissipate 515 W of electronics power during operation. **Figures B3-22** and **B3-23** shows the external thermal models of the Vesta lander. **Figure B3-24** shows the two radiator temperatures as a function of time throughout the rotational period.

The thermal design would use two radiators on the lander, sized to keep the electronics within operational temperature limits without the use of heaters. One radiator (0.56 m²) would be dedicated to the CDEX instrument and the UCIS DPU, which have higher lower temperature limit than the other electronics. A second avionics radiator (1.56 m²) would dissipate heat for all other instruments and electronics boxes. Small patch radiators may be used for every box, or spreader heat pipes could be embedded in the lander's radiator face to help spread heat between boxes. The lander's Li-ion batteries would either be mounted to the avionics radiator or would need heat pipes to thermally connect them if mounted in a remote location. A heat pipe would be used to transfer heat from instruments and their electronics boxes to the radiator if not co-located. Heat pipes would also connect the radiator panel to the propulsion thrust tube, keeping the propulsion system (tanks and lines) warm by sharing thermal heat from the radiators, keeping them above the hydrazine freezing point at all times. All thermal hardware has a high TRL, having been used extensively in other planetary missions.

Table B3-9: Vesta solar characteristics.

Value	
Solar Flux (W/m ²), Hot Biased	290
Albedo	0.43
Planetary Infrared	Calculated within thermal model

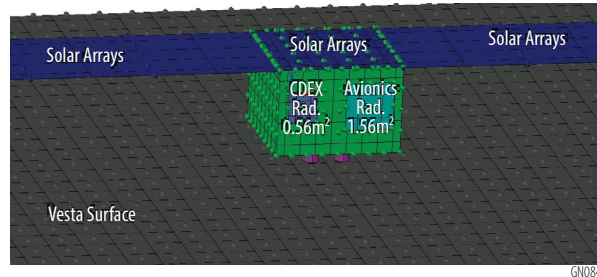


Figure B3-22: External thermal model of the Vesta Geochronology lander.

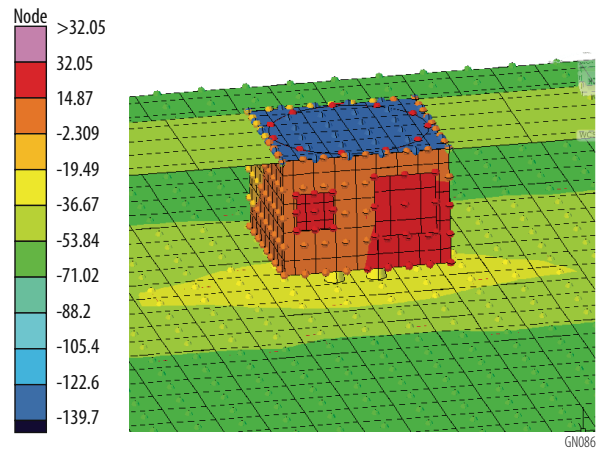
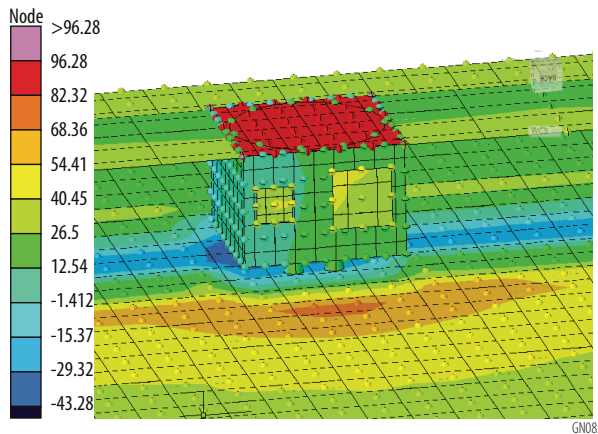


Figure B3-23: Vesta Geochronology lander hot daytime temperatures (left) and cold nighttime temperatures (right).

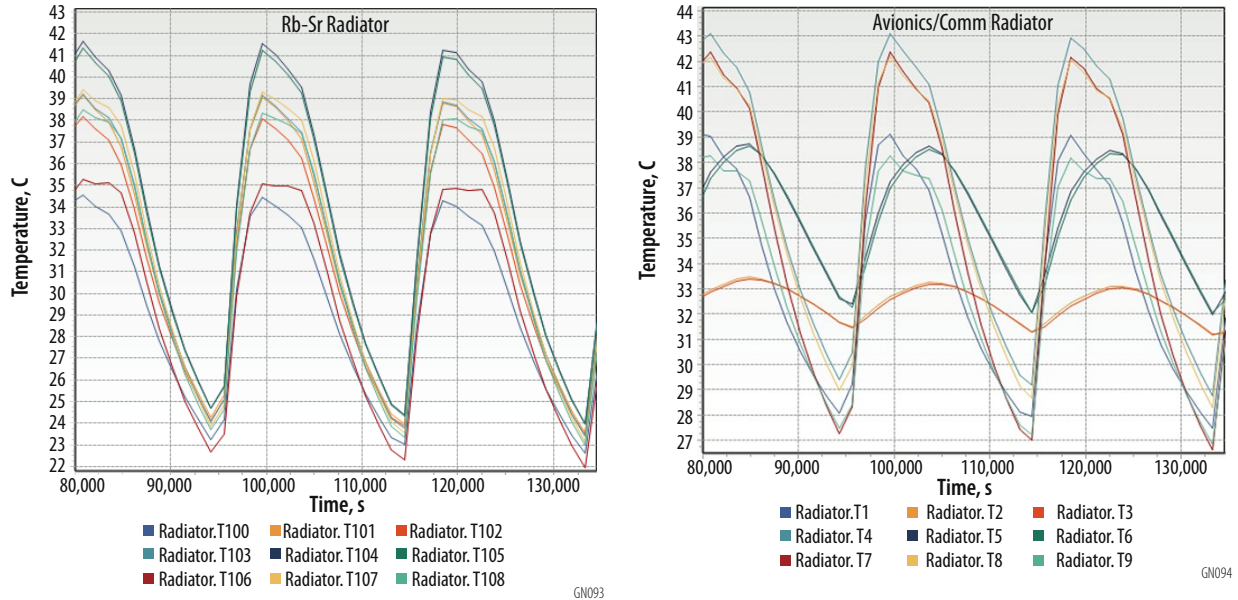


Figure B3-24: Vesta Geochronology lander radiator temperatures for (left) CDEX radiator and (right) avionics and communications radiator.

1.4 Mars Lander

1.4.1 Overview

Lockheed Martin (LM) conducted a study to investigate how the full Geochronology payload and operations could be implemented for Mars. The lander and EDL system would be based on the successful InSight and Phoenix missions, scaled to land 180 kg of payload and operate for ≥ 180 sols. No TRL development is required. Specific modifications include extending the deck and bipods to accommodate the instruments, increasing the aeroshell diameter, adding three MR-104s and a 4-inch stretch (~XSS-11 tank) to the descent manifold, and using a Viking-sized parachute to accommodate the larger mass. The mission design considered all Mars launch opportunities between 2025 and 2035 and selected the 2030 window for its ability to target a landing close to solar longitude (L_s) $L_s=0$ to maximize operations time before the onset of dust storm season. Based on this analysis, the Mars Geochronology mission would launch between July 12, 2030 and August 1, 2030 to land on October 30, 2032 at $L_s=73$.

Figure 17 in the **Main Report** shows the Mars Geochronology lander stowed in the heat shield. To accommodate the increased mass of the Geochronology payload relative to Phoenix or Insight, the deck and aeroshell would be scaled up. Scaling up the aeroshell and launch mass would cause all primary structures to increase in mass (and would increase the size of the aeroshell).

1.4.2 Mission Design

The LM team developed a candidate baseline trajectory to perform a direct landing on Mars in the Nili Fossae region (Lat 21°N , Lon 74°E , elevation -1500 m MOLA relative). The team did not perform EDL Monte Carlo on the study baseline trajectory. A desired trajectory would arrive close to $L_s=0$, but not before, allowing at least 180 sols for operations before dust storm season would begin. Constraints were considered when performing trade studies to determine a baseline trajectory included:

- Constrain launch date to be between January 1, 2030 and December 31, 2034.
- Required minimum launch mass = 1000 kg.



- Minimum mission lifetime on the surface of Mars = 180 sols. This in turn places a constraint on the arrival L_s : $-10^\circ \leq L_s \leq 97^\circ$.
- Maximum entry interface speed with respect to a Mars-fixed reference frame = 6.75 km/s. Entry interface would occur at a distance of 3522.2 km from the center of Mars. The spacecraft's flight path angle at entry interface would be constrained to -12.5° .

The trajectory selected for this study would enable landing on October 30, 2032 at $L_s=73$ (Figure B3-25). However, this trajectory has a long transfer time of 841 days and a very high C3 (44.87 to 47.86), so trajectory searches should be refined. Table B3-10 provides the launch window and conditions. Candidate trajectory details are provided in Table B3-11. There are no deterministic DSMs. Heliocentric and Mars-centric views of the transfer trajectories are shown in Figure B3-26.

Table B3-10: Mars Geochronology mission launch window dates and launch and arrival conditions.

	Open	Middle	Close
Launch date	7/12/2030	7/22/2030	8/1/2030
C3 (km^2/s^2)	47.86	44.87	46.16
DLA (deg)	12.51	10.08	5.83
Arrival date	10/30/2032	10/30/2032	10/30/2032
Velocity wrt Mars (km/s)	5.406	5.596	6.08
L_s (deg)	50.57	63.13	71.85

Table B3-11: Mars candidate baseline trajectory details.

Launch Opportunity	2030 Jul 12 - 2030 Aug 1 (21 days)
Max launch C3 across opportunity (km^2/s^2)	47.86
Max DLA across opportunity (deg)	12.51
Falcon Heavy Recovery launch mass at max launch C3 across opportunity (kg)	1170
Mars arrival date	2032 Oct 30
Arrival solar longitude (deg)	73.3
Max entry interface speed wrt Mars-fixed frame across opportunity (km/s)	6.08

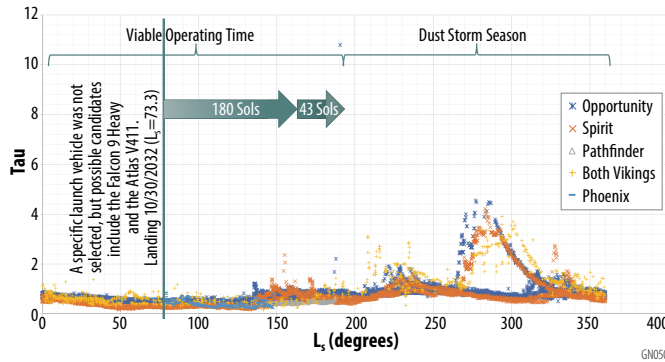


Figure B3-25: Mars Geochronology lander would arrive on October 30, 2032 at $L_s=73.3$.

1.4.3 Entry, Descent, and Landing

The team used a simple exponential Mars atmospheric model to model aerodynamic drag in Mars' atmosphere. The spacecraft drag coefficient (C_d) was held constant at 1.7, and the spacecraft drag area was held constant at 5.515 m^2 . The desired latitude and longitude were targeted at an altitude of 15 km above the surface of Mars, at which point it was assumed that additional means (e.g., a parachute) would be used to further arrest the spacecraft's momentum. The phases of entry, descent, and landing for the Geochronology mission are shown in Figure B3-27.

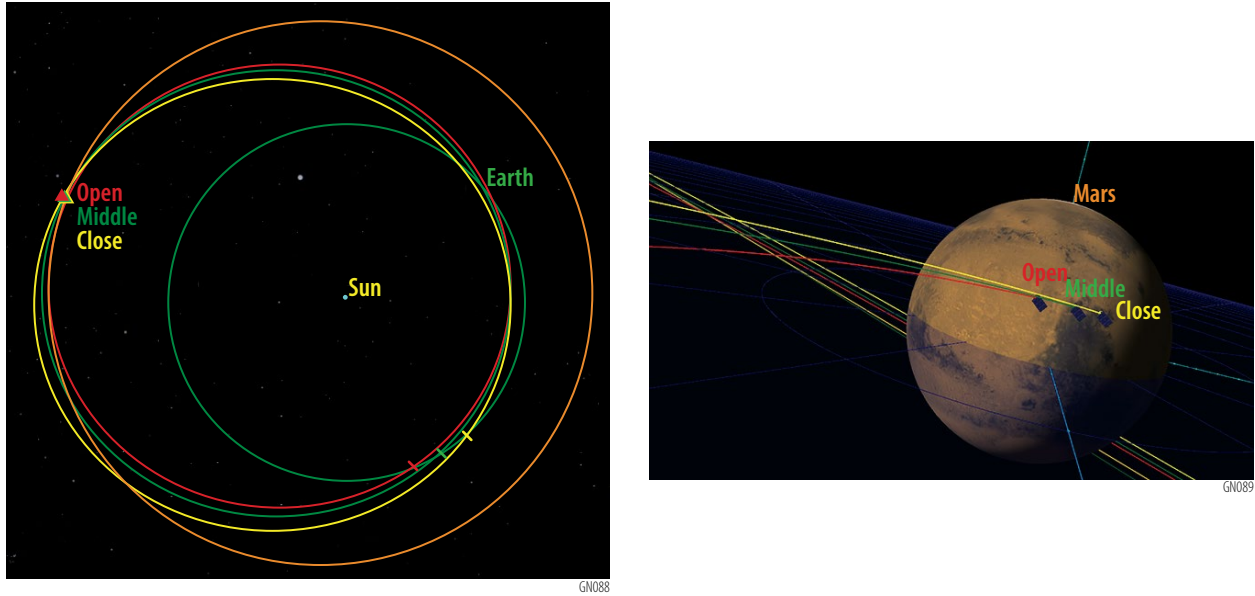


Figure B3-26: Heliocentric (left) and Mars-centric (right) views of the open/middle/close of trajectories for the Geochronology lander.

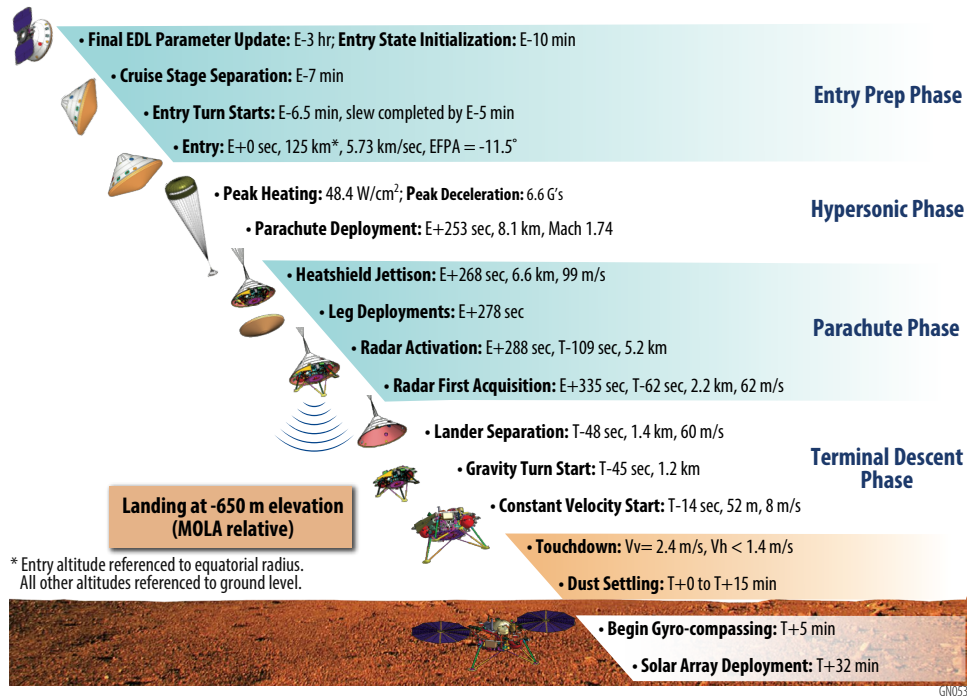


Figure B3-27: Mars Geochronology mission entry, descent and landing at Mars.

1.4.4 Surface Operations

The Mars payload is identical to the Moon and Vesta concepts with the addition of vacuum pumps integrated into the CDEX and KARLE instruments and a vacuum chamber added to CDEX (**Table 2 in Main Report**). The pumps would evacuate Martian atmosphere from the sample chambers prior to and during the laser ablation and gas analysis processes.

The lander design would provide ~700 W-hr/sol for payload operations, which would pace payload use during Mars surface operations. The Geochronology sequence has the ability to pause and restart



at nearly any point, so the process used to analyze a single sample would be distributed over ~4 sols. For the first several samples, full data would be downlinked and examined before retrieving the next sample from the Triage station to ensure that the instruments were working properly, the sample analysis was understood, and the results interpretable in the context of the Science Goals. Later in the mission, a summary or subset of data might be considered for downlink and review, which could increase the pace of operations. This was assumed in the data and power profile (**Figure 19** in the **Main Report**), where sample cadence would increase after analysis of sample 6. Context imaging would be divided over ~16 sols to ensure consistent lighting conditions, though there would be flexibility in this pacing. Assuming 200 Mb/sol downlink capacity, it would take ~14 sols to downlink all the data generated from a single sample analysis. The full 20-sample science operations would be complete at Sol ~340 and all data downlinked by Sol 390.

1.4.5 Subsystem Details

1.4.5.1 Structure

Figure 17 in the **Main Report** shows the Geochronology lander stowed in the heat shield. To accommodate the increased mass of the Geochronology payload relative to Phoenix or Insight, the deck and aeroshell would need to be scaled up. Scaling up the aeroshell and launch mass would cause mass increases in all primary structures and a size increase for the aeroshell. **Table B3-12** shows the mass properties for the Mars Geochronology lander.

Table B3-12: Mass properties for the Mars Geochronology lander.

	CBE	Cont %	MEV	MPV	Margin %
C&DH	13.2	5.0%	13.9	14.5	4.3%
EPS	81.4	4.9%	85.4	91.5	7.1%
Harness	40.0	6.8%	42.7	46.5	8.8%
Telecom	23.1	5.4%	24.3	25.5	4.8%
GN&C	23.2	5.0%	24.4	25.8	5.9%
Structures	332.4	6.5%	354.2	387.3	9.3%
Mechanisms	25.7	6.3%	27.3	29.6	8.4%
Propulsion	68.6	6.2%	72.9	79	8.3%
Thermal	21.3	5.4%	22.4	24.6	9.7%
Ballast	6.1	6.3%	6.5	6.8	5.0%
Spacecraft	635.1	6.1%	674.0	731.1	8.5%
Payload	138.1	23.1%	170.0	180	5.9%
Dry	773.1	9.2%	844.0	911.1	7.9%
Lander Fuel	85	0.0%	85	85	0.0%
Lander Helium	0.9	0.0%	0.9	0.9	0.0%
Launch Total	859.0	8.3%	929.9	997.0	7.2%
AV411 Capability (C3=47.85)				1130	

The launch allocation for Falcon Heavy-R is currently 997 kg. Future iterations of the launch vehicle performance may increase launch allocation to 1130-1170 kg, which would provide additional launch margin (though possibly at higher cost). A future iteration could take advantage of the LV capability at a very modest CBE mass increase. Additional design iterations could better allocate the launch vehicle capability to achieve a launch margin of 21.5% as shown in **Table B3-13**.

1.4.5.2 Power

The design would provide ~700 W-hr/sol available for payload operations. However, experience with Phoenix and InSight might predict that much more energy would be available earlier in the mission. **Figure B3-28** shows the expected energy availability throughout the mission lifetime.



Table B3-13: Possible future mass properties for the Mars Geochronology lander using updated launch vehicle performance.

	CBE	Cont %	MEV	MPV	Margin %
C&DH	13.2	5.0%	13.9	14.5	4.3%
EPS	81.4	4.9%	85.4	91.5	7.1%
Harness	40.0	6.8%	42.7	46.5	8.8%
Telecom	23.1	5.4%	24.3	25.5	4.8%
GN&C	23.2	5.0%	24.4	25.8	5.9%
Structures	332.4	6.5%	354.2	387.3	9.3%
Mechanisms	25.7	6.3%	27.3	29.6	8.4%
Propulsion	68.6	6.2%	72.9	79	8.3%
Thermal	21.3	5.4%	22.4	24.6	9.7%
Ballast	6.1	6.3%	6.5	6.8	5.0%
Spacecraft	635.1	6.1%	674.0	731.1	8.5%
Payload	138.1	23.1%	170.0	180	5.9%
Dry	773.1	9.2%	844.0	1044.1	23.7%
Lander Fuel	85	0.0%	85	85	0.0%
Lander Helium	0.9	0.0%	0.9	0.9	0.0%
Launch Total	859.0	8.3%	929.9	1130.0	21.5%
AV411 Capability (C3=47.85)				1130	

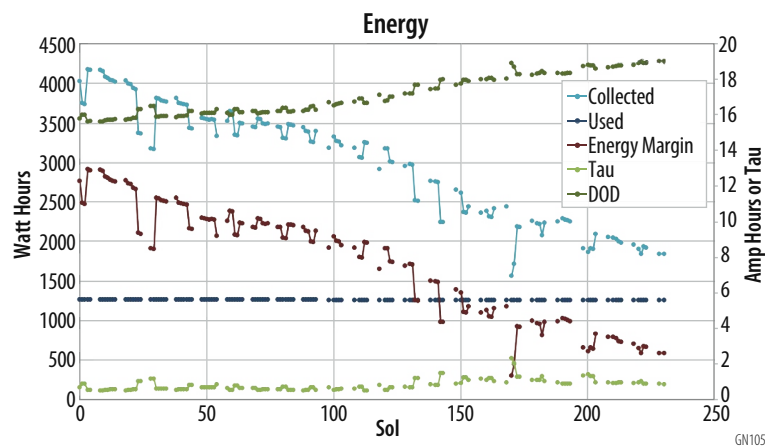


Figure B3-28: Expected energy early in the Mars Geochronology mission.

1.4.5.3 Communications

For orbital assets at equatorial latitudes it is unknown how much communications relay capacity could be available for this mission. A conservative estimate using the Mars Relay User’s Guide might be 50 Mbits/sol. At a downlink rate of 50 Mbits/sol, it would take ~1500 sols to complete all science data downlink. However, flight missions have had much better downlink capacity (**Figure B3-29, Table B3-14**). Therefore, the team baselined 200 MB/sol downlink, which is in line with what Insight has been able to downlink. At this rate, the full 20-sample science operations would be complete at Sol 340 and all data downlinked by Sol 390 (assuming no dust storm interruptions).

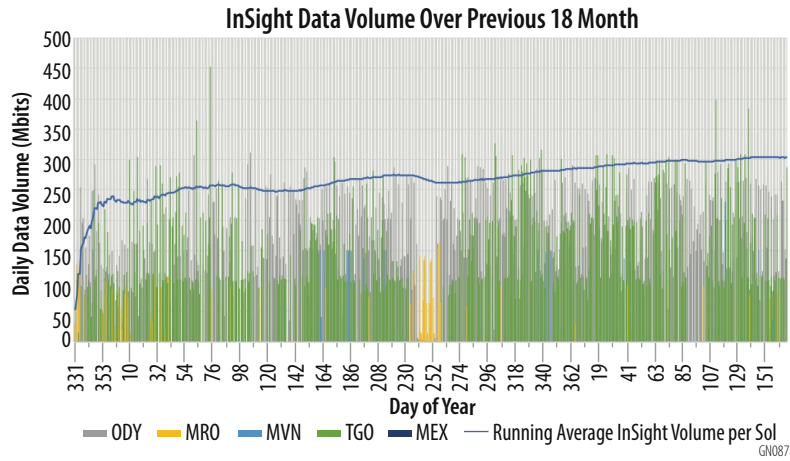


Figure B3-29: InSight daily downlink data volume over its mission lifetime.

Table B3-14: Daily average relay capacity volume (Mbits) for Mars orbiters.

	Daily Average Volume	Daily Average Passes
ODY	72.1	1.9
MRO	72.1	1.1
MVN	132.1	1.1
TOG	163.8	1.3



Appendix B4 –Detailed Cost and Schedule

Mission Schedules

Developing a mission implementation schedule identifying detailed development activities and flows within all WBS's, especially for the WBS 5 and 6 elements, was outside the scope of this study. To determine the feasibility of the Geochronology mission concepts as compatible with a typical New Frontiers mission, we generated a template Geochronology mission schedule drawn from New Frontiers mission data sets in CADRe. This template schedule reflects the average mission Phase B-D durations of prior New Frontiers missions and the typical average locations for standard mission level milestone reviews. This template schedule incorporates the schedule data from Phoenix and InSight mission system developments. We used this template schedule to evaluate hardware development times for WBS 5 and 6, as these elements drive the schedule duration.

The Geochronology instrument developers, all of whom have experience in developing flight systems, confirmed the feasibility of developing their respective instruments inside the mission phase and milestone review framework of the template schedule. The summary development schedule generated by the GSFC Mission Design Laboratory for the lunar lander, which is very similar to the Vesta lander, also showed that the schedule would fit within the template schedule. The Mars lander in this study is based on the Phoenix and InSight missions and would also have a development schedule commensurate with the template schedule.

The Phase B-D durations, milestone reviews and general schedule flow of the Geochronology template schedule would be compatible with all Geochronology missions studied. What would vary among the missions is the ATP/Phase B start dates, the Launch Readiness Dates (LRD) and constraints, and Phase E elements and durations. Launch window constraints for all missions are described in **Appendix B3**. The high-level summary schedule and mission phase durations for all Geochronology missions studied is shown in **Schedule Foldout 1**.

The lunar and Vesta missions both would have Phase E science operations lasting one terrestrial year (including margin). The Vesta mission Phase E would include a 49 month 7 day cruise phase and 6 month orbital survey phase. To minimize the delta-V and cruise phase for arrival at Vesta, the Vesta mission LRD would be 8 months later than the lunar mission LRD. To keep the hardware development durations the same, the Vesta mission would have a corresponding 8 month later ATP/Phase B start date. For the Mars Geochronology mission, Phase E science operations would take 450 sols, or 464 terrestrial days (including margin). The Mars mission Phase E would include a 27 month 18 day cruise phase before a direct descent to the Martian surface. To minimize the delta-V to arrive at Mars, and maximize mission operational time before the onset of seasonal dust storms, the Mars mission LRD would be one month later than the lunar mission. To keep the hardware development durations the same, the Mars mission ATP/Phase B start date would likewise be one month delayed relative to the Lunar mission.

The Geochronology mission schedules would meet NASA requirements for funded schedule reserves and would fit well within history of New Frontiers mission schedule execution. If a Geochronology mission were to be proposed as a New Frontiers mission, more detailed schedules would need to be developed and optimized per specifics of the payload and lander developments.

To maintain a schedule as shown in **Schedule Foldout 1**, the proposing mission team(s), during the Step 2 Phase A and early Phase B, would be challenged to develop WBS 6 requirements and contract documentation, so as to have in place/award a contract for WBS 6 (Lander or EDL) by the ATP date shown. Mission proposing teams would also be challenged during the Phase A time frame to reduce risks identified for the specific mission.

Costing Methodology and Basis of Estimates

A variety of costing methods were used to develop the Phase B-D costs for the Geochronology missions studied, which are shown in **Table B4-1**. The Geochronology team developed the mission cost estimates by first creating a Work Breakdown Structure (WBS) compliant with NPR 7120.5E. A few WBS elements would be specific to the Mars Geochronology mission. All cost estimates were modeled



assuming hardware components would be at TRL 6. No special facilities or facility modifications were assumed. Appropriate engineering development units and flight spares were incorporated into the cost models; spares were not modeled for common vendor items such as star cameras, sun sensors, IMU, SDST, etc.

Table B4-1: Geochronology missions costing methodology.

WBS Elements		Costing Methodology
1	Project Management	NF Avg. % Wrap of Sum of WBS 5&6
2	Mission Systems Engineering	NF Avg. % Wrap of Sum of WBS 5&6
3	Safety and Mission Assurance	NF Avg. % Wrap of Sum of WBS 5&6
4	Science	NF Avg. % Wrap of Sum of WBS 5&6
5	Payload Suite	
5.5	Instruments	
5.5.1	CDEX	
5.5.1.1	CDEX Instrument	SEER-H Cost Modeled; 50% Confidence Level
5.5.1.2	Postgrind Imager	ROM Estimate for Camera ~ MAHLI Costs
5.5.1.3	Grinding Station	ROM Estimate from Honeybee
5.5.1.4	Vacuum Pump and Chamber (Mars Mission Only)	ROM Estimate from Co-I; TRL 8, 9
5.5.2	KArLE	
5.5.2.1	KArLE Instrument	NICM Cost Modeled; 50% Confidence Level
5.5.2.2	Vacuum Pump (Mars Mission Only)	Estimate from SAM instrument Vendor
5.5.3	ICPMS	NICM Cost Modeled; 50% Confidence Level
5.5.4	UCIS	NICM Cost Modeled; 50% Confidence Level
5.5.5	Panoramic Cameras and Microimager	ROM Estimate from Co-I; TRL 8, 9
5.6	Sample Handling Systems	ROM Estimate From Honeybee Inc.
6	Landing Systems	Moon, Vesta: NICM Cost Modeled: 50% Confidence Level Mars: Lockheed Martin Proprietary Parametric Cost Model
7	Mission Operations	ROM estimate from MDL Mission Operations Lead
9	Ground Systems	NF Avg. % Wrap of Sum of WBS 5&6
10	Systems I&T	NF Avg. % Wrap of Sum of WBS 5&6

Payload WBS 5

Table B4-2 and shows the Phase B-D costs of the Lunar, Vesta and Mars Geochronology mission WBS 5 payload elements.

Instrument cost modeling for KArLE (WBS 5.5.2), ICPMS (WBS 5.5.3), and UCIS (WBS 5.5.4) was performed by the GSFC Cost Estimating, Modeling & Analysis (CEMA) Office using the using the NASA Instrument Cost Model (NICM). The Geochronology team provided the CEMA Office with the high level technical parameters and schedule data for each of these 3 instruments, as inputs to the NICM. Modeling was performed assuming all hardware is at TRL 6 maturity and that the KArLE and ICPMS systems would be efficiently packaged, using a single carousel, laser ablation system, and mass spectrometer between both instruments. The NICM model produces a probabilistic cost result, a Cumulative Distribution Function (CDF), more commonly referred to as an S-curve, which accounts for uncertainty in the input parameters as well as error terms associated with cost estimating relationships. The CDF defines confidence levels of 30%, 50%, 70% etc. as a function of costs. For the KArLE, ICPMS and UCIS instruments, the 50% confidence costs were used in **Table B4-2**.

The remaining payload elements have had prior engineering formulation and/or flight heritage, so cost estimates for these elements were derived from rough order-of-magnitude (ROM) estimates provided by their respective supplier. The CDEX instrument (WBS 5.5.1) has been through prior Phase A formulation activities, proposed against a NASA Announcement of Opportunity, and evaluated by a Technical, Management, Cost, and Other (TMCO) review panel. CDEX instrument costs are based on a System Evaluation & Estimation of Resources - Hardware (SEER-H) model results with reserves added. The cameras have high TRL and reliable cost and design heritage, giving confidence in their



ROM costs. The sampling handling system components either have flight heritage, or have been proposed and vetted by a TMCO review panel and are now in development on NASA missions, giving them sufficient design and cost heritage to use their ROM estimates.

Lander Systems WBS 6

Table B4-2: Lunar, Vesta, and Mars payload costs.

WBS Element		Costs \$M FY 2025	
		Lunar & Vesta	Mars
5	Payload		
5.5	Instruments		
5.5.1	CDEX		
5.5.1.1	CDEX Instrument	\$73	\$73
5.5.1.2	Postgrind imager	\$3	\$3
5.5.1.3	Grinding station	\$9	\$9
5.5.1.4	Vacuum pump and chamber		\$3
5.5.2	KArLE		
5.5.2.1	KArLE instrument ¹	\$57	\$57
5.5.2.2	Vacuum pump		\$1
5.5.3	ICPMS ²	\$39	\$39
5.5.4	UCIS	\$18	\$18
5.5.5	Panoramic cameras and Microimager	\$19	\$19
5.6	Sample handling system	\$13	\$13
	Subtotal	\$232	\$237
	50% Reserves	\$116	\$118
	Payload Total	\$348	\$355
¹ Not including the mass spectrometer, which is carried in the ICPMS allocation			
² Not including the laser ablation system, which is included in the KArLE allocation			

The GSFC CEMA Office used SEER-H parametric cost model to estimate costs for the Lunar and Vesta missions landing systems (WBS 6). The Geochronology team, in partnership with the GSFC Mission Design Lab (MDL), generated a lander systems Master Equipment List (MEL) and provided this and schedule data to the CEMA Office modelers as input into the SEER-H model. The SEER-H model produces a probabilistic cost result, a Cumulative Distribution Function (CDF). For the lunar and Vesta Landers, the 50% confidence costs were used. **Table B4-3** shows the Phase B-D costs of the individual Lunar and Vesta Geochronology mission WBS 6 Lander Systems.

The WBS 6 costs for the Mars lander, including the EDL system, for Phases B/C/D were estimated by Lockheed Martin using a proprietary parametric used and refined over decades for planetary mission cost modeling. A MEL was developed as input to the cost model. The Lockheed Martin parametric cost estimating technique for the spacecraft is based on a mature parametric estimating process that has been used since the inception of PI-led planetary missions and continuously refined and calibrated with actual costs from Lockheed’s planetary flight programs.

Phase B-D costs for the Mars Geochronology missions lander would be \$249M in \$FY2025. Per stipulations in the agreement between GSFC and Lockheed Martin, detailed breakdown of costs within WBS 6 and WBS 7, 9 & 10 was not provided. However, since this estimate also includes EDL systems costs in WBS 7, 9, & 10; some double booking of costs in these WBS elements is shown in **Section 7 Table 14**, adding reserve above the 50% required by the study report guidelines.

Non-Flight Hardware WBS 1-4, 9 & 10

For the non-hardware WBS elements, applying a wrap rate to the sum of WBS 5&6 is a common practice for the basis of estimation prior to entering the Pre-Phase A of a mission lifecycle. Wrap rates were used to calculate the cost of WBS 1-4, 9 & 10, Project Management, Mission Systems Engineering, Safety & Mission Assurance, Ground System and System I&T. Average wrap rates were determined from prior New Frontiers mission cost data (**Table B4-4**).



Phase E

Table B4-5 shows the Phase E costs for the Geochronology Lunar, Vesta, and Mars missions studied.

Table B4-3: Lunar and Vesta Geochronology lander subsystems costs.

WBS Elements		Costs \$M FY 2025	
		Lunar	Vesta
6	Lander Systems		
6.1	Attitude control	\$17	\$19
6.2	Avionics	\$21	\$20
6.3	Communications	\$28	\$31
6.4	Electrical power	\$25	\$33
6.5	Mechanisms	\$11	\$16
6.6	Structure	\$63	\$58
6.7	Propulsion	\$37	\$35
6.8	Thermal	\$4	\$4
6.9	Management, systems engineering, assembly, integration, and testing	\$44	\$47
6.10	Flight spares & engineering test units	\$23	\$27
6.11	Ground support equipment	\$12	\$13
6.12	Environmental testing	\$12	\$13
6.13	Software		
6.13.1	FPGA development	\$2	\$2
6.13.2	Flight software	\$25	\$27
6.13.3	Flight software testbed	\$1	\$1
Subtotal		\$325	\$348
50% Reserves		\$163	\$174
Lander Systems Total		\$488	\$522

Table B4-4: New Frontiers wrap rates.

% of Flight (WBS 5.0 & 6.0) Cost		
WBS #	WBS	Average
1	Project Management	7.9%
2	Systems Engineering	4.7%
3	Safety & Mission Assurance	4.1%
4	Science/Technology	3.5%
5	Payload	28.0%
6	Spacecraft	72.0%
7	Mission Operations	4.2%
8	LV Services	61.2%
9	Ground Operations	7.1%
10	Systems I&T	5.9%
11	E&PO	0.4%

The GSFC CEMA Office used the Mission Operations Cost Estimating Tool (MOCET) to model the Phase E costs for the Geochronology Missions. The MOCET model produces a CDR-level CDF or “S-curve.” For each mission, the 50% confidence costs were used and an additional 25% reserves added. For Geochronology mission Phase E surface operations, the science team is estimated to be 15 FTE: the PI, Deputy PI, and Project Scientist each at 0.5FTE and a total of 3 FTE involved in the Science Operations Center (SOC).



Table B4-5: Geochronology Lunar, Vesta, Mars missions Phase E costs.

Mission	Phase E Cruise	Phase E Orbit Survey	Phase E Surface Science Operations	Cost \$M FY 2025
Lunar	5 days	0 mo.	1 year	\$80
Vesta	49 mo. 7 days	6 mo.	1 year	\$252
Mars	27 mo. 18 days	0 mo.	1.3 year	\$160



Appendix C – Special Technical Analysis – Mobility Trades

Mobility was one of the driving trades in the Geochronology mission study. Enabling global access to sites thousands of km apart would be a significant architectural breakthrough, not only for geochronology, but for many other kinds of science. The importance of measuring in situ ages across widely-separated locations, the existence of extensive well-characterized target terrains, and the availability of flight-heritage payload components would make a hopper a scientifically compelling and architecturally attractive opportunity for an in situ dating mission. To meet the mission requirement of “Conduct sample analysis at two geographically different sites hundreds to thousands of km apart” we investigated a lunar lander that could land at one site and then hop to a second site, as per **Figure C-1**. We investigated pairs of landing sites in Mare Crisium, Mare Nectaris, and Procellarum basin (see more information on sites in **Appendix B1**), approximately 1200 km apart, to perform a trade of hopping distance vs required landing mass, including propellant mass, for the hop with a 1,237.8 kg dry-mass lander.

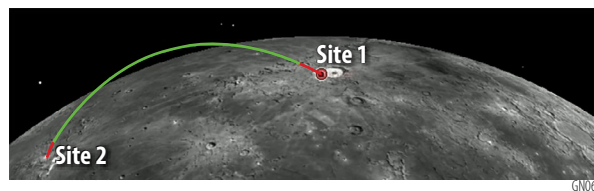


Figure C-1: Moon Hop transfer trajectory (distance 900 km).

The trade study was performed to understand two main factors: a) what wet mass would be required for the first landing (prior to the hop), and b) how much propellant would be needed to allow for a hop. This can be translated to how much launch mass would be needed to land on the moon and perform a hop. The spacecraft dry mass would be greater than 1237.8 kg MEV.

Four alternatives for reaching the first landing site were evaluated:

- Direct landing
 - Solid propellant used for orbit transfer
 - Liquid propellant for Entry, Descent, and Landing (EDL)
 - Liquid propellant used to hop to second site
- Direct landing
 - Liquid propellant used for orbit transfer
 - Liquid propellant for EDL
 - Liquid propellant used to hop to second site
- Orbit insertion to a circular lunar orbit with 50 km altitude prior to performing EDL
 - Liquid propellant used for orbit transfer
 - Liquid propellant for EDL
 - Liquid propellant used to hop to second site
- Low-energy transfer trajectory prior to performing EDL
 - Liquid propellant used for orbit transfer
 - Liquid propellant for EDL
 - Liquid propellant used to hop to second site

The liquid propulsion system was assumed to produce 4000 N thrust at an I_{sp} of 293 s. Future iterations of the study may consider an engine development that would improve the I_{sp} to 315 s. Low-energy capture was discarded due to a project-level decision. The three remaining alternatives were analyzed, and the results are given in **Table C-1**, **Table C-2**, and **Table C-3**. Solutions were generated by constraining the minimal wet mass (after the hop) and calculation the fuel-optimal launch mass solution. This results in different launch masses, but similar final masses.



Table C-1: Additional lunar transfer concepts evaluated in trade study.

Landing method		Direct	Direct	Direct	Direct	Orbit		Orbit	
Solid engine		-	Star48	Star 63D	-	-		-	
Liquid engine		4kN, 293s	4kN, 293s	4kN, 293s	4 x 4kN, 293s	4kN, 293s		4 x 4kN, 293s	
Launch Mass		7237.8kg (fuel: 6000kg)	7381kg (fuel: 6000kg) (Star48: 144kg)	6287kg (fuel: 4800kg) (Star63D: 249kg)	5254kg (fuel: 3600kg)	4738kg (fuel: 3500kg)		4654.9kg (fuel: 3000kg)	
Solid engine	Delta V		1110m/s	2020m/s					
	Fuel		2430kg	3250kg					
	Burn time		88s	106s					
Liquid						LOI	Landing	LOI	Landing
	Delta V	4790m/s	3608m/s	1932m/s	3020m/s	777m/s	2776m/s	774m/s	1907m/s
	Fuel	5871kg	3438kg	1364kg	3418kg	1123kg	2117kg	1100kg	1724kg
	Burn time	4270s	2607s	1102s	725s	807s	1654s	197s	357s
Landing Mass		1367kg	1370kg	1423kg	1837kg	1376kg		1831kg	

Table C-2: Additional solid propellants evaluated in trade study.

	Average Thrust (N)	I _{sp} (s)	Wet Mass (kg)	Dry Mass (kg)	Fuel Mass (kg)
Star 48	77176.6	283	2547	144	2430
Star 63D	84739	283	3495	245	3250
Star 75	200170	288	8068	565	7503

Table C-3: Direct transfer.

		Direct	Direct	Direct	Orbit
Solid engine		Star 63D	Star75	Star75	Star 63D
Liquid engine		24kN, 293s	24kN, 293s	24kN, 315s	24kN, 315s
Launch mass		13000kg	13000kg	12500kg	11000kg
Solid engine	Delta V	798m/s	2576m/s	2577m/s	780m/s
	Fuel	3250kg	7481kg	7481kg	2696kg
	Burn time	106s	111s	111s	88s
Liquid	Delta V	2424m/s	293m/s	294m/s	1963m/s
	Fuel	5417kg	432kg	404kg	3777kg
	Burn time	756s	52s	53s	535s
Landing mass		4087kg	4038kg	4053kg	4255kg

As seen in these tables, the largest landing mass results from a direct landing using the Star 63D solid engine. However, going into orbit prior to landing results in the smallest fuel mass requirement.

The feasibility of hopping to a second site was evaluated based on the landing mass values produced by the various lunar transfer concepts (Table C-4). For all transfer concepts, the landing mass was found to be greater than the requirement of 1237.8 kg (MEV). However, for all lunar transfer concepts, the fuel mass required to perform a hop of hundreds or thousands of km was found to be significantly greater than the landing mass and in excess of the MEV requirement (*i.e.*, the mass that could be used for fuel for a hop).

Table C-4: Spacecraft mass requirement for hop.

Hop distance (km)	I _{sp} 315s		I _{sp} 293s	
	Landed mass prior to hop (kg)	Propellant required for hop (kg)	Landed mass prior to hop (kg)	Propellant required for hop (kg)
300	3060	1210	3160	1310
660	3650	1800	3840	1990
900	4000	2150	4250	2400
1200	4380	2530	4680	2830



We used the landed mass at the second site to determine the propellant required to hop from the first site and then used that total to determine the total propellant mass needed. This resulted in large propellant masses and unrealistic burn times for the baselined lander liquid engines. We iterated our solution with shorter hop distances. As shown in **Figure C-2** and illustrated in **Table C-4**, a hop of 300 km or more would require a landed mass in excess of 3000 kg, which is more than twice the mass landed by most of the scenarios described in **Table C-3**.

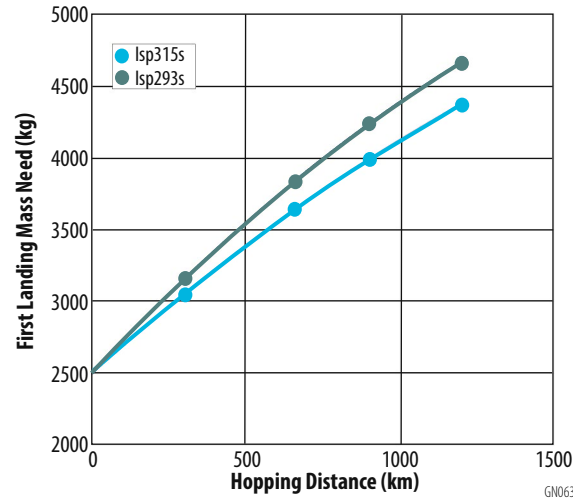


Figure C-2: First landing mass vs. hopping distance.

We investigated using large solid propellant motors such as the Star 63D and Star 75 and were able to get a solution to close with the Star 75. The total launch mass of this solution was 13,0998 kg. Due to the long lunar night the concept would require a Next Generation Radioisotope Thermoelectric Generator (NGRTG) to provide heat to keep the propellant for the hop warm, but cooling for the NGRTG was an issue at lunar noon at the low latitudes of interest. When we evaluated the cost of this solution we found that the Star 75 would need development costs as it was only used as a test motor on the ground and has never flown. This development cost with the added costs of using the NGRTG pushed the total mission cost above the New Frontiers cap of \$1.1B FY25.

Though lunar hoppers have been considered by many teams, the Moon is a marginal case for hopping. For this mission study, the combination of a heavy payload and a long required hop distance meant that we didn't get a design to close. Lunar hopper missions may be feasible for missions with smaller payloads (10s of kg) and shorter hops (<1km). The team descoped the lunar mission in this study to be a single site lander, but to maintain compelling science at a single site, the lander would conduct operations on two lithologies of interest (20 samples). However, for smaller bodies like Vesta (which also has a less severe day/night cycle), both the fuel needed and the ability to keep it warm are less demanding, so we were able to develop a Vesta hopper to reach both sites of interest.

Mars, with its higher gravity and a thicker atmosphere, would be a worse case for hopping than the Moon. However, Mars has been the target of many rover missions, which we surveyed. Small (MER-class) rovers carry on the order of a 5 kg payload, which is insufficient to meet our sample acquisition and analysis needs. The payload size and power is more consistent with the Curiosity rover or long range lunar geology explorers. Curiosity/Perseverance-class rovers could carry on the order of 100 kg of payload, but their Flagship-class costs put them outside of our study envelope. We made a similar decision for the Mars architecture to baseline a single site but to conduct operations on two lithologies of interest (20 samples).



Appendix D – References

- Allton J. H. (1978) *The Apollo 11 Drive Tubes*. https://curator.jsc.nasa.gov/lunar/catalogs/other/apollo11_drive_tubes.pdf; last accessed.
- Anderson F. S., Levine J., and Whitaker T. J. (2015a) Dating the Martian meteorite Zagami by the ^{87}Rb - ^{87}Sr isochron method with a prototype in situ resonance ionization mass spectrometer. *Rapid Communications in Mass Spectrometry* **29**, 191-204.
- Anderson F. S., Levine J., and Whitaker T. J. (2015b) Rb-Sr resonance ionization geochronology of the Duluth Gabbro: A proof of concept for in situ dating on the Moon. *Rapid Communications in Mass Spectrometry* **29**, 1457-1464.
- Arevalo Jr. R., Farcy B., Benna M., Taghioskouli M., William McDonough (1), Brinckerhoff W., Briois C., Thirkell L., Colin F., Sellie L., Makarov A., Yu A., Fahey M., Southard A., Grubisic A., Danell R., and Gundersen C. (2019) Planetary Applications For In Situ Laser Ablation Processing Coupled With Mass Spectrometry. *EGU General Assembly* 21, #EGU2019-17077.
- Arvidson R. E., Bonitz R. G., Robinson M. L., Carsten J. L., Volpe R. A., Trebi-Ollennu A., Mellon M. T., Chu P. C., Davis K. R., Wilson J. J., Shaw A. S., Greenberger R. N., Siebach K. L., Stein T. C., Cull S. C., Goetz W., Morris R. V., Ming D. W., Keller H. U., Lemmon M. T., Sizemore H. G., and Mehta M. (2009) Results from the Mars Phoenix Lander Robotic Arm experiment. *Journal of Geophysical Research: Planets* **114**.
- Bandfield J. L., Ghent R. R., Vasavada A. R., Paige D. A., Lawrence S. J., and Robinson M. S. (2011) Lunar surface rock abundance and regolith fines temperatures derived from LRO Diviner Radiometer data. *Journal of Geophysical Research (Planets)* **116**.
- Beatty D. W., Grady M. M., McSween H. Y., Sefton-Nash E., Carrier B. L., Altieri F., Amelin Y., Ammannito E., Anand M., Benning L. G., Bishop J. L., Borg L. E., Boucher D., Brucato J. R., Busemann H., Campbell K. A., Czaja A. D., Debaille V., Des Marais D. J., Dixon M., Ehlmann B. L., Farmer J. D., Fernandez-Remolar D. C., Filiberto J., Fogarty J., Glavin D. P., Goreva Y. S., Hallis L. J., Harrington A. D., Hausrath E. M., Herd C. D. K., Horgan B., Humayun M., Kleine T., Kleinhenz J., Mackelprang R., Mangold N., Mayhew L. E., McCoy J. T., McCubbin F. M., McLennan S. M., Moser D. E., Moynier F., Mustard J. F., Niles P. B., Ori G. G., Raulin F., Rettberg P., Rucker M. A., Schmitz N., Schwenzer S. P., Sephton M. A., Shaheen R., Sharp Z. D., Shuster D. L., Siljeström S., Smith C. L., Spry J. A., Steele A., Swindle T. D., ten Kate I. L., Tosca N. J., Usui T., Van Kranendonk M. J., Wadhwa M., Weiss B. P., Werner S. C., Westall F., Wheeler R. M., Zipfel J., and Zorzano M. P. (2019) The potential science and engineering value of samples delivered to Earth by Mars sample return. *Meteoritics & Planetary Science* **54**, S3-S152.
- Bibring J. P., Langevin Y., Mustard J. F., Poulet F., Arvidson R., Gendrin A., Gondet B., Mangold N., Pinet P., Forget F., Berthe M., Bibring J. P., Gendrin A., Gomez C., Gondet B., Jouglet D., Poulet F., Soufflot A., Vincendon M., Combes M., Drossart P., Encrenaz T., Fouchet T., Merchiorri R., Belluci G., Altieri F., Formisano V., Capaccioni F., Cerroni P., Coradini A., Fonti S., Korabely O., Kottsov V., Ignatiev N., Moroz V., Titov D., Zasova L., Loiseau D., Mangold N., Pinet P., Doute S., Schmitt B., Sotin C., Hauber E., Hoffmann H., Jaumann R., Keller U., Arvidson R., Mustard J. F., Duxbury T., Forget F., and Neukum G. (2006) Global mineralogical and aqueous mars history derived from OMEGA/Mars Express data. *Science* **312**, 400-4.
- Bishop J. et al. (2017) Marwth Vallis: Detailed Description of Mineralogy and Stratigraphy. https://mars-next.jpl.nasa.gov/documents/2017/Thursday%20Afternoon/18.%20Bishop_Mawrth_20170209.pdf; last accessed June 8.



- Bishop J. L., Dobrea E. Z., McKeown N. K., Parente M., Ehlmann B. L., Michalski J. R., Milliken R. E., Poulet F., Swayze G. A., Mustard J. F., Murchie S. L., and Bibring J. P. (2008) Phyllosilicate diversity and past aqueous activity revealed at Mawrth Vallis, Mars. *Science* **321**, 830-3.
- Bogard D. D. (2011) K-Ar ages of meteorites: Clues to parent-body thermal histories. *Chemie der Erde* **71**, 207-226.
- Bottke W. F. and Norman M. D. (2017) The Late Heavy Bombardment. *Annual Review of Earth and Planetary Sciences* **45**, 619-647.
- Braden S. E., Stopar J. D., Robinson M. S., Lawrence S. J., van der Bogert C. H., and Hiesinger H. (2014) Evidence for basaltic volcanism on the Moon within the past 100 million years. *Nature Geoscience* **7**, 787.
- Bramble M. S., Mustard J. F., and Salvatore M. R. (2017) The geological history of Northeast Syrtis Major, Mars. *Icarus* **293**, 66-93.
- Carrier W. D. (1973) Lunar soil grain size distribution. *The moon* **6**, 250-263.
- Carson J. M., Johnson A. E., Hines G. D., Johnson W., Anderson F. S., Lawrence S., Lee D. E., Huertas A., Amzajerdian F., Olansen J. B., Devolites J., Harris W. J., Trawny N., Condon G. L., and Nguyen L. (2016) GN&C Subsystem Concept for Safe Precision Landing of the Proposed Lunar MARE Robotic Science Mission. In *AIAA Guidance, Navigation, and Control Conference*. American Institute of Aeronautics and Astronautics.
- Cattani F., Gillot P.-Y., Quidelleur X., Hildenbrand A., Lefèvre J.-C., Boukari C., and Courtade F. (2019) *In-situ* K-Ar dating on Mars based on UV-Laser ablation coupled with a LIBS-QMS system: Development, calibration and application of the KArMars instrument. *Chemical Geology* **506**, 1-16.
- Chapman C. R., Cohen B. A., and Grinspoon D. H. (2007) What are the real constraints on the existence and magnitude of the late heavy bombardment? *Icarus* **189**, 233-245.
- Cho Y. and Cohen B. A. (2018) Dating igneous rocks using the Potassium–Argon Laser Experiment (KArLE) instrument: a case study for ~380 Ma basaltic rocks. *Rapid Communications in Mass Spectrometry* 10.1002/rcm.8214.
- Christensen P. R., Bandfield J. L., Hamilton V. E., Ruff S. W., Kieffer H. H., Titus T. N., Malin M. C., Morris R. V., Lane M. D., and Clark R. L. (2001) Mars Global Surveyor Thermal Emission Spectrometer experiment: investigation description and surface science results. *Journal of Geophysical Research: Planets* **106**, 23823-23871.
- Cintala M. J. and McBride K. M. (1995) Block distributions on the lunar surface: *A comparison between measurements obtained from surface and orbital photography*. NASA Technical Report NASA-TM-104804.
- Cohen B. A. (2013) The Vestan cataclysm: Impact-melt clasts in howardites and the bombardment history of 4 Vesta. *Meteoritics & Planetary Science* **48**, 771-785.
- Cohen B. A., Malespin C. A., Farley K. A., Martin P. E., Cho Y., and Mahaffy P. R. (2019) In Situ Geochronology on Mars and the Development of Future Instrumentation. *Astrobiology* **19**, 1303-1314.
- Cohen B. A., Miller J. S., Li Z.-H., Swindle T. D., and French R. A. (2014) The Potassium-Argon Laser Experiment (KArLE): In Situ Geochronology for Planetary Robotic Missions. *Geostandards and Geoanalytical Research* **38**, 421-439.



- Conrad P. G., Malespin C. A., Franz H. B., Pepin R. O., Trainer M. G., Schwenzer S. P., Atreya S. K., Freissinet C., Jones J. H., Manning H., Owen T., Pavlov A. A., Wiens R. C., Wong M. H., and Mahaffy P. R. (2016) In situ measurement of atmospheric krypton and xenon on Mars with Mars Science Laboratory. *Earth and Planetary Science Letters* **454**, 1-9.
- Cook A. M. and et al. (2016) NIR Spectroscopy and Multi-wavelength imaging for volatile prospecting. *Instruments for Planetary Missions Conference*, #4023.
- Coutts D. S., Matthews W. A., and Hubbard S. M. (2019) Assessment of widely used methods to derive depositional ages from detrital zircon populations. *Geoscience Frontiers* **10**, 1421-1435.
- Dalrymple G. B. and Ryder G. (1996) Argon-40/argon-39 age spectra of Apollo 17 highlands breccia samples by laser step heating and the age of the Serenitatis basin. *Journal of Geophysical Research* **101**, 26,069-26,084.
- Deutsch A. and Stöffler D. (1987) Rb-Sr-analyses of Apollo 16 melt rocks and a new age for the Imbrium basin: Lunar basin chronology and the early heavy bombardment of the moon. *Geochimica et Cosmochimica Acta* **51**, 1951-1964.
- Devismes D., Gillot P.-Y., Lefèvre J.-C., Boukari C., Rocard F., and Chiavassa F. (2016) KArMars: A breadboard model for in situ absolute geochronology based on the K-Ar method using UV-laser induced breakdown spectroscopy and quadrupole mass spectrometry. *Geostandards and Geoanalytical Research* **40**, 517-532.
- Doran P. T., Clifford S. M., Forman S. L., Nyquist L., Papanastassiou D. A., Stewart B. W., Sturchio N. C., Swindle T. D., Cerling T., Kargel J., McDonald G., Nishiizumi K., Poreda R., Rice J. W., and Tanaka K. (2004) Mars chronology: assessing techniques for quantifying surficial processes. *Earth-Science Reviews* **67**, 313-337.
- Draper D. S., Klima R. L., Lawrence S. J., and Denevi B. W. (2019) The Inner Solar System CHRONology (ISOCHRON) Discovery Mission: Returning Samples of the Youngest Lunar Mare Basalts. *Lunar and Planetary Science Conference*, #1110.
- Duke M. B. (2003) Sample return from the lunar South Pole-Aitken Basin. *Advances in Space Research* **31**, 2347-2352.
- Ehlmann B. L., Anderson F. S., Andrews-Hanna J., Catling D. C., Christensen P. R., Cohen B. A., Dressing C. D., Edwards C. S., Elkins-Tanton L. T., Farley K. A., Fassett C. I., Fischer W. W., Fraeman A. A., Golombek M. P., Hamilton V. E., Hayes A. G., Herd C. D. K., Horgan B., Hu R., Jakosky B. M., Johnson J. R., Kasting J. F., Kerber L., Kinch K. M., Kite E. S., Knutson H. A., Lunine J. I., Mahaffy P. R., Mangold N., McCubbin F. M., Mustard J. F., Niles P. B., Quantin-Nataf C., Rice M. S., Stack K. M., Stevenson D. J., Stewart S. T., Toplis M. J., Usui T., Weiss B. P., Werner S. C., Wordsworth R. D., Wray J. J., Yingst R. A., Yung Y. L., and Zahnle K. J. (2016a) The sustainability of habitability on terrestrial planets: Insights, questions, and needed measurements from Mars for understanding the evolution of Earth-like worlds. *Journal of Geophysical Research: Planets* **121**, 1927-1961.
- Ehlmann B. L. and et al. (2019) A 2U SWIR-MIR Point Spectrometer for SmallSat and Landed Missions: Enabling Characterization of Solar System Volatiles. *Lunar and Planetary Science Conference* 50, #2806.
- Ehlmann B. L. and Mustard J. F. (2012) An *in-situ* record of major environmental transitions on early Mars at Northeast Syrtis Major. *Geophysical Research Letters* **39**.



- Ehlmann B. L., Swayze G. A., Milliken R. E., Mustard J. F., Clark R. N., Murchie S. L., Breit G. N., Wray J. J., Gondet B., Poulet F., Carter J., Calvin W. M., Benzel W. M., and Seelos K. D. (2016b) Discovery of alunite in Cross crater, Terra Sirenum, Mars: Evidence for acidic, sulfurous waters. *American Mineralogist* **101**, 1527-1542.
- Farley K. A., Malespin C., Mahaffy P., Grotzinger J. P., Vasconcelos P. M., Milliken R. E., Malin M., Edgett K. S., Pavlov A. A., Hurowitz J. A., Grant J. A., Miller H. B., Arvidson R., Beegle L., Calef F., Conrad P. G., Dietrich W. E., Eigenbrode J., Gellert R., Gupta S., Hamilton V., Hassler D. M., Lewis K. W., McLennan S. M., Ming D., Navarro-González R., Schwenzer S. P., Steele A., Stolper E. M., Sumner D. Y., Vaniman D., Vasavada A., Williford K., Wimmer-Schweingruber R. F., and MSL Science Team (2014) In Situ Radiometric and Exposure Age Dating of the Martian Surface. *Science* **343**.
- Fassett C. I., Head J. W., Kadish S. J., Mazarico E., Neumann G. A., Smith D. E., and Zuber M. T. (2012) Lunar impact basins: Stratigraphy, sequence and ages from superposed impact crater populations measured from Lunar Orbiter Laser Altimeter (LOLA) data. *Journal of Geophysical Research* **117**.
- Fassett C. I. and Minton D. A. (2013) Impact bombardment of the terrestrial planets and the early history of the Solar System. *Nature Geoscience* **6**, 520-524.
- Featherstone W. E., Hirt C., and Kuhn M. (2013) Band-limited Bouguer gravity identifies new basins on the Moon. *Journal of Geophysical Research (Planets)* **118**, 1397-1413.
- Fischer-Gödde M. and Becker H. (2012) Osmium isotope and highly siderophile element constraints on ages and nature of meteoritic components in ancient lunar impact rocks. *Geochimica et Cosmochimica Acta* **77**, 135-156.
- Fraeman A. A., Haag J. M., Eastwood M. L., Chen W., McKinley I. M., Sandford M., Blaney D. L., Ehlmann B. L., Green R. O., and Mouroulis P. (2020) An Ultra-Compact Imaging Spectrometer for the Lunar Surface: UCIS-Moon. *Lunar and Planetary Science Conference* **51**, #1610.
- Frey H. (2011) Previously unknown large impact basins on the Moon: Implications for lunar stratigraphy. In Recent Advances and Current Research Issues in *Lunar Stratigraphy: Geological Society of America Special Paper* (eds. W. A. Ambrose and D. A. Williams), pp. 53-75. Geological Society of America.
- Fruland R. M., Nagle J. S., and Allton J. H. (1982) Catalog of the Apollo 16 Lunar Core 60009/60010. *NASA Johnson Space Center, Lunar Curatorial Branch Publication 61*, JSC 17172.
- Fryxell R. and Heiken G. (1971) Description, Dissection, and Subsampling of Apollo 14 Core Sample 14230. *NASA Technical Memorandum*, NASA TM X-58070.
- GDAL/OGR contributors (2019) GDAL/OGR Geospatial Data Abstraction software Library. *Open Source Geospatial Foundation*, <https://gdal.org>.
- Goudge T. A., Mohrig D., Cardenas B. T., Hughes C. M., and Fassett C. I. (2018) Stratigraphy and paleohydrology of delta channel deposits, Jezero crater, Mars. *Icarus* **301**, 58-75.
- Graf J. C. (1993) Lunar soils grain size catalog. *NASA Technical Report NASA-RP-1265*, 484.
- Grant J. A., Golombek M. P., Grotzinger J. P., Wilson S. A., Watkins M. M., Vasavada A. R., Griffes J. L., and Parker T. J. (2011) The science process for selecting the landing site for the 2011 Mars Science Laboratory. *Planetary and Space Science* **59**, 1114-1127.



- Grant J. A., Golombek M. P., Wilson S. A., Farley K. A., Williford K. H., and Chen A. (2018) The science process for selecting the landing site for the 2020 Mars rover. *Planetary and Space Science* **164**, 106-126.
- Grant J. A., Warner N. H., Weitz C. M., Golombek M. P., Wilson S. A., Baker M., Hauber E., Ansan V., Charalambous C., Williams N., Calef F., Pike W. T., DeMott A., Kopp M., Lethcoe H., and Banks M. E. (2020) Degradation of Homestead Hollow at the InSight Landing Site Based on the Distribution and Properties of Local Deposits. *Journal of Geophysical Research: Planets* **125**, e2019JE0006350.
- Grant J. A., Wilson S. A., Ruff S. W., Golombek M. P., and Koestler D. L. (2006) Distribution of rocks on the Gusev Plains and on Husband Hill, Mars. *Geophysical Research Letters* **33**, 16202.
- Grotzinger J. P., Gupta S., Malin M. C., Rubin D. M., Schieber J., Siebach K., Sumner D. Y., Stack K. M., Vasavada A. R., Arvidson R. E., Calef F., Edgar L., Fischer W. F., Grant J. A., Griffes J., Kah L. C., Lamb M. P., Lewis K. W., Mangold N., Minitti M. E., Palucis M., Rice M., Williams R. M. E., Yingst R. A., Blake D., Blaney D., Conrad P., Crisp J., Dietrich W. E., Dromart G., Edgett K. S., Ewing R. C., Gellert R., Hurowitz J. A., Kocurek G., Mahaffy P., McBride M. J., McLennan S. M., Mischna M., Ming D., Milliken R., Newsom H., Oehler D., Parker T. J., Vaniman D., Wiens R. C., and Wilson S. A. (2015) Deposition, exhumation, and paleoclimate of an ancient lake deposit, Gale crater, Mars. *Science* **350**.
- Hartmann K. W. (2019) History of the Terminal Cataclysm Paradigm: Epistemology of a Planetary Bombardment That Never (?) Happened. *Geosciences* **9**, 285.
- Hartmann W. K. and Neukum G. (2001) Cratering chronology and the evolution of Mars. *Space Science Reviews* **96**, 165-194.
- Hartmann W. K., Ryder G., Dones L., and Grinspoon D. (2000) The time-dependent intense bombardment of the primordial Earth-Moon system. In *Origin of the Earth and Moon* (eds. R. M. Canup and K. Righter), pp. 493-512. University of Arizona Press, Tucson.
- Haruyama J., Ohtake M., Matsunaga T., Morota T., Honda C., Yokota Y., Abe M., Ogawa Y., Miyamoto H., Iwasaki A., Pieters C. M., Asada N., Demura H., Naru Hirata, Terazono J., Sasaki S., Saiki K., Yamaji A., Torii M., and Josset J.-L. (2009) Long-Lived Volcanism on the Lunar Farside Revealed by SELENE Terrain Camera *Science* **323**, 905-908.
- Haskin L. A., Korotev R. L., Rockow K. M., and Jolliff B. L. (1998) The case for an Imbrium origin of the Apollo Th-rich impact-melt breccias. *Meteoritics and Planetary Science* **33**, 959-975.
- Hiesinger H., Head J. W., III, Wolf U., Jaumann R., and Neukum G. (2011) Ages and stratigraphy of lunar mare basalts: A synthesis. In *Recent Advances and Current Research Issues in Lunar Stratigraphy* (eds. W. A. Ambrose and D. A. Williams), pp. 0. Geological Society of America.
- Hiesinger H., Head J. W., Wolf U., Jaumann R., and Neukum G. (2003) Ages and stratigraphy of mare basalts in Oceanus Procellarum, Mare Nubium, Mare Cognitum, and Mare Insularum. *Journal of Geophysical Research* **108**.
- Hiesinger H., Jaumann R., Neukum G., and Head J. W. (2000) Ages of mare basalts on the lunar nearside. *Journal of Geophysical Research* **105**, 29239-29276.



- Hiesinger H., Marchi S., Schmedemann N., Schenk P., Pasckert J. H., Neesemann A., O'Brien D. P., Kneissl T., Ermakov A. I., Fu R. R., Bland M. T., Nathues A., Platz T., Williams D. A., Jaumann R., Castillo-Rogez J. C., Ruesch O., Schmidt B., Park R. S., Preusker F., Buczkowski D. L., Russell C. T., and Raymond C. A. (2016a) Cratering on Ceres: Implications for its crust and evolution. *Science* **353**, aaf4759.
- Hiesinger H., Pasckert J. H., van der Bogert C. H., Robinson M. S., Weinauer J., Lawrence S. J., Stopar J. D., and Robinson M. S. (2016b) New Crater Size-Frequency Distribution Measurements for Autolycus Crater, Moon. *Lunar and Planetary Science Conference* 47, #1879.
- Hiesinger H., van der Bogert C. H., Pasckert J. H., Funcke L., Giacomini L., Ostrach L. R., and Robinson M. S. (2012) How old are young lunar craters? *Journal of Geophysical Research (Planets)* **117**.
- James O. B. (1981) Petrologic and age relations of the Apollo 16 rocks: Implications for subsurface geology and the age of the Nectaris basin. *Proceedings of the Lunar and Planetary Science Conference* **12**, 209-233.
- Jawin E. R., Valencia S. N., Watkins R. N., Crowell J. M., Neal C. R., and Schmidt G. (2019) Lunar Science for Landed Missions Workshop Findings Report. *Earth and Space Science* **6**, 2-40.
- Jolliff B. L., Rockow K. M., Korotev R. L., and Haskin L. A. (1996) Lithologic distribution and geologic history of the Apollo 17 site: The record in soils and small rock particles from the highland massifs. *Meteoritics and Planetary Science* **31**, 116-145.
- Jolliff B. L., Shearer C. K., and Cohen B. A. (2012) Sampling South Pole-Aitken Basin: The Moonrise Approach. In Annual Meeting of the Lunar Exploration and Analysis Group, pp. Abstract #3047. Lunar and Planetary Institute, Greenbelt.
- Jolliff B. L., Shearer C. K., Papanastassiou D. A., Liu Y., and Team M. S. (2017) Why Do We Need Samples from the Moon's South Pole-Aitken Basin and What Would We Do with Them? *Lunar and Planetary Science Conference* 48.
- Jourdan F. (2012) The $^{40}\text{Ar}/^{39}\text{Ar}$ dating technique applied to planetary sciences and terrestrial impacts. *Australian Journal of Earth Sciences* **59**, 199-224.
- Kennedy T., Jourdan F., Bevan A. W. R., Mary Gee M. A., and Frew A. (2013) Impact history of the HED parent body(ies) clarified by new $^{40}\text{Ar}/^{39}\text{Ar}$ analyses of four HED meteorites and one anomalous basaltic achondrite. *Geochimica et Cosmochimica Acta* **115**, 162-182.
- Le Deit L., Mangold N., Forni O., Cousin A., Lasue J., Schröder S., Wiens R. C., Sumner D., Fabre C., and Stack K. M. (2016) The potassic sedimentary rocks in Gale Crater, Mars, as seen by ChemCam on board Curiosity. *Journal of Geophysical Research: Planets* **121**, 784-804.
- Leonard, Jason M., et al. (2019) OSIRIS-REx Orbit Determination Performance During the Navigation Campaign. *AAS/AIAA Astrodynamics Specialist Conference*, AAS-19-714.
- Lindsay F. N., Delaney J. S., Herzog G. F., Turrin B. D., Park J., and Swisher Iii C. C. (2015) Rheasilvia provenance of the Kapoeta howardite inferred from ~ 1 Ga $^{40}\text{Ar}/^{39}\text{Ar}$ feldspar ages. *Earth and Planetary Science Letters* **413**, 208-213.
- Lindsay J. F., Heiken G. H., and Fryxell R. (1971) Description of Core Samples Returned by Apollo 12. *NASA Technical Memorandum*, NASA TM X-58066.
- Lockheed Martin Space Systems Company (2014) Mars One 2018 Lander Payload Proposal Information Package. https://www.mars-one.com/images/uploads/MarsOne_PIP.pdf.



Lunar Exploration Analysis Group (2017) Advancing Science of the Moon: Report of the Specific Action Team. <https://www.lpi.usra.edu/leag/reports/ASM-SAT-Report-final.pdf>.

Mahaffy P. R., Benna M., King T., Harpold D. N., Arvey R., Barciniak M., Bendt M., Carrigan D., Errigo T., Holmes V., Johnson C. S., Kellogg J., Kimvilakani P., Lefavor M., Hengemihle J., Jaeger F., Lyness E., Maurer J., Melak A., Noreiga F., Noriega M., Patel K., Prats B., Raaen E., Tan F., Weidner E., Gundersen C., Battel S., Block B. P., Arnett K., Miller R., Cooper C., Edmonson C., and Nolan J. T. (2015a) The Neutral Gas and Ion Mass Spectrometer on the Mars Atmosphere and Volatile Evolution Mission. *Space Science Reviews* **195**, 49-73.

Mahaffy P. R., Richard Hodges R., Benna M., King T., Arvey R., Barciniak M., Bendt M., Carigan D., Errigo T., Harpold D. N., Holmes V., Johnson C. S., Kellogg J., Kimvilakani P., Lefavor M., Hengemihle J., Jaeger F., Lyness E., Maurer J., Nguyen D., Nolan T. J., Noreiga F., Noriega M., Patel K., Prats B., Quinones O., Raaen E., Tan F., Weidner E., Woronowicz M., Gundersen C., Battel S., Block B. P., Arnett K., Miller R., Cooper C., and Edmonson C. (2015b) The Neutral Mass Spectrometer on the Lunar Atmosphere and Dust Environment Explorer Mission. In *The Lunar Atmosphere and Dust Environment Explorer Mission (LADEE)* (eds. R. C. Elphic and C. T. Russell), pp. 27-61. Springer International Publishing, Cham.

Mahaffy P. R., Webster C. R., Cabane M., Conrad P. G., Coll P., Atreya S. K., Arvey R., Barciniak M., Benna M., Bleacher L., Brinckerhoff W. B., Eigenbrode J. L., Carignan D., Cascia M., Chalmers R. A., Dworkin J. P., Errigo T., Everson P., Franz H., Farley R., Feng S., Frazier G., Freissinet C., Glavin D. P., Harpold D. N., Hawk D., Holmes V., Johnson C. S., Jones A., Jordan P., Kellogg J., Lewis J., Lyness E., Malespin C. A., Martin D. K., Maurer J., McAdam A. C., McLennan D., Nolan T. J., Noriega M., Pavlov A. A., Prats B., Raaen E., Sheinman O., Sheppard D., Smith J., Stern J. C., Tan F., Trainer M., Ming D. W., Morris R. V., Jones J., Gundersen C., Steele A., Wray J., Botta O., Leshin L. A., Owen T., Battel S., Jakosky B. M., Manning H., Squyres S., Navarro-González R., McKay C. P., Raulin F., Sternberg R., Buch A., Sorensen P., Kline-Schoder R., Coscia D., Szopa C., Teinturier S., Baffes C., Feldman J., Flesch G., Forouhar S., Garcia R., Keymeulen D., Woodward S., Block B. P., Arnett K., Miller R., Edmonson C., Gorevan S., and Mumm E. (2012) The Sample Analysis at Mars Investigation and Instrument Suite. *Space Science Reviews* **170**, 401-478.

Maher K. A. and Stevenson D. J. (1988) Impact frustration of the origin of life. *Nature* **331**, 612-614.

Maki J., Thiessen D., Pourangi A., Kobzeff P., Litwin T., Scherr L., Elliott S., Dingizian A., and Maimone M. (2012) The Mars science laboratory engineering cameras. *Space Science Reviews* **170**, 77-93.

Maki J. N., Bell J. F., Herkenhoff K. E., Squyres S. W., Kiely A., Klimesh M., Schwochert M., Litwin T., Willson R., and Johnson A. (2003) Mars exploration rover engineering cameras. *Journal of Geophysical Research: Planets* **108**.

Maki J. N., Golombek M., Deen R., Abarca H., Sorice C., Goodsall T., Schwochert M., Lemmon M., Trebi-Ollennu A., and Banerdt W. B. (2018) The color cameras on the InSight lander. *Space Science Reviews* **214**, 105.

Marchi S., Bottke W. F., Cohen B. A., Wünnemann K., Kring D. A., McSween H. Y., Sanctis M. C. D., O'Brien D. P., Schenk P., Raymond C. A., and Russell C. T. (2013) High-velocity collisions from the lunar cataclysm recorded in asteroidal meteorites. *Nature Geoscience* **6**, 303-307.

Martin P. E., Farley K. A., Baker M. B., Malespin C. A., Schwenzer S. P., Cohen B. A., Mahaffy P. R., McAdam A. C., Ming D. W., Vasconcelos P. M., and Navarro-González R. (2017) A Two-Step K-Ar Experiment on Mars: Dating the Diagenetic Formation of Jarosite from Amazonian Groundwaters. *Journal of Geophysical Research (Planets)* **122**, 2803-2818.



- McKay D. S., Heiken G., Basu A., Blanford G., Simon S., Reedy R., French B. M., and Papike J. (1991) The lunar regolith. In *Lunar Sourcebook* (eds. G. H. Heiken, D. T. Vaniman, and B. M. French), pp. 285-356. Cambridge University Press, Cambridge.
- MEPAG (2020) Mars Scientific Goals, Objectives, Investigations, and Priorities. <https://mepag.jpl.nasa.gov/reports.cfm>.
- Merle R. E., Nemchin A. A., Grange M. L., Whitehouse M. J., and Pidgeon R. T. (2014) High resolution U-Pb ages of Ca-phosphates in Apollo 14 breccias: Implications for the age of the Imbrium impact. *Meteoritics and Planetary Science* **49**, 2241-2251.
- Meyer C. (2016) *Lunar Sample Compendium*. <http://curator.jsc.nasa.gov/lunar/compendium.cfm>; last accessed June 8, 2020.
- Michael G. G. (2013) Planetary surface dating from crater size–frequency distribution measurements: Multiple resurfacing episodes and differential isochron fitting. *Icarus* **226**, 885-890.
- Milliken R. E. and Bish D. L. (2010) Sources and sinks of clay minerals on Mars. *Philosophical Magazine* **90**, 2293-2308.
- Mojzsis S. and Harrison T. M. (2000) Vestiges of a Beginning: Clues to the Emergent Biosphere Recorded in the Oldest Known Sedimentary Rocks. *GSA Today* **10**, 1-6.
- Morbidelli A., Nesvornyy D., Laurenz V., Marchi S., Rubie D. C., Elkins-Tanton L., Wieczorek M., and Jacobson S. (2018) The timeline of the lunar bombardment: Revisited. *Icarus* **305**, 262-276.
- Moriarty III D. P. and Pieters C. M. (2016) Complexities in pyroxene compositions derived from absorption band centers: Examples from Apollo samples, HED meteorites, synthetic pure pyroxenes, and remote sensing data. *Meteoritics & Planetary Science* **51**, 207-234.
- Murchie S. L., Bibring J.-P., Arvidson R. E., Bishop J. L., Carter J., Ehlmann B. L., Langevin Y., Mustard J. F., Poulet F., Riu L., Seelos K. D., and Viviano C. E. (2019) Visible to Short-Wave Infrared Spectral Analyses of Mars from Orbit Using CRISM and OMEGA. In *Remote Compositional Analysis: Techniques for Understanding Spectroscopy, Mineralogy, and Geochemistry of Planetary Surfaces* (eds. J. F. Bell III, J. L. Bishop, and J. E. Moersch), pp. 453-483. Cambridge University Press, Cambridge.
- Mustard J. F., Poulet F., Head J. W., Mangold N., Bibring J. P., Pelkey S. M., Fassett C. I., Langevin Y., and Neukum G. (2007) Mineralogy of the Nili Fossae region with OMEGA/Mars Express data: 1. Ancient impact melt in the Isidis Basin and implications for the transition from the Noachian to Hesperian. *Journal of Geophysical Research: Planets* **112**.
- Nagle J. S. (1979) Preliminary description and interpretation of Apollo 14 cores 14210/11. *Proceedings of the Lunar and Planetary Science Conference* **10**, 1299-1319.
- Nagle J. S. (1980a) Core 14220 and the lateral continuity of soils at Apollo 14 station G. *The Moon and the Planets* **23**, 165-183.
- Nagle J. S. (1980b) Possible rim crest deposits in cores 12027 and 15008: Some interpretations and problems for future research. *Proceedings of the Lunar and Planetary Science Conference* **11**, 1479-1496.
- Nagle J. S. (1982) Depositional units in drive tube 64001/2. *Lunar Science Conference* **13**, #566-567.



- National Aeronautics and Space Administration (2015) NASA Technology Roadmaps, TA8: Science Instruments, Observatories, and Sensor Systems. https://www.nasa.gov/sites/default/files/atoms/files/2015_nasa_technology_roadmaps_ta_8_science_instruments_final.pdf.
- National Research Council (2007) *The Scientific Context for the Exploration of the Moon*. The National Academies Press, Washington, DC. pp. 120.
- Needham D. H. and Kring D. A. (2017) Lunar volcanism produced a transient atmosphere around the ancient Moon. *Earth and Planetary Science Letters* **478**, 175-178.
- Neukum G. and Ivanov B. A. (1994) Crater size distributions and impact probabilities on Earth from lunar, terrestrial-planet, and asteroid cratering data. In *Hazards due to Comets and Asteroids* (eds. T. Gehrels, M. S. Matthews, and A. M. Schumann), pp. 359-416. University of Arizona Press, Tucson.
- Neukum G., Ivanov B. A., and Hartmann W. K. (2001) Cratering records in the inner solar system in relation to the lunar reference system. *Space Science Reviews* **96**, 55-86.
- Neumann G. A., Zuber M. T., Wieczorek M. A., Head J. W., Baker D. M. H., Solomon S. C., Smith D. E., Lemoine F. G., Mazarico E., Sabaka T. J., Goossens S. J., Melosh H. J., Phillips R. J., Asmar S. W., Konopliv A. S., Williams J. G., Sori M. M., Soderblom J. M., Miljković K., Andrews-Hanna J. C., Nimmo F., and Kiefer W. S. (2015) Lunar impact basins revealed by Gravity Recovery and Interior Laboratory measurements. *Science Advances* **1**.
- Norman M. D. (2009) The Lunar Cataclysm: Reality or “Mythconception”? *Elements* **5**, 23-28.
- Norman M. D., Duncan R. A., and Huard J. J. (2010) Imbrium provenance for the Apollo 16 Descartes terrain: Argon ages and geochemistry of lunar breccias 67016 and 67455. *Geochimica et Cosmochimica Acta* **74**, 763-783.
- Orgel C., Michael G., Fassett C. I., van der Bogert C. H., Riedel C., Kneissl T., and Hiesinger H. (2018) Ancient bombardment of the inner solar system: Reinvestigation of the “fingerprints” of different impactor populations on the lunar surface. *Journal of Geophysical Research: Planets* **123**, 748-762.
- Pieters C. M. and Noble S. K. (2016) Space weathering on airless bodies. *Journal of Geophysical Research: Planets* **121**, 1865-1884.
- Pilorget C. P. and Bibring J. P. (2013) NIR reflectance hyperspectral microscopy for planetary science: Application to the MicrOmega instrument. *Planetary and Space Science* **76**, 42-52.
- Poulet F., Gross C., Horgan B., Loizeau D., Bishop J. L., Carter J., and Orgel C. (2020) Mawrth Vallis, Mars: A Fascinating Place for Future In Situ Exploration. *Astrobiology* **20**, 199-234.
- Pun A., Keil K., Taylor G. J., and Wieler R. (1998) The Kapoeta howardite: Implications for the regolith evolution of the HED parent body. *Meteoritics and Planetary Science* **33**, 835-851.
- Qiao L., Head James W., Xiao L., Wilson L., and Dufek Josef D. (2017) The role of substrate characteristics in producing anomalously young crater retention ages in volcanic deposits on the Moon: Morphology, topography, subresolution roughness, and mode of emplacement of the Sosigenes lunar irregular mare patch. *Meteoritics & Planetary Science* **53**, 778-812.
- Quinn D. P. and Ehlmann B. L. (2019) The Deposition and Alteration History of the Northeast Syrtis Major Layered Sulfates. *Journal of Geophysical Research: Planets* **124**, 1743-1782.



- Rhodes J. M., Hubbard N. J., Wiesmann H., Rodgers K. V., Brannon J. C., and Bansal B. M. (1976) Chemistry, classification, and petrogenesis of Apollo 17 mare basalts. *Proceedings of the Lunar and Planetary Science Conference* 7, 1467-1489.
- Riley S. J., DeGloria S. D., and Elliot R. (1999) A terrain ruggedness index that quantifies topographic heterogeneity. *Intermountain Journal of Sciences* 5, 23–27.
- Robbins S. J. (2014) New crater calibrations for the lunar crater-age chronology. *Earth and Planetary Science Letters* 403, 188-198.
- Rogers A. D., Warner N. H., Golombek M. P., Head Iii J. W., and Cowart J. C. (2018) Areal Extensive Surface Bedrock Exposures on Mars: Many Are Clastic Rocks, Not Lavas. *Geophysical Research Letters* 45, 1767-1777.
- Runyon K. D., Moriarty D. P., Denevi B. W., Greenhagen B. T., Morgan G., Young K. E., Cohen B. A., van der Bogert C. H., Hiesinger H., and Jozwiak L. M. (2020) Impact Melt Facies in the Moon's Crisium Basin: Identifying, Characterizing, and Future Radiogenic Dating. *Journal of Geophysical Research (Planets)* 125, e06024.
- Ryder G. (1990) Lunar samples, lunar accretion, and the early bombardment of the Moon. *Eos* 71, 313, 322-323.
- Ryder G., Koeberl C., and Mojzsis S. J. (2000) Heavy bombardment on the Earth at ~3.85 Ga: The search for petrographic and geochemical evidence. In *Origin of the Earth and Moon* (eds. R. M. Canup and K. Righter), pp. 475-492. University of Arizona Press, Tucson.
- Ryder G. and Norman M. D. (1980) Catalog of Apollo 16 rocks. *NASA JSC Curator's Office publication #52*.
- Sautter V., Fabre C., Forni O., Toplis M. J., Cousin A., Ollila A. M., Meslin P. Y., Maurice S., Wiens R. C., Baratoux D., Mangold N., Le Mouélic S., Gasnault O., Berger G., Lasue J., Anderson R. A., Lewin E., Schmidt M., Dyar D., Ehlmann B. L., Bridges J., Clark B., and Pinet P. (2014) Igneous mineralogy at Bradbury Rise: The first ChemCam campaign at Gale crater. *Journal of Geophysical Research: Planets* 119, 30-46.
- SBAG (2016) *Goals and Objectives for the Exploration and Investigation of the Solar System's Small Bodies*. <http://www.lpi.usra.edu/sbag/goals/> last accessed ver. 1.2.2016.
- Schaeffer G. A. and Schaeffer O. A. (1977) Ar-39 - Ar-40 ages of lunar rocks. *Proceedings of the Lunar and Planetary Science Conference* 8, 2253-2300.
- Scheller E. L. and Ehlmann B. L. (2020) Composition, Stratigraphy, and Geological History of the Noachian Basement Surrounding the Isidis Impact Basin. *Journal of Geophysical Research: Planets* n/a, #2019JE006190.
- Schenk P., O'Brien D. P., Marchi S., Gaskell R., Preusker F., Roatsch T., Jaumann R., Buczkowski D., Mccord T., Mcsween H. Y., Williams D., Yingst A., Raymond C., and Russell C. (2012) The Geologically Recent Giant Impact Basins at Vesta's South Pole. *Science* 336, 694-697.
- Schmedemann N., Kneissl T., Ivanov B. A., Michael G. G., Wagner R. J., Neukum G., Ruesch O., Hiesinger H., Krohn K., Roatsch T., Preusker F., Sierks H., Jaumann R., Reddy V., Nathues A., Walter S. H. G., Neesemann A., Raymond C. A., and Russell C. T. (2014) The cratering record, chronology and surface ages of (4) Vesta in comparison to smaller asteroids and the ages of HED meteorites. *Planetary and Space Science* 103, 104-130.



- Schmitt H. H., Petro N. E., Wells R. A., Robinson M. S., Weiss B. P., and Mercer C. M. (2017) Revisiting the field geology of Taurus-Littrow. *Icarus* **298**, 2-33.
- Shahrzad S., Kinch K. M., Goudge T. A., Fassett C. I., Needham D. H., Quantin-Nataf C., and Knudsen C. P. (2019) Crater Statistics on the Dark-Toned, Mafic Floor Unit in Jezero Crater, Mars. *Geophysical Research Letters* **46**, 2408-2416.
- Shearer C. K. and Papike J. J. (1999) Magmatic evolution of the Moon. *American Mineralogist* **84**, 1469-1494.
- Shoemaker E. M. and Morris E. C. (1970) Physical Characteristics of the Lunar Regolith Determined From Surveyor Television Observations. *Radio Science* **5**, 129-155.
- Spudis P. and Pieters C. (1991) Global and regional data about the Moon. In *Lunar Sourcebook: A User's Guide to the Moon* (eds. G. H. Heiken, D. T. Vaniman, and B. M. French), pp. 595-632. Cambridge University Press, Cambridge.
- Spudis P. D. (1993) *The Geology of Multi-Ring Impact Basins: The Moon and Other Planets*. Cambridge University Press, Cambridge.
- Spudis P. D. and Sliz M. U. (2017) Impact melt of the lunar Crisium multiring basin. *Geophysical Research Letters* **44**, 1260-1265.
- Spudis P. D., Wilhelms D. E., and Robinson M. S. (2011) The Sculptured Hills of the Taurus Highlands: Implications for the relative age of Serenitatis, basin chronologies and the cratering history of the Moon. *Journal of Geophysical Research* **116**.
- Stöffler D. and Ryder G. (2001) Stratigraphy and isotope ages of lunar geologic units: Chronology and standard for the inner solar system. *Space Science Reviews* **96**, 9-54.
- Stöffler D., Ryder G., Ivanov B. A., Artemieva N. A., Cintala M. J., and Grieve R. A. F. (2006) Cratering History and Lunar Chronology. *Reviews in Mineralogy and Geochemistry* **60**, 519-596.
- Strom R. G. and Neukum G. (1988) The cratering record on Mercury and the origin of impacting objects. In *Mercury* (eds. F. Vilas, C. R. Chapman, and M. S. Matthews), pp. 336-373. University of Arizona Press, Tucson.
- Sun V., Quantin-Nataf C., Ehlmann B., Scheller E., and Kelemen P. (2018) *Mars 2020 Science Team Assessment of Northeast Syrtis and Midway*. https://marsnext.jpl.nasa.gov/workshops/2018-10/PRESENTATIONS/m2020_lsw_day2_11_NESyrtis_Midway_FINAL2.pdf; last accessed June 8.
- Swindle T. D., Kring D. A., and Weirich J. R. (2014) $^{40}\text{Ar}/^{39}\text{Ar}$ ages of impacts involving ordinary chondrite meteorites. *Geological Society, London, Special Publications* **378**, 333-347.
- Taghioskoui M. and Zaghoul M. (2016) Plasma ionization under simulated ambient Mars conditions for quantification of methane by mass spectrometry. *Analyst* **141**, 2270-2277.
- Tanaka K. L., Robbins S. J., Fortezzo C. M., Skinner J. A., and Hare T. M. (2014) The digital global geologic map of Mars: Chronostratigraphic ages, topographic and crater morphologic characteristics, and updated resurfacing history. *Planetary and Space Science* **95**, 11-24.
- Tera F., Papanastassiou D. A., and Wasserburg G. J. (1974) Isotopic evidence for a terminal lunar cataclysm. *Earth and Planetary Science Letters* **22**, 1-21.
- van der Bogert C. and Hiesinger H. (2020) Which samples are needed for improved calibration of the lunar cratering chronology? *Lunar and Planetary Science Conference* 51, #2088.



- van der Bogert C. H., Hiesinger H., and Spudis P. (2017) The Age of the Crisium Impact Basin. *New Views of the Moon 2 - Europe*, #1988.
- Van Gorp B. and et al. (2014) Ultra-compact imaging spectrometer for remote, in situ, and microscopic planetary mineralogy. *Journal of Applied Remote Sensing* **8**, 084988-084988.
- Wang J., Cheng W., and Zhou C. (2015) A Chang'E-1 global catalog of lunar impact craters. *Planetary and Space Science* **112**, 42-45.
- Warner N. H., Grant J. A., Wilson S. A., Golombek M. P., DeMott A., Charalambous C., Hauber E., Ansan V., Weitz C., Pike T., Williams N., Banks M. E., Calef F., Baker M., Kopp M., Deahn M., Lethcoe H., and Berger L. (2020) An Impact Crater Origin for the InSight Landing Site at Homestead Hollow, Mars: Implications for Near Surface Stratigraphy, Surface Processes, and Erosion Rates. *Journal of Geophysical Research: Planets* **125**, e2019JE006333.
- Warwick R. W. (2003) Low-cost, light-weight Mars landing system. In *2003 IEEE Aerospace Conference Proceedings*, DOI 10.1109/AERO.2003.1235540.
- Watkins R. N., Jolliff B. L., Mistick K., Fogerty C., Lawrence S. J., Singer K. N., and Ghent R. R. (2019) Boulder Distributions Around Young, Small Lunar Impact Craters and Implications for Regolith Production Rates and Landing Site Safety. *Journal of Geophysical Research: Planets* **124**, 2754-2771.
- Weitz C. M., Grant J. A., Golombek M. P., Warner N. H., Hauber E., Ansan V., S. A. W., Constantinos C., Williams M., Calef F., Pike W. T., Lethcoe-Wilson H., Maki J., DeMott A., and Kopp M. (2020) Comparison of InSight Homestead hollow to hollows at the Spirit landing site. *Journal of Geophysical Research* **125**, in press.
- Weitz C. M., Noe Dobrea E., and Wray J. J. (2015) Mixtures of clays and sulfates within deposits in western Melas Chasma, Mars. *Icarus* **251**, 291-314.
- Williams B., Antreasian P., Carranza E., Jackman C., Leonard J., Nelson D., Page B., Stanbridge D., Wibben D., Williams K., Moreau M., Berry K., Getzandanner K., Liounis A., Mashiku A., Highsmith D., Sutter B., and Laurretta D. S. (2018) OSIRIS-REx Flight Dynamics and Navigation Design. *Space Science Reviews* **214**, 69.
- Wilhelms D. E. (1987) The geologic history of the Moon. *U.S. Geological Survey Professional Paper* **1348**.
- Williams D. A., Denevi B. W., Mittlefehldt D. W., Mest S. C., Schenk P. M., Yingst R. A., Buczkowski D. L., Scully J. E. C., Garry W. B., McCord T. B., Combe J.-P., Jaumann R., Pieters C. M., Nathues A., Le Corre L., Hoffmann M., Reddy V., Schäfer M., Roatsch T., Preusker F., Marchi S., Kneissl T., Schmedemann N., Neukum G., Hiesinger H., De Sanctis M. C., Ammannito E., Frigeri A., Prettyman T. H., Russell C. T., and Raymond C. A. (2014a) The geology of the Marcia quadrangle of asteroid Vesta: Assessing the effects of large, young craters. *Icarus* **244**, 74-88.
- Williams J.-P., Pathare A. V., and Aharonson O. (2014b) The production of small primary craters on Mars and the Moon. *Icarus* **235**, 23-36.
- Wilson M. F. J., O'Connell B., Brown C., Guinan J. C., and Grehan A. J. (2007) Multiscale Terrain Analysis of Multibeam Bathymetry Data for Habitat Mapping on the Continental Slope. *Marine Geodesy* **30**, 3-35.



- Wray J. J., Milliken R. E., Dundas C. M., Swayze G. A., Andrews-Hanna J. C., Baldrige A. M., Chojnacki M., Bishop J. L., Ehlmann B. L., Murchie S. L., Clark R. N., Seelos F. P., Tornabene L. L., and Squyres S. W. (2011) Columbus crater and other possible groundwater-fed paleolakes of Terra Sirenum, Mars. *Journal of Geophysical Research: Planets* **116**.
- Young K. E., van Soest M. C., Hodges K. V., Watson E. B., Adams B. A., and Lee P. (2013) Impact thermochronology and the age of Haughton impact structure, Canada. *Geophysical Research Letters* **40**, 3836-3840.
- Zacny K., Betts B., Hedlund M., Long P., Gramlich M., Tura K., Chu P., Jacob A., and Garcia A. (2014a) PlanetVac: Pneumatic regolith sampling system. *2014 IEEE Aerospace Conference*, #1-8.
- Zacny K., Chu P., Davis K., Paulsen G., and Craft J. (2014b) Mars2020 sample acquisition and caching technologies and architectures. In *2014 IEEE Aerospace Conference*, pp. 1-12.
- Zellner N. E. B. (2017) Cataclysm no more: New views on the timing and delivery of lunar impactors. *Origins of Life and Evolution of Biospheres* **47**, 261-280.
- Zhang B., Lin Y., Moser D. E., Hao J., Shieh S. R., and Bouvier A. (2019) Imbrium Age for Zircons in Apollo 17 South Massif Impact Melt Breccia 73155. *Journal of Geophysical Research: Planets* **124**, 3205-3218.
- Zhao J., Xiao L., Qiao L., Glotch T. D., and Huang Q. (2017) The Mons Rümker volcanic complex of the Moon: A candidate landing site for the Chang'E-5 mission. *Journal of Geophysical Research (Planets)* **122**, 1419-1442.